

ÉCOLE DE TECHNOLOGIE SUPÉRIEURE
UNIVERSITÉ DU QUÉBEC

MANUSCRIPT-BASED THESIS PRESENTED TO
ÉCOLE DE TECHNOLOGIE SUPÉRIEURE

IN PARTIAL FULFILLEMENT OF THE REQUIREMENTS FOR
THE DEGREE OF DOCTOR OF PHILOSOPHY
Ph. D.

BY
Amir Masoud TAHVILIAN

NUMERICAL AND EXPERIMENTAL STUDY OF A FLEXIBLE ROBOTIC
GRINDING PROCESS

MONTRÉAL, JANUARY 20, 2015



Amir Masoud Tahvilian, 2015



This Creative Commons license allows readers to download this work and share it with others as long as the author is credited. The content of this work may not be modified in any way or used commercially.

BOARD OF EXAMINERS (THESIS PH.D.)

THIS THESIS HAS BEEN EVALUATED

BY THE FOLLOWING BOARD OF EXAMINERS

Prof. Zhaoheng Liu, Thesis Supervisor
Department of Mechanical Engineering at École de technologie supérieure

Prof. Henri Champlaud, Thesis Co-supervisor
Department of Mechanical Engineering at École de technologie supérieure

Prof. Marie-José Nollet, Chair, Board of Examiners
Department of Construction Engineering at École de technologie supérieure

Prof. Stéphane Hallé, Member of the jury
Department of Mechanical Engineering at École de technologie supérieure

Dr Bin Shi, Independent External Evaluator
Aerospace Manufacturing Technologies Centre, National Research Council Canada

THIS THESIS WAS PRESENTED AND DEFENDED

IN THE PRESENCE OF A BOARD OF EXAMINERS AND THE PUBLIC

DECEMBER 12, 2014

AT ÉCOLE DE TECHNOLOGIE SUPÉRIEURE

ACKNOWLEDGMENTS

First of all, I would like to thank my parents, Ahmad and Tahereh, my brother Amir for all the support, you provided for me during this stage of my life. This was simply not possible without your encouragement and unconditional love.

I sincerely thank my directors at École de Technologie Supérieure, Professor Zhaoheng Liu and Professor Henri Champliand for their supervision and support during this research work. Their invaluable scientific advice and friendly attitude helped me to overcome all the difficulties through the period of my PhD study.

I would like to thank to Mr. Bruce Hazel, my supervisor at Hydro-Québec research institute (IREQ), whose grateful support, inspiring ideas and insightful discussions helped me for completion of my PhD program. I am also grateful for all the technical help and support from the SCOMPI team at IREQ during the experimental set-up preparation. A special thanks to Mr. Marin Lagacé for providing his image processing software and adding features specifically for this research purpose.

I also would like to thank the jury members who evaluated my thesis and for their constructive suggestions and helpful advice.

Finally, I acknowledge the financial support from Natural Science and Engineering Research Council of Canada (NSERC) and Hydro-Québec research institute (IREQ).

NUMERICAL AND EXPERIMENTAL STUDY OF A FLEXIBLE ROBOTIC GRINDING PROCESS

Amir Masoud TAHVILIAN

SUMMARY

Robotic grinding is among the least studied processes due to its complexity compared to conventional grinding and other machining processes. In robotic grinding with a light, flexible robot, low manipulator stiffness is a key factor affecting process behavior and causing impact phenomena. Force prediction and thermal damage are important aspects to consider in robotic grinding because of the vibrational nature of the process. The portable robot used in the process under study is a multi-purpose track-based manipulator developed by IREQ, Hydro-Quebec's research institute. The main application of this light-weight robot, named "SCOMPI" (Super COMPact robot Ireq), is in situ maintenance of hydro turbine runners. It is observed that the grinding process by this robot is interrupted at each revolution of the wheel rather than having a continuous cutting action. This impact cutting behavior appears due to the low stiffness of the flexible manipulator under high grinding forces. Special attention has thus been given to gain a better understanding of the material removal process in such robotic grinding. The objective is to establish appropriate relations among chip formation, operational cutting forces, temperature, material removal rate and consumed power in the process.

The purpose of this study is to use numerical and experimental methods to gain a better understanding of this flexible robotic grinding process. First, a finite element thermal analysis is carried out to evaluate thermal aspects of the process, such as the energy partition ratio and temperature distribution in the workpiece. A new representation of the heat source in line with the impacting effects of robotic grinding is considered in the model. Experimental measurements in conjunction with numerical analyses led to an energy partition model applicable to this study under varying operating conditions. In the second part, the topography of grinding wheels used in the process is characterized and related to depth of cut. The cutting edges of wheels have a significant effect in process efficiency and are essential in understanding material removal in the grinding process. The variation of wheel topography due to process conditions is demonstrated. Knowledge of the edges involved in cutting during the process are vital for micro-scale modeling of cutting interactions occurring in the wheel-workpiece contact zone. Ongoing work on micro-scale force modeling through FEM will benefit from this wheel topography study. The third part of this thesis is dedicated to enhancing the empirical basis for an existing force model of the process. An impact cutting regime is observed by means of high-speed camera recordings and measured process force signals. This regime is detected at different grinding power levels and used in identifying the empirical coefficients. The energy partition model from the first part of study is also incorporated to obtain a friction-chip energy ratio used to determine the force model constants.

VIII

Keywords: robotic grinding; finite element analysis; thermal model, force model, impact cutting, wheel topography

ÉTUDE NUMÉRIQUE ET EXPÉRIMENTALE D'UN PROCÉDÉ ROBOTISÉ DE MEULAGE PAR ROBOTS FLEXIBLES

Amir Masoud TAHVILIAN

RÉSUMÉ

Le meulage robotisé est parmi les procédés les moins étudiés en raison de sa complexité par rapport au meulage traditionnel et à d'autres procédés d'usinage. Dans un procédé de meulage robotisé, la faible rigidité du manipulateur est un facteur majeur qui modifie le comportement du procédé et provoque des phénomènes d'impact. La prédiction de force et l'étude des dommages thermiques constituent ainsi des éléments importants dans l'étude du meulage robotisé afin de prendre en considération la nature vibratoire du procédé. Le robot portable utilisé dans le procédé à l'étude est un manipulateur sur rail à usage multiple développé par l'IREQ, l'Institut de recherche d'Hydro-Québec. La principale application de ce robot léger, nommé "SCOMPI", consiste en la maintenance sur place des roues de turbines hydroélectriques. Il a été constaté que le procédé de meulage avec ce robot n'est pas une action de coupe continue mais plutôt interrompue à chaque révolution de la meule. Ce comportement de coupe par impact apparaît en raison de la faible rigidité du manipulateur flexible soumis à des forces importantes de meulage. Par conséquent, une analyse détaillée a permis d'acquérir une meilleure compréhension du mécanisme d'enlèvement de matière lors du meulage robotisé. L'objectif de cette étude est donc d'établir des relations appropriées entre la formation des copeaux, les forces de coupe opérationnelles, la température, le taux d'enlèvement de matière et l'énergie consommée dans le procédé.

Cette étude vise aussi à utiliser des méthodes numériques et expérimentales dans le but d'acquérir une meilleure compréhension du procédé de meulage robotisé par robots flexibles. Tout d'abord, une analyse thermique par éléments finis est effectuée afin d'évaluer les paramètres thermiques du procédé tels que le coefficient de répartition des énergies et le champ de température dans la pièce à meuler. Une nouvelle représentation de la source de chaleur prenant en compte les effets d'impact du meulage robotisé est considérée dans le modèle. Un modèle de répartition des énergies entrant dans la pièce et dans la meule a été proposé à la suite des mesures expérimentales et des analyses numériques réalisées sous différentes conditions d'opération de meulage. Dans la seconde partie, la topographie des meules utilisées dans le procédé est caractérisée pour différentes profondeurs de coupe. Les arêtes de coupe des grains ont un effet significatif dans l'efficacité du procédé et sont essentielles à la compréhension de l'enlèvement de matière en meulage robotisé. La variation de la topographie de la meule en fonction des conditions d'opération a été démontrée. La détection des arêtes impliquées dans une action de coupe au cours du procédé est essentielle pour la modélisation à micro-échelle de l'enlèvement de matière se produisant dans la zone de contact entre la meule et la pièce. Les travaux en cours sur la modélisation de la force à micro-échelle par la méthode des éléments finis bénéficieront de cette étude de la topographie des meules. La troisième partie de cette thèse est consacrée à l'amélioration de l'identification empirique d'un modèle de force du procédé développé précédemment. Le régime de coupe d'impact est observé par les enregistrements des caméras à haute vitesse et

par le signal de force mesuré du procédé. Ce régime est détecté à différents niveaux de puissance de meulage et utilisé pour déterminer expérimentalement les paramètres du modèle de force. L'utilisation du modèle de répartition des énergies proposé dans la première partie de l'étude permet également d'obtenir un rapport d'énergies consommées entre le glissement et l'enlèvement de matière, qui sert à optimiser la détermination des constantes du modèle de force.

Mots clés : meulage robotisé, analyse par éléments finis, analyse thermique, modèle de force, coupe par impact, topographie le meule

TABLE OF CONTENTS

	Page
INTRODUCTION	1
CHAPTER 1 RESEARCH OUTLINES AND OBJECTIVES	3
1.1 Problem Definition.....	3
1.2 Scope of Study and Objectives	5
1.3 Background.....	7
1.3.1 Thermal modeling of grinding.....	7
1.3.2 Single-grit chip formation model for grinding.....	10
1.3.3 Grinding wheel topography	14
1.3.4 Grinding force model.....	16
1.4 Summary.....	18
CHAPTER 2 EXPERIMENTAL AND FINITE ELEMENT ANALYSIS OF TEMPERATURE AND ENERGY PARTITION TO THE WORKPIECE WHILE GRINDING WITH A FLEXIBLE ROBOT	21
2.1 Abstract.....	21
2.2 Introduction.....	22
2.3 Energy partition background.....	24
2.4 SCOMPI robot	26
2.4.1 Permanent magnets grinder.....	28
2.4.2 Motor losses.....	28
2.4.3 Influence of temperature.....	29
2.4.4 Motor parameter measurements.....	30
2.5 Modeling technique	31
2.5.1 Kinematic model.....	31
2.5.2 Heat input function	34
2.5.3 Finite element formulation.....	37
2.5.4 Finite element model.....	38
2.6 Experiments	39
2.7 Results and discussion	41
2.7.1 Energy partition results.....	41
2.7.2 Contact temperature results.....	48
2.8 Conclusions.....	51
2.9 Acknowledgements.....	51
2.10 References.....	51
CHAPTER 3 CHARACTERIZATION OF GRINDING WHEEL GRAIN TOPOGRAPHY UNDER DIFFERENT WORKING CONDITIONS IN A ROBOTIC GRINDING PROCESS USING CONFOCAL MICROSCOPE	55

3.1	Abstract.....	55
3.2	Introduction.....	56
3.3	Grain detection methods in wheel topography	59
3.4	Experiments and preparation	60
3.5	3D topography measurement	61
3.6	Data processing.....	63
3.7	Results and discussion	68
	3.7.1 Grain analyses.....	69
	3.7.2 Grain rake and yaw angles distribution	73
	3.7.3 Grain protrusion height and width	76
3.8	Conclusion and summary.....	77
3.9	Acknowledgements.....	78
3.10	References.....	78
 CHAPTER 4 FORCE MODEL FOR IMPACT CUTTING GRINDING WITH A FLEXIBLE ROBOTIC TOOL HOLDER		 81
4.1	Abstract.....	81
4.2	Introduction.....	82
4.3	Literature review.....	84
	4.3.1 Empirical models	84
	4.3.2 Grit based models	85
	4.3.3 Semi-analytical models.....	86
4.4	Grinding kinematics.....	88
4.5	Process force model	89
4.6	Test and measurements.....	90
	4.6.1 Test setup	91
4.7	Results and discussion	93
	4.7.1 Impact cutting regime	93
	4.7.2 Profilometer scans.....	98
4.8	Determination of model coefficients	100
	4.8.1 Friction and chip formation power	102
	4.8.2 Force and depth of cut.....	104
4.9	Conclusion	106
4.10	Acknowledgments.....	107
4.11	References.....	107
 CONCLUSION		 111
 RECOMENDATIONS		 115
 APPENDIX I Influences of Grit Shape and Cutting Edge on Material Removal Mechanism of a Single Abrasive in Flexible Robotic Grinding.....		 117
A I-1	Abstract.....	117
A I-2	Introduction.....	118
A I-3	Background.....	119
A I-4	Literature review	120

A I-5	Robotic grinding by SCOMPI robot.....	122
A I-6	Finite element model.....	125
A I-7	Material model.....	126
A I-8	Results and discussion	128
A I-9	Conclusion	132
A I-10	Acknowledgments.....	133
A I-11	References.....	133
	LIST OF REFERENCES.....	137

LIST OF TABLES

	Page
Table 2.1	Temperature-dependent material properties for stainless steel 304L39
Table 2.2	β values for the energy partition in power model46
Table 3.1	Statistics for the disk and cup wheel.....69
Table 4.1	β values and energy partition versus103
Table A I.1	J-C material constants for128
Table A I.2	J-C damage constants for128

LIST OF FIGURES

		Page
Figure 1-1	Schematic view of hydro turbine (Top-alternative-energy-sources, 2010)	.3
Figure 1-2	SCOMPI during on-site maintenance (Charles Gagnon, 2010)	4
Figure 1-3	Key inputs and outputs in macro-scale modeling of grinding process	8
Figure 1-4	Macro-scale thermal finite element model (Doman et al., 2009b)	9
Figure 1-5	Key inputs and outputs in micro-scale modeling of grinding process	10
Figure 1-6	a) 2D chip formation model, b) 3D chip formation model (T.T.Opoz, 2010)	13
Figure 1-7	Grit positioning in the grinding wheel a) standard wheel,	14
Figure 1-8	Effect of sampling distance in detecting the number of grains (Nguyen et Butler, 2008)	16
Figure 1-9	Hybrid force-position controller (Hazel et al., 2012b)	17
Figure 2-1	a) SCOMPI robot performing grinding operation during on-site blade modification to improve efficiency b) Laboratory setup with high-speed camera and lighting system	27
Figure 2-2	a) Grinder motor torque constant, $N=6000$ rpm, $\alpha=-0.1535$ %/°C, b) Grinder motor losses	31
Figure 2-3	Kinematics of cut	32
Figure 2-4	Heat input model for a) shallow grinding, b) creep-feed grinding, (Anderson et al., 2008a)	34
Figure 2-5	a) Heat input distribution, b) Uncut chip thickness over the wheel-workpiece interface	36
Figure 2-6	Impact heat input scheme	36

XVIII

Figure 2-7	a) SCOMPI robot experimental setup, b) Grinding trajectories (one layer of material removal).....	40
Figure 2-8	Position of subsurface thermocouples	40
Figure 2-9	a) Full-size workpiece FE simulation, b) Test rig for determining the energy partition ratio.....	42
Figure 2-10	Temperature-matching technique for finding the energy partition ratio, a, b) $P = 1,500 \text{ W}$, $V_f = 60 \text{ mm/s}$, depth = 5 mm; c, d) $P = 1,500 \text{ W}$, $V_f = 80 \text{ mm/s}$, depth = 12 mm	43
Figure 2-11	Energy partition ratio for different power levels and feed speeds	44
Figure 2-12	Energy partition fitting model.....	47
Figure 2-13	Experimental thermocouple temperature	48
Figure 2-14	Finite element temperature distribution in the workpiece contact zone a) One step before the impact-cut, b) Impact-cut step (Power = 1,500 W, Feed speed = 40 mm/s).....	49
Figure 2-15	Contact temperature from finite element analyses and tests.....	50
Figure 3-1	Laboratory setup of SCOMPI for grinding experiments, (a) disk wheel, (b) cup wheel.....	61
Figure 3-2	Samples of the grinding wheel prepared for measurements, (a) disk wheel, (b) cup wheel.....	61
Figure 3-3	(a) Confocal microscope with external light source, (b) disk wheel sample and (c) cup wheel.....	62
Figure 3-4	(a) Optical image (b) topography of the same region	63
Figure 3-5	Process for grinding wheel characterization	64
Figure 3-6	Optical image enhancement through histogram stretching, (a) raw image, (b) after stretching.....	65
Figure 3-7	(a) Butterworth filter, (b) original FFT image, (c) filtered FFT image.....	66
Figure 3-8	(a) One channel optical image of the wheel surface, (b) zoom of the region in red, (c) after high-frequency noise removal, (d) after mean shift filtering.....	67

Figure 3-9 (a) Optical image of grains, (b) binary mask of grains, (c) 3D topography of wheel as measured with the microscope, (d) 3D topography of grains with overlaid mask to remove the bonding region68

Figure 3-10 Pitch and yaw angle with respect to cutting direction70

Figure 3-11 Normal extraction with plane fit method, (a) good result (grain with one face), (b) ambiguous result (grain with two faces)71

Figure 3-12 a) Grain surface without normal vectors, b) grain surface with vertex normal vectors.....71

Figure 3-13 a) Height topography image, b) pitch angle for the whole grain (left), only the cutting face (right), c) yaw angle for the whole grain (left), only the cutting face (right).....72

Figure 3-14 a) Yaw angle distribution for the whole grain, b) for cutting face pixels, c) pitch angle distribution for cutting face pixels73

Figure 3-15 Distribution of (a) yaw angles and (b) rake angles at different power levels for disk wheel74

Figure 3-16 Distribution of (a) yaw angles and (b) rake angles in different grinding conditions for cup wheel.....75

Figure 3-17 Comparison of grain rake angle probability at different power levels for (a) disk wheel, (b) cup wheel76

Figure 3-18 (a) Grain protrusion and (b) grain width probability for disk wheel77

Figure 3-19 (a) Grain protrusion and (b) grain width probability for cup wheel77

Figure 4-1 Grinding kinematics, (a) traverse grinding, (b) idealized notch88

Figure 4-2 Test setup92

Figure 4-3 (a) Normal-speed video at 30 fps, (b) high-speed video at 6,000 fps, played at 30 fps (online version).....93

Figure 4-4 Angular speed and force measurements95

Figure 4-5 (a) Normal and (b) lateral force signal, (c) friction coefficient, (d) impact cutting map96

Figure 4-6	Impact regime at different power levels, (a) P = 500 W, (b) P = 1,000 W, (c) P = 1,500 W, (d) P = 2,000 W	98
Figure 4-7	Probability of number of impacts per turn	98
Figure 4-8	(a) Scanning the grooves, (b) top view of a groove (image and measured), (c) sample 3D view	99
Figure 4-9	(a) Analysis of scanned groove, (b) instantaneous MRR, (c) depth of cut	100
Figure 4-10	Synchronized data for (a) power consumption measured from robot controller, (b) MRR from groove scan data, (c) angular speed from DAQ.....	101
Figure 4-11	Error in cost function	102
Figure 4-12	Predicted and measured grinding power.....	104
Figure 4-13	Measured and predicted depth of cut at different power levels	105
Figure 4-14	Measured and predicted average force at different power levels	105
Figure A I-1	High speed camera setup used for observation of impact cutting	123
Figure A I-2	Kinematics of uncut chips at each impact.....	124
Figure A I-3	Surface of wheel a) 3D scan, b) Separated sections of wheel scan	124
Figure A I-4	2D profiles and rake angles.....	125
Figure A I-5	Finite element mesh	126
Figure A I-6	Von-Mises stresses, depth of cut = 20 ^{μm} a) rake angle = -10 degree, b) rake angle = -50 degree	129
Figure A I-7	Normal force versus cutting speed.....	129
Figure A I-8	Effect of initial temperature on cutting force.....	130
Figure A I-9	Temperature contour during the chip formation.....	130
Figure A I-10	Normal force versus depth of cut and rake angle	131
Figure A I-11	Cutting force versus depth of cut and rake angle.....	131

Figure A I-12 Force ratio versus depth of cut and rake angle132

LIST OF SYMBOLS AND UNITS OF MEASUREMENTS

Symbol	Units	Description
A	m^2	Instantaneous cross-section area of undeformed chip
B	Wb/m^2	Flux density in the grinder iron armature
C	J/K	Specific heat capacity
c	-	Color value for mean shift algorithm
\bar{c}	-	Average color value for mean shift algorithm
c_f	-	Normalized cut-off frequency in Butterworth kernel function
C_{Power}	%	Cost function for comparison of predicted and measured power
d_g	m	Average grain size
e_d	J/mm^2	Energy intensity function
E	m	Grinding wheel width
f	Hz	Rotational frequency
F_N	N	Instantaneous normal grinding force
\bar{F}_N	N	Average normal grinding force
F_T	N	Instantaneous tangential grinding force
\bar{F}_T	N	Average tangential grinding force
h	m	Depth of cut
h_0	m	Maximum depth of cut
H	J/mm^2	Heat flux distribution
I	A	Electrical current consumed by grinder
$K(S_i, S^k)$	-	Kernel function for mean shift algorithm
k, K	$W/(mK)$	Thermal conductivity
k_c	N/m^2	Cutting force coefficient
k_e	N/m	Edge force coefficient
k_{hys}	$W/(kgHz)$	Hysteresis loss coefficient
k_{eddy}	$W/(kgHz)$	Eddy loss coefficient
K_T	Nm/A	Torque constant of electrical grinder
$K_{T(T)}$	Nm/A	Torque constant at a given temperature T
$K_{T(T_{ref})}$	Nm/A	Torque constant at the reference temperature T_{ref}
M	-	Grit size
n	-	Butterworth filter power
n_c	-	Number of impacts per revolution
N	Hz	Rotational frequency
P	W	Grinding power
P_m	W	Measured grinding power
\bar{P}_m	W	Mean measured grinding power

P_M	W	Evaluated mechanical grinder power
$P_{friction}$	W	Evaluated mechanical power to overcome friction
P_{chip}	W	Evaluated mechanical power to form the chip
P_{Drag}	W	Power lost in drag and friction in grinder bearings
P_{Fan}	W	Power consumed to drives cooling fan in grinder
P_{Core}	W	Power lost in the stator iron armature
Q	Nm	Nominal delivered torque at the grinder spindle
r	-	Normalized distance from center in Butterworth kernel function
R	m	Grinding wheel radius
R_0	m	Maximum grinding wheel radius
S, S_{chip}	m^2	Surface of the uncut chip
S^k, S^{k+1}	-	Pixel coordinate and color value in mean shift algorithm
t	s	Time
T	K	Temperature
$T_{\bar{\theta}}$	K/m	Temperature gradient
T_{ref}	K	Reference temperature
u	J/m^3	Grinding specific energy
u_{ch}	J/m^3	Chip formation specific energy
u_{pl}	J/m^3	Plowing specific energy
u_{sl}	J/m^3	Sliding specific energy
v_f	m/s	Feed speed of the robot
V, V_{chip}	m^3	Volume of the uncut chip
V_s	m/s	Peripheral speed of the grinding wheel
w	m	Width of cut
x	m	Instantaneous undeformed chip width
X	m	Longitudinal coordinate of the groove
Δx	m	Wheel advance per turn in feed direction
Z_w	m^3/s	Material removal rate
α_T	$\%/C$	Negative reversible temperature coefficient
α	-	Energy partition model coefficient
β	-	Energy partition model coefficient
γ	m	Abrasive grit width
ρ	Kg/m^3	Mass density
ε	-	Energy partition ratio
δ	m	Uncut chip thickness
θ	rad	Cutting angle
μ	-	Friction coefficient
ω	rad/s	Rotational speed of grinder spindle
φ	rad	Immersion angle

INTRODUCTION

All machining operations involve a material removal process. Although the process varies in different types of machining, understanding this removal mechanism is a key step toward achieving higher efficiency in the process. Grinding, unlike other machining processes, can be defined as fairly shallow removal of material, usually in order to reach high accuracy in the finishing phases of manufacturing or rectifying processes. Grinding is among the most important machining processes because it is performed in the final stages of manufacturing and has a direct effect on product quality. Efforts in modeling and simulating this process can thus yield a significant practical return on investment.

Numerical methods like finite element analysis (FEA) have been applied to a wide range of engineering fields to model and simulate many physical phenomena. Empirical models are also commonly used to predict any complex process for which there is no possible analytical solution. Both methods have thus become strong tools in industry in order to predict and understand process behavior and to reduce trial-and-error practices.

The fact that the material removal process in grinding is composed of innumerable micro-cutting actions by random grains makes grinding a difficult task to model. This difficulty becomes even more challenging when a flexible robot is the manipulator holding the grinder. Dynamic effects and stiffness of the robot structure add to problem complexity. Hence, a comprehensive study of the robotic grinding process is necessary and must consider the flexible holding structure of the grinding robot.

Organization of thesis

This research work is presented as a manuscript-based thesis and divided into four chapters. Chapter 1 gives information about the problem providing the basis for this research, outlines the research and states the objectives defining the scope of study. Background to this

research work is also discussed. The methodology followed is described, emphasizing major assumptions and considerations for each model.

Chapter 2 presents the first journal article. A thermal finite element model is developed to obtain the temperature distributions in the workpiece during the robotic grinding process. The effects of different loading conditions and the particular cutting regime occurring with the robot under study are considered under the boundary conditions applied. An energy partition model applicable to the process is introduced and verified through a series of tests. Temperature results from the model showed good agreement with the test results.

Chapter 3 presents the second journal article. In this work, the grain topography of the grinding wheels used in the process is obtained. A new method is developed for distinguishing the grains from the bonding material using image processing techniques in overlaid optical images of the measured surface. Having thus determined the geometry of individual grains, the yaw and rake angles of the grain faces involved in the cutting action are extracted. The distribution and mean value of these angles are evaluated under different operating conditions. The grain geometry data is vital for micro-scale simulation of the cutting action in the grinding process. This is an ongoing area of research in this project.

Chapter 4 presents the third journal article. Enhancements are made in determining the empirical coefficients of an existing force model for the process. Grinding with the robot under study was seen to be interrupted at each revolution of the wheel. The number of impacts per turn is determined at different grinding power levels through tests in which the force signal is measured. Also, using the friction-chip energy ratio of the process obtained in the first article, the empirical coefficients to use are more closely determined. The predicted depth of cut and average normal force showed a very close correlation with the results from test measurements.

The conclusion and recommendations are provided at the end of this thesis.

CHAPTER 1

RESEARCH OUTLINES AND OBJECTIVES

1.1 Problem definition

Hydro turbines have been widely used for power generation for many years in North America. With about 40% of Canada's water resources, Québec provides a major portion of the electricity generated by hydropower (Hydro-Québec, 2010). Figure 1-1 shows a view of a typical hydro turbine and its generator.

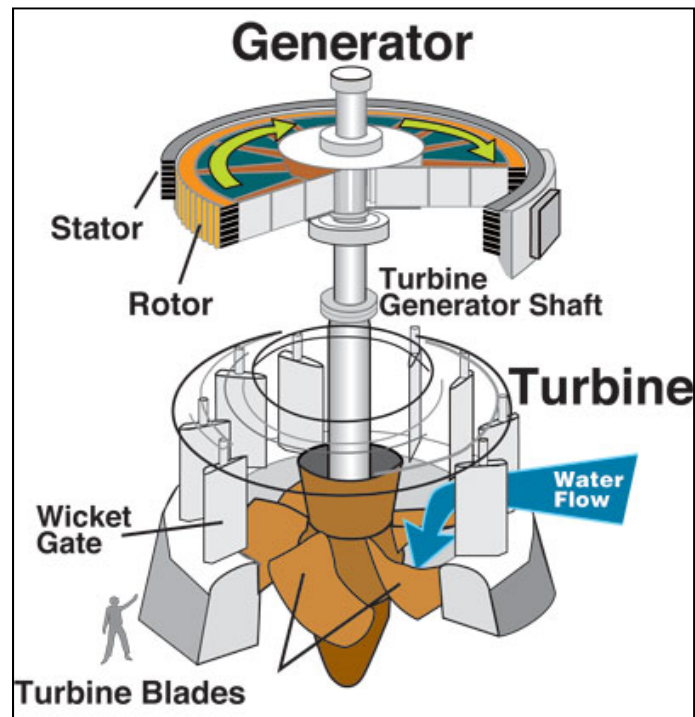


Figure 1-1 Schematic view of hydro turbine
(Top-alternative-energy-sources, 2010)

One typical type of damage to hydro turbines is cavitation on turbine blades, which is a major problem in turbine maintenance. High repair costs for these blades and the long repair time due to their enormous size have long been a major issue. In the late 1970s, Hydro-Québec started designing a robot capable of handling the entire repair procedure for cracks

and defects in turbine blades. The robot was developed by IREQ, Hydro-Québec's research institute. It has the ability to reach otherwise inaccessible areas of the installed blade without requiring their disassembly (see Figure 1-2) (Hydro-Québec, 2004). To achieve such versatility, a light-weight, flexible robot was required to meet the need for on-site maintenance of hydro turbine blades. The robot developed has effectively reduced turbine down time and saved a considerable amount of money during turbine maintenance. The robot is named "SCOMPI", which stands for "Super COMPact Ireq robot". With a total weight of about 33 kg, it has 6 degrees of freedom and is capable of performing on-site plasma gouging, welding, grinding and hammer pinning. The grinding process with this robot is designed for parts in difficult-to-reach locations, such as turbine blades, or unmovable parts in special environments, like underwater gates. It is difficult or even impossible to grind such parts with conventional grinding machines due to their surroundings.



Figure 1-2 SCOMPI during on-site maintenance
(Charles Gagnon, 2010)

Because of its light-weight design, the robot has a low-stiffness structure given the task force compared to conventional grinding machines. Consequently, unwanted vibrations and deformation of the arm are likely to occur during the process. Due to the robot's characteristics, loss of accuracy and non-uniform material removal may result when grinding.

Since a fine surface finish and accurate dimensions are essential for efficient turbine blades, the grinding process with SCOMPI requires great care. The desired material removal is achieved through a multi-step procedure with dimensions controlled precisely at each step.

1.2 Scope of study and objectives

In order to improve process efficiency, a better understanding of the robotic grinding process discussed above is crucial. The main purpose of this research is to improve the quality and precision of grinding performed by SCOMPI. The goal is thus to develop or improve numerical and empirical models in order to better predict the process.

An important issue in all grinding processes is thermal defects in the workpiece due to excessive heat generated during the process. This may be even more important when grinding is performed by robots due to the more dynamic nature of robotic grinding. Hence, the first part of this work relates to thermal aspect of the process. This includes quantifying heat input to the workpiece using finite element analysis and testing. FE simulations of grinding usually ignore the dynamic effect of the holder's structure. This assumption is made based on conventional grinding machines with a rigid structure. Boundary conditions related to the parts attached to the machine are thus assumed constant. In robotic grinding and especially with the light, flexible structures in this study, the effects of low manipulator stiffness cannot be ignored in simulations. If the structure of the machine is not rigid, the depth of cut will not stay constant. Plastic work, friction forces and generated heat may also vary over time. Thermal simulations must include heat flux dynamics for appropriate solutions. Therefore as of the first objective, a macro-scale FE model is developed with dynamic boundary conditions representing the robotic grinding process. The aim is to investigate the temperature distribution in the workpiece due to the process. The results are expected to make it possible to predict any thermal defects produced in the workpiece due to the dynamics of robotic grinding.

Another step toward acquiring the necessary understanding of the process is to have a micro-scale view of the grinding process. Material removal in grinding is a combination of numerous micro-cuts in the wheel-workpiece contact zone. Microscopic modeling of grinding focuses on the effects and interactions between individual grains and the workpiece surface. It is thus crucial to investigate the geometry of cutting edges, meaning the orientation and protrusion of grains. The second objective of this study is to characterize two wheels commonly used in the SCOMPI grinding process. A non-contact method with a confocal scanning laser microscope is used to obtain the wheel topography. The necessary steps are taken to remove the bonding material from measurements. Grinding wheels are characterized under different operating conditions. A comprehensive view of the wheel topography is achieved, including grain density, grain width and protrusion height, as well as the rake and yaw angles of the attacking faces of grains. The resulting geometry of cutting edges from this study will be used in a future study for micro-scale simulation of the process.

The last part of this study is devoted to an empirical model for force prediction at a specific material removal rate. As mentioned earlier, the main difference between conventional grinding and robotic grinding is tool holder rigidity. Lower rigidity causes non-uniform material removal during robotic grinding. An accurate force model that considers the correct process dynamics will thus help the robot controller to better maintain desired process characteristics like depth of cut. An existing force model is further analyzed with an emphasis on the effect of cutting regime and energy concepts.

In conclusion, a FE macro-scale model is developed to determine temperature distribution in the workpiece during the process. The thermal results are used to predict thermal damage and evaluate material behavior for a FE micro-scale model. In order to properly investigate material removal mechanism by the micro-scale model, having the information of cutting edge in the grinding wheel is necessary. Therefore, wheel topography study is performed and statistical geometries of grains are extracted. Finally, some enhancement on the process force model is performed to improve process quality and precision.

1.3 Background

Numerical simulation is more complex to perform for grinding than for other machining processes. The reason is the random size and shape of the grits and their cutting edges. Basically, two approaches are employed to overcome this difficulty. One approach is to investigate the process through macro-scale simulations in which there is no need to know the geometry of cutting edges. Instead, the effect of the cutting process is applied in the model without going into details regarding the material removal process. In the resulting models, the effect of the grinding wheel is usually represented by a heat source moving over the workpiece surface (Jaeger, 1942). The other approach is to investigate the process through micro-scale simulations which focus on interactions between a single grit and the workpiece surface. While macro-scale models are more of a general look at the process, micro-scale models deal with the details of grain-workpiece interaction. (Brinksmeier et al., 2006; Doman et al., 2009b; Mackerle, 2003) have produced thorough reviews of finite element simulations of machining and grinding.

1.3.1 Thermal modeling of grinding

Early measurements of grinding forces and specific energy in the 1950s revealed that grinding has higher specific energy than other machining processes like turning or milling (Stephen Malkin, 2008). This means that for a specific volume of material removed by grinding, much more power is consumed than by any other machining process. Commonly, much more heat is thus generated, and consequently the rise in workpiece temperature is greater. If the temperature exceeds a critical limit, phase transformation occurs in the workpiece. Due to this phase transformation, brittle untempered martensite is formed on the surface. This is referred to as “workpiece burn” and has a bluish color. The thickness of this martensite layer depends on the amount of heat applied and how readily it is conducted through the workpiece (Malkin and Guo, 2007). Other thermal defects in the workpiece due to high temperature are micro-cracks, residual stresses, warping, bending and twisting. That

is why thermal damage is of utmost concern in the grinding processes and the subject of considerable study.

Figure 1-3 shows the key inputs to and expected results from a general macro-scale model of robotic grinding. However, only thermal aspects of macro-scale modeling are investigated in this thesis. As explained earlier, an important parameter to consider in quantifying heat flux is the energy partition to the workpiece (Chen and Xu, 2010; Hadad et al., 2012; Kohli et al., 1995). A correlation for the heat flux is derived, usually based on the consumed power or specific energy, and calibrated using test data for the process condition (Guo and Malkin, 1999; Mohamed et al., 2011).

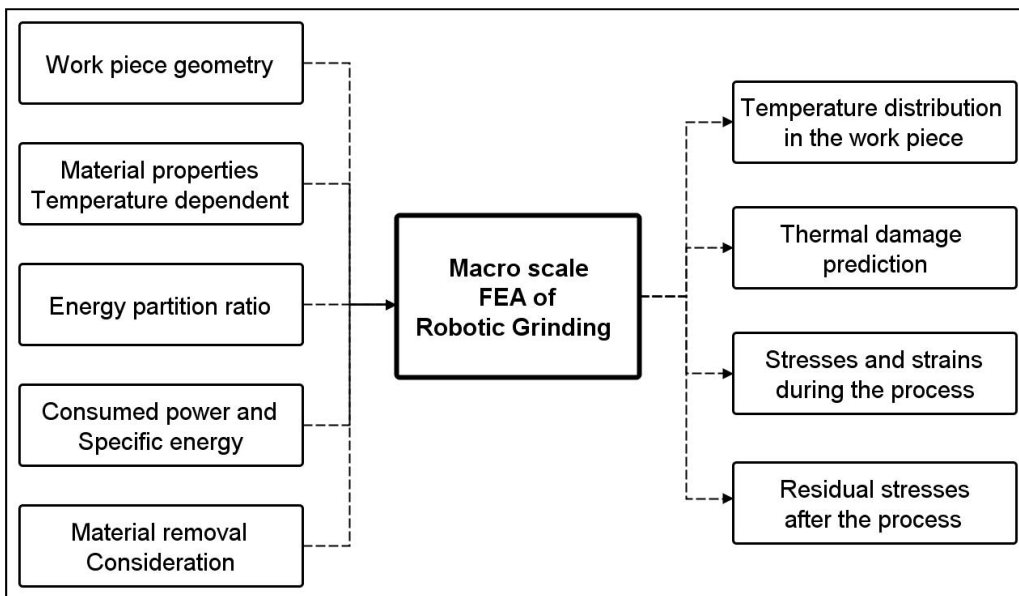


Figure 1-3 Key inputs and outputs in macro-scale modeling of grinding process

In macro-scale models, the finite element mesh covers the workpiece. The cutting zone is considered to be a very thin area compared to the workpiece. The grinding wheel is then represented by a heat flux moving along the workpiece surface. The heat flux may have different distributions, like uniform or triangular, based on the grinding parameters. The effects of a liquid coolant or natural air cooling are modeled by heat convection on the surface of workpiece (Hoffmeister and Weber, 1999; Li and Li, 2005; Mahdi and Liangchi,

1995; Mao et al., 2010; Parente et al., 2012). The general model with different heat fluxes is shown in Figure 1-4. Given the impact cutting phenomenon and dynamic force response in robotic grinding, real dynamic power consumption must be considered rather than just the mean value since it affects directly the heat flux entering the workpiece. The applied heat flux is thus not constant over time as it progresses across the workpiece surface.

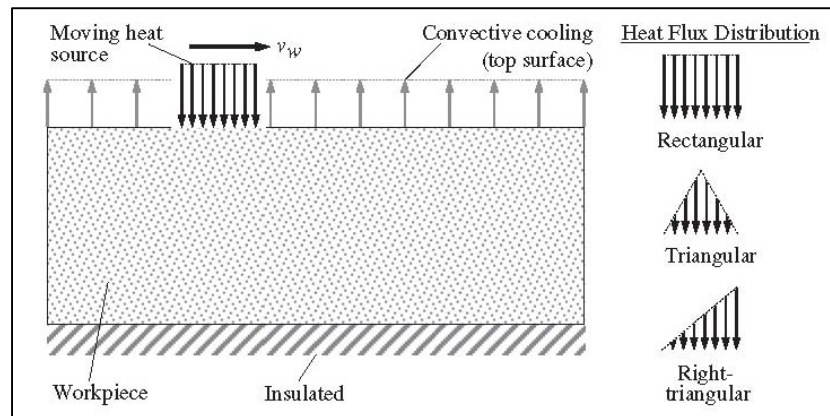


Figure 1-4 Macro-scale thermal finite element model
(Doman et al., 2009b)

Any numerical simulation must be validated through tests or analytical solutions. Online temperature measurement during grinding is the most trustworthy test method for validating thermal simulations of the grinding process. In fact, temperature measurement during grinding is not only crucial to validate thermal simulation results but is also needed to investigate and determine the energy partition for heat modeling (Kohli et al., 1995). Grinder power consumption should also be recorded to obtain the specific energy of the process. This is necessary for calculating the energy partition ratio.

The heat generated in the grinding process is highly transient and close to the wheel contact area. A highly sensitive sensor should thus be placed near this area to measure the actual temperature impinging on the workpiece material. Common temperature measurement techniques used for grinding are embedded foil thermocouples and thermal imaging. Thermocouples are frequently used to validate thermal simulations of the grinding process (Dai et al., 2000; Lefebvre et al., 2012; Li and Li, 2005; Wang et al., 2003). They have

proven to be a fast, appropriate measuring tool for such transient thermal conditions. The other common method mentioned, thermal imaging, involves measuring the infrared radiation emitted from the workpiece by means of a thermal camera or any other appropriate CCD sensor (Anderson et al., 2008b; Hwang et al., 2003; Mohamed et al., 2012a). The primary drawback in thermal imaging is the interference of any other body, which blocks radiation from the main object. Depending on the workpiece and process conditions, both methods have been extensively used in earlier studies.

1.3.2 Single-grit chip formation model for grinding

The other approach in grinding simulations is micro-scale FE modeling of the process. The purpose is to develop a finite element model capable of simulating chip formation and finding the appropriate relations among applied force, friction and local plastic deformations in the contact area for individual grains. Micro-scale modeling of grinding involves large deformations in geometry, in addition to material and boundary non-linearity. Figure 1-5 shows the key inputs that should be provided for a micro-scale model of robotic grinding as well as the expected results.

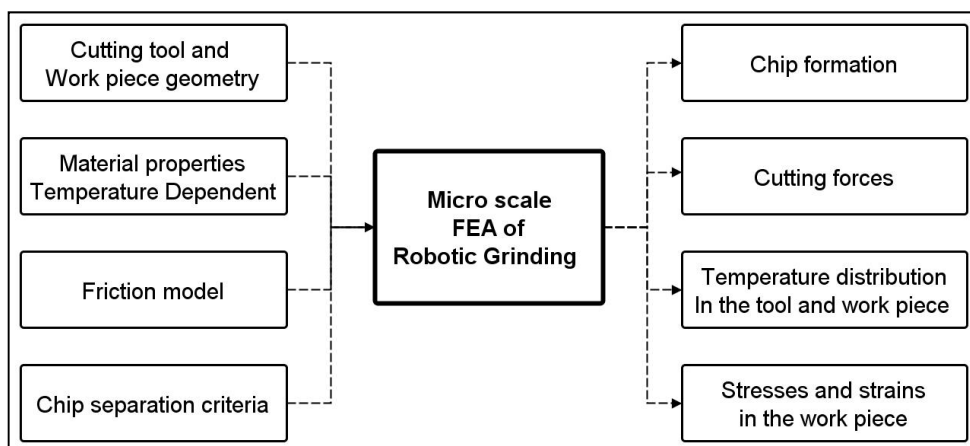


Figure 1-5 Key inputs and outputs in micro-scale modeling of grinding process

Three important general aspects to be considered in finite element simulations of all metal cutting processes are material behavior, the friction model and the chip separation criterion. Since very large deformations and high heat generation usually occur simultaneously in the process, selecting the appropriate material model is crucial. Furthermore, friction and the chip separation criterion play major roles in chip formation, cutting forces and generated heat in finite element simulations.

Material behavior in metal cutting is known to be one of the dilemmas in simulating the process. Due to excessive strain, large strain rate and high temperature, the material does not respond by common elastic-plastic behavior. One well-known model of plasticity, the visco-plastic model, has been found to be most appropriate. Numerous constitutive models in the literature have been used by researchers to determine the visco-plastic material flow in machining processes. In most of them, the influences of strain rate and temperature are considered for calculating the effective stresses. (Fang, 2005a) compared 18 engineering materials and concluded that strain rate hardening has less effect on flow stress than the other factors, i.e., strain hardening and thermal softening. A list of common constitutive material models for stress flow can be found in (Grzesik, 2008). The most important and commonly used material models are those of (Zerilli and Armstrong, 1987), (Oxley, 1989) and (Johnson and Cook, 1985b).

In simulating the chip formation phenomenon, as the tool advances into the workpiece, the material ahead of the tool tip must be pushed away so that the chip and new surface can form. This involves separation of the finite element mesh during the solution. Basically, in order to handle material separation in finite element models, three techniques have been used: node separation criteria (geometrical or physical), adaptive re-meshing and element deletion with a damage law. Any one or a combination of these techniques can be implemented to form the chip in metal cutting simulations. Node separation criteria are based on splitting nodes on a predefined path. Separation occurs when a specified law or rule is satisfied. Studies have used various physical parameters for separation thresholds (Carroll and Strenkowski, 1988; Iwata et al., 1984; Lin and Lin, 1992). Adaptive re-meshing is a local

(Ozel and Zeren, 2005) or global re-meshing (Yen et al., 2004) of the workpiece with respect to an activation criterion, i.e., a limit for change of angles in elements or a constant time interval. In element deletion, a damage law is applied to control the elements in the distorted zones. Any element that reaches the limit is deleted from the mesh. The most well-known damage law and one frequently used in metal cutting simulations is that of (Johnson and Cook, 1985a). This damage law has been implemented in several metal cutting simulations for chip formation modeling (Guo and Yen, 2004; J. Zouhar, 2008; Pantalé et al., 2004; Zeren, 2004).

The other major aspect in FE simulation of metal cutting processes is the tool-workpiece friction model, which is still a matter of interest in recent studies. According to (Ozel and Altan, 2000), in conventional machining, friction exists in two locations: between the flank face of the tool and finished surface of the workpiece, and between the rake face of the tool and the chip formed. However, in high-speed machining like orthogonal cutting and grinding, flank face friction is much lower than rake face friction. The effective friction in high-speed machining and grinding will thus only be between rake face of the tool and the chip formed. Basically, two distinctive zones in the contact region of the rake face are considered: a sticking region near the tool tip and a sliding region over the remaining contact length. Friction in the sliding region is explained by Coulomb's law. However, since friction force clearly cannot exceed the shear limit of material, friction is constant and equal to the shear limit in the sticking region. This is one of the basic models. Many other studies deal with this matter (Arrazola et al., 2008; Arrazola and Özel, 2010; Bonnet et al., 2008; Ozel, 2006; Shi et al., 2002).

From a simulation standpoint, the metal cutting process closest to material removal in grinding is orthogonal cutting with a negative rake angle. (Sevier et al., 2007) used finite element analysis to investigate the plastic deformations caused by machining, considering a wide range of rake angles (-50 to +50 degrees) in their simulations. (Ohbuchi and Obikawa, 2003) also tried to simulate the grinding mechanism by introducing a FE model of orthogonal cutting with a large negative angle and an updated Lagrangian formulation. The authors

found that the cutting speed and grinding parameters like depth of cut greatly influence the chip formation process. In another study, (Doman et al., 2009a) presented a three-dimensional FE model to investigate the sliding and plowing phases of material removal in grinding. The normal and tangential forces from the FE model were compared to scratch test results to validate the model proposed. (T.T.Opoz, 2010) considered a negative-rake-angle tool in orthogonal cutting to represent single-grit cutting in grinding. An explicit solver is utilized, and the Johnson-Cook (J-C) material model is applied in conjunction with the J-C damage law to perform the chip formation process. 2D and 3D models are simulated by means of the ALE formulation and adaptive re-meshing technique to avoid element distortion. It is confirmed that J-C is a suitable material and damage model for machining processes. Figure 1-6 shows the stress contour in 2D and 3D simulations from this study.

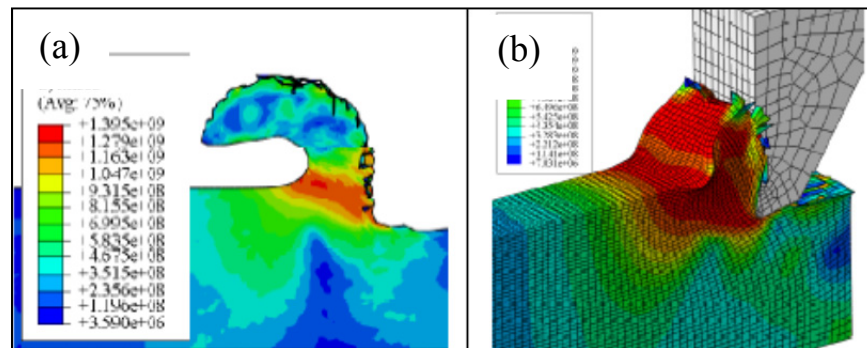


Figure 1-6 a) 2D chip formation model, b) 3D chip formation model (T.T.Opoz, 2010)

Extensive finite element studies have been conducted on chip formation in other types of machining processes (Altan and Vazquez, 1997; Mackerle, 2003; Mackerle, 1998). Chip formation modeling in grinding remains a complex problem, however, due to the random position and unpredictable geometry of grains. One solution implemented to solve this problem is to modify the finite element model of chip formation in other machining processes in a way that represents the single-grain action in grinding. Study in this field is clearly lacking and most grinding FE simulations focus on macro-scale modeling of the process.

1.3.3 Grinding wheel topography

Grinding wheels are composed of innumerable tiny abrasive particles, which remove material from a surface. Although some recent efforts have been directed toward positioning abrasive particles in specific patterns on the surface of grinding wheels (Aurich et al., 2003; Aurich et al., 2008), in most conventional wheels, the particles, named “grains” or “grits”, are positioned randomly in the wheel structure and have different shapes and edge angles (see Figure 1-7). That is why the grinding process remains among the least understood manufacturing processes and is extremely difficult to model. In order to overcome this difficulty, grinding wheel surface characteristics must be determined, a necessary step for any sort of micro-scale simulation of grinding. This means determining the geometry of cutting edges as well as the position and density of grains. There are basically three main groups of studies that employ different strategies to deal with this random cutting edge problem.

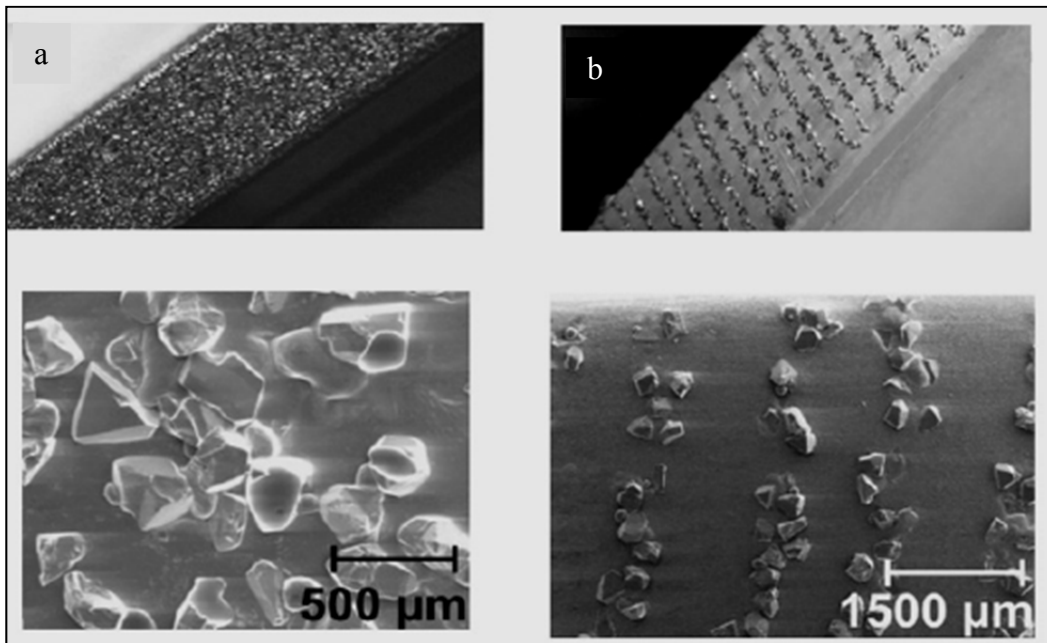


Figure 1-7 Grit positioning in the grinding wheel a) standard wheel, b) defined-grain-pattern wheel (Aurich et al., 2008)

The first group of studies assumes that grains are of some basic shape, such as spheres, pyramids, cones or prisms (Badger and Torrance, 2000; Fengfeng and Zhou, 2005; Transchel et al., 2014). The second group of studies develops a mathematical description for the wheel topography based on virtual grinding wheel modeling. The mathematical models are developed for different types of wheel, like diamond wheels (Koshy et al., 1993; 1997), CBN wheels (Li et al., 2013), etc. The grinding wheel topography models developed in this group cover a wide range: from 1D and 2D models to 3D representations of wheel surface (Doman et al., 2006). These models are generally used for kinematic analysis of the grinding process (Liu et al., 2013; Nguyen and Butler, 2005). The third group of studies focuses on obtaining the wheel topography from direct measurements of the wheel's surface. There are two main measurement methods: contact and non-contact (Darafon, 2013). In both methods, an important initial step is to separate grain topography data from the bonding data. This is achieved either by preparation of wheel to remove the bonding material before measurement (Xie et al., 2011) or by applying detection and filtering techniques after measurement (Darafon et al., 2013). In most contact methods, it is hard to distinguish between the grains and the bonding material. Some studies use a method called "highest point among eight neighbors" to define the grains. This introduces another difficulty, i.e., the need to use an optimum sampling distance. If the sampling distance chosen is smaller than the optimum value, the number of grains may be overestimated by instead detecting the cutting edges (Blunt and Ebdon, 1996). Figure 1-8 illustrates how the sampling distance affects the grain count by the "highest point among eight neighbors" method.

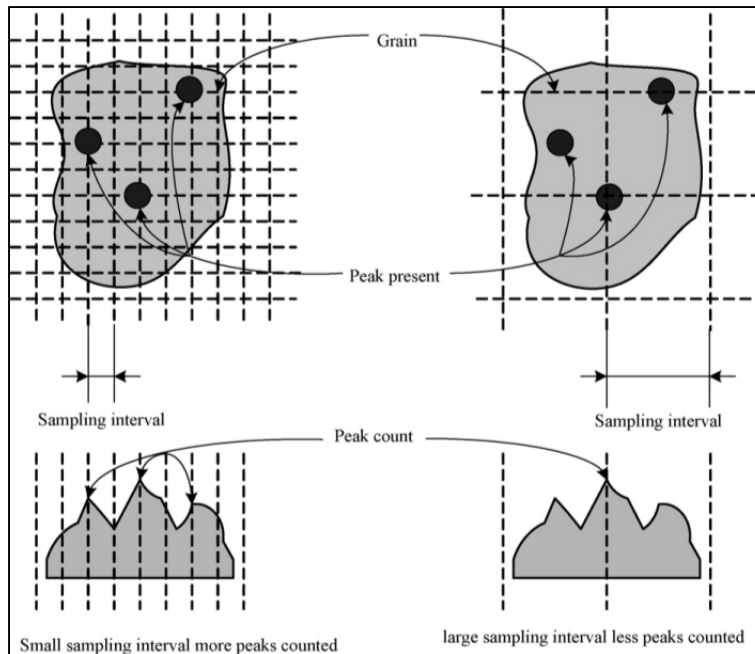


Figure 1-8 Effect of sampling distance in detecting the number of grains (Nguyen and Butler, 2008)

In non-contact methods, grain detection can be performed using the intensity of the reflected measuring beam. However, this is applicable only if grains have high reflectivity in order to differentiate them from the bonding material, as in diamond wheels (Cui et al., 2013). Environmental light may also affect the results. Another method is to use a scanning electron microscope (SEM), which makes it possible to distinguish between the grains and bonding material (Kapłonek and Nadolny, 2013). The small chamber for specimens and the high costs of a SEM are disadvantages of this method.

1.3.4 Grinding force model

As explained earlier, the robotic grinding under study is for field repair purposes on hydropower equipment. The process is designed to perform high material removal rate grinding as well as attain high surface finish quality and accuracy. The robot's flexibility due to its light-weight structure and track-based design leads to material removal through impact cutting. Conventional position control systems thus cannot be employed here to achieve high

removal rates and high precision. Instead, a hybrid force-position controlled material removal rate (CMRR) strategy is used to obtain the final profile (Hazel et al., 2012a). The grinding force model is a crucial part of this CMRR strategy. Special care must be taken to ensure that all dynamic effects caused by low robot rigidity are included in the force model. In other words, the desired material removal rate (MRR) is obtained by regulating the grinding power. The force model provides the correlation between the MRR and grinding power.

Figure 1-9 is a block diagram of the controller. First, the task planner calculates the desired MRR for the target depth of cut based on the process kinematics and other related parameters, such as wheel geometry. Second, the calculated MRR is correlated to the target force and grinding power that are used to control the robot. A wheel wear model is also employed to apply the necessary adjustments due to changes in wheel geometry during the process.

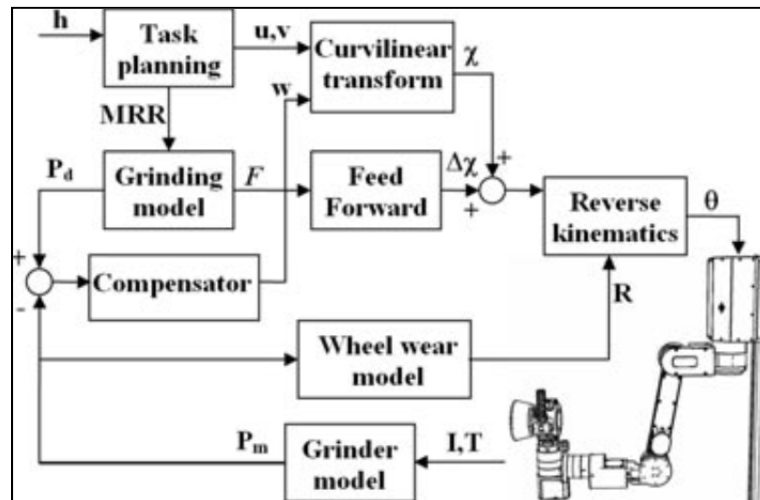


Figure 1-9 Hybrid force-position controller (Hazel et al., 2012b)

(Brinksmeier et al., 2006; Tönshoff et al., 1992) summarized early grinding studies in the literature. Some are based on comparative experiments with no mathematical expression for force (Malkin and Cook, 1971). Others tried to establish a mathematical expression to predict the force based on chip thickness (Snoeys et al., 1974), the stochastic distribution of

cutting edges (Werner, 1973) or chip formation and friction concepts (Lichun et al., 1980). However, these models all lack the effects of grinding time and coolant.

Generally, since random grains participate in the grinding removal action, it is impossible to develop a fully analytical force model for the grinding process. The dynamics of robotic grinding also make force prediction more difficult. Most grinding force models fall into one of three categories: empirical, semi-analytical or grit-based. Empirical models propose a mathematical model for force, composed of major process parameters supplemented by regression exponents and multipliers determined experimentally (Johnson et al., 2008; Liu et al., 2008; Mishra and Salonitis, 2013; Winter et al., 2014). Although empirical force models are widely used for industrial applications, their coefficients must be determined for each specific operating condition. Their main drawback is thus the time and cost of tests needed for each combination of grinding wheel and workpiece material. While empirical models largely depend on test data, semi-analytical models reduce this dependency by incorporating process kinematics into the model. These models are normally supported by an analytical chip thickness model (Agarwal and Venkateswara Rao, 2013). Certain studies in this category construct the force model from chip formation, friction and sometimes plowing components (Patnaik Durgumahanti et al., 2010; Yao et al., 2014). The third category of grinding force models is based on the micro-interaction between wheel and workpiece. Single-grit cutting force models are developed and extended based on a wheel topography model to obtain the overall grinding force (Chang and Wang, 2008; Hecker et al., 2007; Wang et al., 2014).

1.4 Summary

This section explained the initial reasons and drivers for the research project. The scope of this study and areas of research were also outlined. Then background was presented on other work related to this research problem.

Two grinding FE modeling approaches, i.e., macro-scale and micro-scale, were introduced. Key inputs and outputs of these approaches to modeling robotic grinding were explained. Though numerous studies have been conducted on the simulation of metal cutting processes and conventional grinding, less attention has been given to dynamic conditions in FE modeling of robotic grinding. After reviewing several studies in this area, the author found no FE model specifically related to the material removal mechanism in robotic grinding.

The importance of studying grinding wheel topography was highlighted. Contact and non-contact methods in the literature used for measuring wheel topography were briefly introduced. Though many methods have been used by researchers to develop the requisite knowledge of cutting edges in grinding process, there is still room for developments, especially regarding techniques for distinguishing grains from the bonding material. Also, no study was found on grinding wheel topography that considered only the attack side of the grains for characterization purposes.

Why the control strategy (CMRR) used for the process requires an accurate force model is clarified. The force models for conventional grinding in the literature include empirical, semi-analytical and grit-based models. Since the conventional force models are not applicable to the robotic grinding process under study, an appropriate force model is essential in order that the process achieves both high surface quality and accuracy. The dynamics of the robot is at the core of this force model. The next three sections of this thesis present developments and the results obtained in this research in the form of three journal articles published or submitted for publication.

CHAPTER 2

EXPERIMENTAL AND FINITE ELEMENT ANALYSIS OF TEMPERATURE AND ENERGY PARTITION TO THE WORKPIECE WHILE GRINDING WITH A FLEXIBLE ROBOT

Amir Masoud Tahvilian¹, Zhaoheng Liu^{1*}, Henri Champlaud¹, Bruce Hazel²

⁽¹⁾Department of Mechanical Engineering, École de technologie supérieure,
Montréal, Québec, H3C 1K3, Canada

⁽²⁾Expertise Robotique et civil, IREQ, Hydro-Québec's research institute
Varenes, Québec, J3X 1S1, Canada

This article is published in “Journal of Materials Processing Technology”, volume 213, issue 12, December 2013, Pages 2292-2303

Highlights

- A new representation of heat source is developed for thermal analysis of a flexible robotic grinding.
- Energy partition ratio is adjusted for a flexible robotic grinding using temperature-matching technique.
- A modified empirical model from the literature and a new formula are proposed to determine the energy partition applicable to this study.
- Dynamic effect of robotic grinding predicted temperatures 15% higher than when average parameters are considered.

2.1 Abstract

Grinding processes performed with flexible robotic tool holders are very unlike conventional types of grinding because of low stiffness of the robot's structure. A special flexible robotic grinding process is used for in situ maintenance of large hydroelectric equipment for bulk material removal over large areas rather than as a finishing step, as is the case for most

conventional grindings. Due to the low structural stiffness of tool holder, cutting is interrupted at each revolution of wheel during the grinding process. In this study, an investigation is carried out to determine the temperatures and energy partition to the workpiece for the above-mentioned flexible robotic grinding process by a three-dimensional finite element thermal model. Experiments were undertaken using embedded thermocouples to obtain the subsurface temperature at several points in the workpiece during the process. Then, energy partition to the workpiece was evaluated using a temperature-matching method between the experimental and numerical results. This ratio is used for predicting the temperature field at the wheel-workpiece interface with a relevant heat source function. Kinematics of cut and the flexible robot's dynamic behavior are considered in applying the heat input to the model. The energy partition to the workpiece in this specific flexible grinding process is found to be lower than for analogous conventional precision grinding processes. Two models, one from the literature and one from the power model of the process, are modified and proposed for determining the energy partition. The results showed that the energy partition ratio decreases by increasing the process power. Also, this ratio slightly decreases at higher feed speeds. In addition, lower temperatures were seen at higher powers due to the lower intensity of heat input over a larger contact area. Experimental observations show close agreement between simulated contact temperatures and measured results.

Keywords: Robotic grinding; finite element analysis; energy partition; contact temperature

2.2 Introduction

Grinding has much larger specific energy in material removal than other machining processes, leading to a higher temperature at the wheel-workpiece interface. High temperature can cause thermal damage, such as burning and phase transformation, which adversely affect workpiece surface characteristics. High temperature is also an important factor in grinding wheel wear rates and significantly affects the mechanical behavior of workpiece material due to thermal softening effects. Many studies have been conducted to

determine the temperature field in the workpiece during conventional grinding processes. They are usually based on a model by Jaeger (1942), who proposed a heat source of constant intensity moving over a semi-infinite workpiece surface. Brinksmeier et al. (2006) presented an overview of all types of models and simulations for grinding process, including analytical and numerical models.

Thermal simulation of the grinding process generally involves measuring the power consumed during the process, determining the ratio of energy transported into the workpiece and defining the heat input function for the particular surface. The most challenging of these three tasks is determining the energy partition into the workpiece for all grinding parameters and conditions. Rowe et al. (1988) were among the first who introduced the concept of heat partitioning in thermal modeling of grinding process. The four main sources of heat dissipation in the grinding process are the grinding wheel, the workpiece, chips and coolant. Specifying the amount of heat entering the workpiece is a key rule for any thermal simulation of grinding processes.

Finite element (FE) methods have proven to be a reliable approach and are used extensively by researchers for thermal simulations of grinding. Several FE models with different heat functions are used to predict the temperature distribution in the workpiece. Doman et al. (2009b) summarized some FE approaches used for grinding modeling and categorized them into macro- and micro-scale models. Early simulations made a number of simplifying assumptions to obtain a two-dimensional (2D) model. However, with computer power increasing in recent years, more complex three-dimensional (3D) models have been developed and solved with fewer assumptions. Mahdi and Liangchi (1995) used FE to predict phase transformation in the workpiece assuming, surface grinding as a 2D process with a triangular heat source profile. In other study, Mamalis et al. (2003a) used a similar model with a rectangular heat flux function to investigate effect of different grinding wheels on maximum surface temperature in the workpiece. Jin and Stephenson (2004) studied transient heat transfer for high efficiency deep grinding with 3D model, evaluating effect of convective cooling on the side walls of workpiece in contact temperature. Mao et al. (2010)

performed a 3D thermal simulation proposing a parabolic distribution for heat flux in the contact zone rather than a triangular one. Mohamed et al. (2012b) showed the importance of using the accurate grinding power for calculating the heat flux in a numerical simulation of heat transfer in grinding process. The authors used instantaneous grinding power, average grinding power and calculated power from tangential force and cutting speed to obtain the contact temperature and compared it with experimentally measured temperatures. It is found that in steady-state condition instantaneous power and calculated power give the best match results with experiments where average power underestimates the temperatures. Although many thermal models for conventional grinding exist in the literature, less attention has been paid to grinding processes more recently performed by flexible robots.

2.3 Energy partition background

Energy partition is defined as the ratio of the energy that enters the workpiece to the total energy consumed by the grinding process. The energy partition largely depends on operating parameters, as well as on grinding wheel and workpiece thermal properties. Numerous studies have been conducted to determine the energy partition to the workpiece under various grinding conditions for conventional machines. A number of researchers commonly used a temperature-matching method to investigate this ratio. Using this method, the energy partition is found by matching temperatures measured during the process with the results of a thermal model or experiments. Kohli et al. (1995) found a ratio of 60-85% for conventional aluminum oxide wheels and 20% for resin bond cubic boron nitride (CBN) wheels in regular grinding. In a similar study, Guo and Malkin (1999) obtained same results with the extension that, energy partition ratio is reduced to 5-8% for vitrified CBN wheels. Guo et al. (1999) also verified that only 4.0-8.5% of total energy enters into workpiece for grinding with vitrified CBN wheels. Such a low ratio is attributed to the high thermal conductivity of the CBN grains and the enhanced fluid flow in vitrified wheels. Anderson et al. (2008c) determined the ratio of 70-90% for dry grinding with an aluminum oxide grinding wheels. Chen and Xu (2010) also performed temperature matching technique for high speed grinding and found a range of 30-75% under different grinding conditions with a brazed diamond

wheel. (Mohamed et al., 2011) found a relation between surface roughness of the finished workpiece and grain radius of the wheel in the contact zone. The authors used this correlation to update an existing energy partition model which needs estimation of grain radius. (Hadad et al., 2012) also reported a study of energy partition of grinding in dry, minimum quantity lubrication (MQL) and fluid environments for a hardened 100Cr6 steel workpiece. The authors found a 82%, 75% and 36% ratios for grinding with aluminum oxide wheel in dry, MQL and fluid cooling respectively. Whereas these ratios are reduced to 52%, 46% and 14% for CBN wheel due to high thermal conductivity of CBN abrasive.

Some investigations are conducted to relate the energy partition to relevant grinding parameters, such as process specific energy or workpiece and grinding wheel material properties. Material removal in grinding is performed by the action of many grains and can be divided into three stages—sliding, plowing and chip formation—as proposed by Hahn (1962). Consequently, grinding specific energy (u) can be divided into three fractions based on the stages above:

$$u = u_{ch} + u_{pl} + u_{sl} \quad (2.1)$$

Malkin and Anderson (1973) found that in dry shallow conventional grinding about 55% of chip formation energy and almost all sliding and plowing energy enter the workpiece. Therefore, the energy partition can be rewritten in the form of specific energy (Malkin S., 2008),

$$\varepsilon = \frac{\text{energy entering the workpiece}}{\text{total consumed energy}} = \frac{u_{pl} + u_{sl} + 0.55u_{ch}}{u} = \frac{u - 0.45u_{ch}}{u} \quad (2.2)$$

where u is the specific energy and u_{ch} is the chip formation specific energy found to be $13.8 J/mm^3$ for grinding of steel workpieces (Kohli et al., 1995). This model is applicable to grinding processes with aluminum oxide wheels and it is not true for the case that a CBN

grinding wheel is used. It is because of high thermal conductivity of CBN ($500\sim 1300 \text{ Wm}^{-1}\text{K}^{-1}$) compared to aluminum oxide ($36 \text{ Wm}^{-1}\text{K}^{-1}$) which causes significant conduction of heat into the wear flat grain at the wheel-workpiece interface in the former case (Lavine et al., 1989). Therefore, although the assumption of remaining plowing energy in the workpiece still stands, not all the sliding energy is conducted in the workpiece when grinding with CBN wheels.

All studies on the temperature and energy partition were for conventional grinding processes with rigid structures, none for specific flexible robotic grinding process. In this study, a 3D transient thermal FE code is developed to account for heat generation due to a robotic grinding operation. The aim is to study thermal conditions during the discontinuous material removal, called “vibro-impact cutting”, which is the way a flexible robot performs grinding and should be distinguished from chatter in conventional machining. First, the energy partition ratio is obtained, using the proper input heat function, through several full-size workpiece simulations and comparison with test results. The predicted energy partition value is correlated with the power model implemented in the robot controller, which has been verified in several field trials (Hazel et al., 2012a). Then, on a smaller model for the contact zone, the input heat function is adjusted to the dynamic cutting conditions based on the observed impact-cutting behavior of the robot during the grinding process to find the exact contact temperature. Knowledge of the temperature distribution is important not only for studying workpiece burns and other thermal damage, but also for the ongoing study of chip formation to predict how thermal softening affects workpiece material behavior.

2.4 SCOMPI robot

This study concerns thermal aspects of a traverse surface grinding performed by a light flexible robotic tool holder. The robot, named “SCOMPI” (Super COMPact robot Ireq), is developed by IREQ, Hydro-Quebec’s research institute, and has been used mainly for in situ maintenance of hydro turbine runners (Hazel et al., 2012b). SCOMPI is a portable, multi-purpose, track-based 6-degree of freedom robot manipulator weighing 33 kg. The robot is

capable of performing in situ plasma gouging, welding, grinding and hammer peening. It has been in use for 20 years and has proven to be an efficient, cost-effective tool for hydropower jobs. Figure 2-1a shows SCOMPI performing in situ grinding on the surface of a turbine runner blade at Manic-3 power station, in Manicouagan region of Quebec, which is operated by Hydro-Quebec.

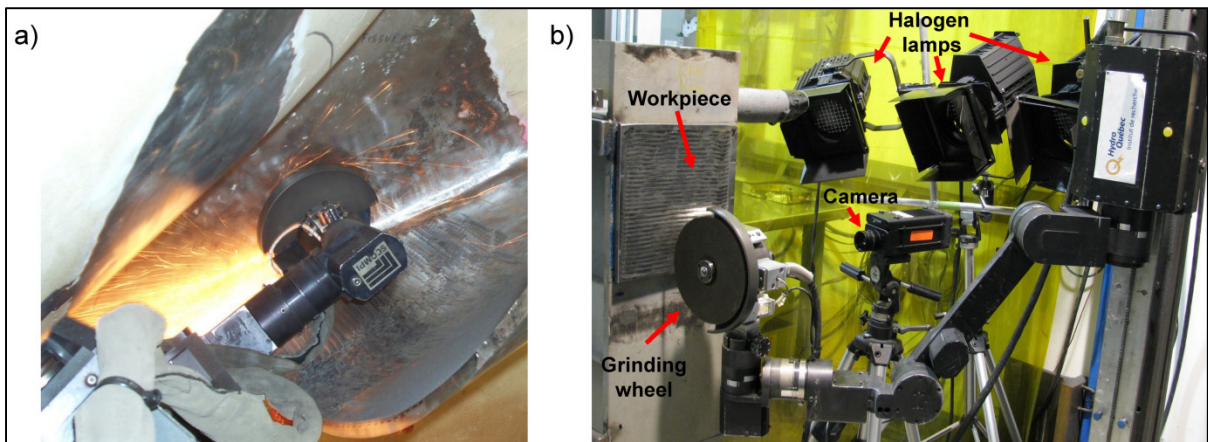


Figure 2-1 a) SCOMPI robot performing grinding operation during on-site blade modification to improve efficiency b) Laboratory setup with high-speed camera and lighting system

A high-speed digital camera and three 750-W halogen lamps providing enough light on the cut section were used to capture videos at up to 25,000 fps during the grinding process in laboratory (Figure 2-1b). Careful review of the videos revealed that under steady-state conditions, there is only one impact per turn and the wheel remains above the workpiece surface during the rest of each revolution. This vibro-impact cutting behavior is due to the low rigidity of the robot structure versus the high rigidity of the cutting process. Raffieian et al. (2013) also verified this impact cutting behavior by the measurement of instantaneous angular speed and vibrations. Note that since this grinding process is a type of high removal rate machining, no truing of the grinding wheel is performed before or during the process. Though a fine surface finish and accurate dimensions are critical for turbine blades, accuracy is maintained by controlling the material removal rate during the process, as explained in the following section.

Grinding with SCOMPI is done using grinding wheels for hand grinders, which are self-sharpening wheels. The normal force and feed speed during grinding must be kept in a range that prevents the wheel from becoming glazed or breaking. Either dull grains break to form new edges or the resin breaks exposing new grains to the workpiece. Grinding at a high removal rate with a resin bond wheel generally makes dressing unnecessary since the wheel is self-sharpening.

2.4.1 Permanent magnets grinder

The desired workpiece surface profile in conventional grinding is obtained by controlling the exact position of a well-trued, balanced grinding wheel. The grinder's very stiff structure combined with the low material removal rate (MRR) ensures the accuracy of final profile. This conventional method is not applicable to the flexible grinding process in this study where both a high MRR and precision are desired. Due to the low rigidity of the tool holder, the exact position of the grinding wheel's outer face relative to the surface profile cannot be ensured. A hybrid force/position controller is thus employed to grind at a controlled material removal rate (CMRR) by regulating the mechanical grinding power of grinder. The rotational speed must then be controlled and the mechanical power delivered at the spindle accurately monitored, considering all the effects of motor losses and temperature on motor power. To implement CMRR with a compact, lightweight tool for work in hard-to-reach areas, a custom electrical grinder was built for SCOMPI. Industrial pneumatic or electrical grinders available on the market do not perform at the level required for target applications. More details on the controller and the robot can be found in Hazel et al. (2012b).

2.4.2 Motor losses

The grinder is built around an electrical three-phase synchronous permanent-magnet motor often referred to as a "DC brushless servo motor". This type of motor was selected for its high power density and the very linear relationship between its torque and current ($Q = K_T I$), where I is the current, Q the torque and K_T the torque constant. However, part of the torque is

lost in drag and friction in the bearings, another part drives the fan and a last part is dissipated as core losses into the stator iron armature. The Joule losses and the armature reaction losses are compensated by the motor's power electronic as an increase in the voltage and do not affect the torque or measured current. In order to properly evaluate the mechanical power P_M available at the spindle, all the losses must be subtracted.

$$P_M = K_T I \omega - P_{Drag} - P_{Fan} - P_{Core} \quad (2.3)$$

The bearing friction torque is assumed constant and bearing losses proportional to the speed ($P_{Drag} \propto \omega$). From dimensional analysis, fan losses are found to be proportional to the cube of rotational speed ($P_{Fan} \propto \omega^3$). As the rotor is rotated, core losses arise from the variation of magnetic flux density into the stator laminations. This variation incurs Eddy current losses as well as hysteresis losses into the core. These losses are offset by supplying additional current. These core losses increase exponentially with the rotational speed and can be estimated with the Steinmetz equation (James R. Hendershot and Miller, 1994),

$$P_{Core} = k_{hys} B^{1.5} f + k_{eddy} B^2 f^2 \quad (2.4)$$

where k_{hys} is the hysteresis loss coefficient, k_{eddy} is the Eddy loss coefficient, B is the flux density and $f = p \frac{\omega}{2\pi}$ is the frequency with p being the number of pole pairs.

2.4.3 Influence of temperature

A rise in temperature adversely affects the motor in two ways. The resistivity of the copper increases and the flux density of the rotor magnets decreases, both linearly with temperature. Therefore, copper losses and the performance loss of rotor permanent magnets are considered in the model. Since the value of torque constant K_T is also a function of the remanent flux density, the torque constant at a given temperature T is given by:

$$K_{T(T)} = K_{T(T_{ref})} (1 + \alpha_T (T - T_{ref})) \quad (2.5)$$

where α_T is a negative reversible temperature coefficient and $K_{T(T_{ref})}$ is the value of the torque constant at reference temperature T_{ref} . As the magnets heat up, more current is thus required in the stator to produce torque. In turn, this current increase contributes to more copper loss and the temperature rises. The temperature must be limited to about 100°C to avoid demagnetizing the rotor permanent magnets. Note however, that core losses decrease as the temperature rises.

2.4.4 Motor parameter measurements

The permanent-magnet electrical grinder used in this study is a 2,500-W model with an operating rotational speed of 5,000 to 8,000 rpm. In order to obtain an accurate estimate of the mechanical power delivered at the spindle, the grinder is tested on a dynamometer bench at IREQ lab prior to be used for the experiments. The dynamometer bench is comprised of a Magtrol HD-805 hysteresis dynamometer and a DSP-6001 dynamometer controller, to obtain its torque model parameters. A series of steady-state measurements is taken at various speeds and power levels, then motor parameters K_T , α , k_{hys} and k_{eddy} are optimized through regression analysis. Figure 2-2a shows the graph for torque constant versus winding temperature and Figure 2-2b summarizes the motor losses at different rotational speeds. Typically, the mechanical power estimation error is less than 2% for the entire range of attainable power levels, speeds and temperatures.

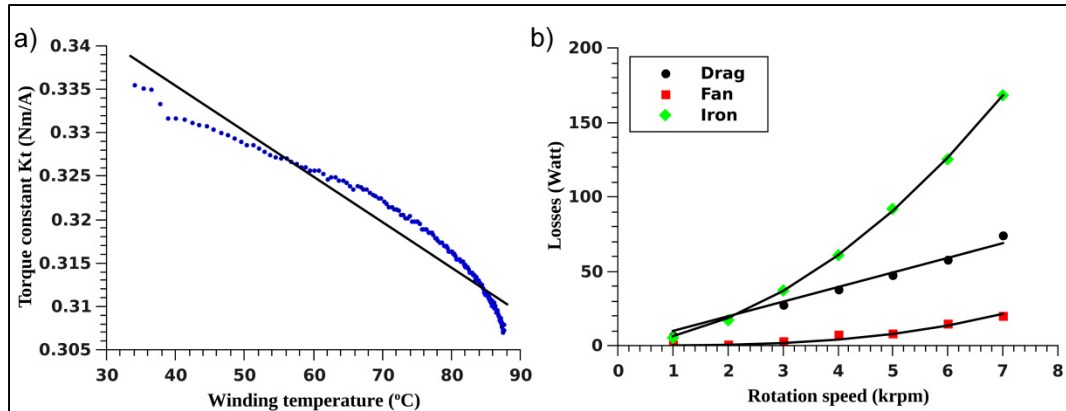


Figure 2-2 a) Grinder motor torque constant, $N=6000$ rpm, $\alpha=-0.1535$ %/°C, b) Grinder motor losses

2.5 Modeling technique

Most finite element models of the grinding process consist of a meshed workpiece with all other effects applied as heat sources or heat dissipations. Among the boundary conditions, effects of grinding wheel contact area and heat input are the most important factors to consider. It is thus crucial to have a good understanding of the geometry of the cut and removed chips, based on the type and characteristics of the grinding process.

2.5.1 Kinematic model

Figure 2-3a shows a cylindrical grinding wheel, considered to be held by SCOMPI robot, performing a single pass of traverse surface grinding. The distance that the wheel advances in the feed direction during the time of one revolution Δx is equal to V_f/N , in which V_f is the feed speed and N is the number of rotations of the wheel per second. As the steady-state condition is reached, the rate of radial wear of the wheel becomes constant. A specific amount of material is then removed at each impact, i.e., at each revolution of the wheel. Figure 2-3b is a schematic view of the central section of the wheel at time t_0 and after one revolution at time $t_0 + \Delta t$. The material removed during this advancement of the wheel, the hatched area in the cross-sectional view, is called the “uncut chip”.

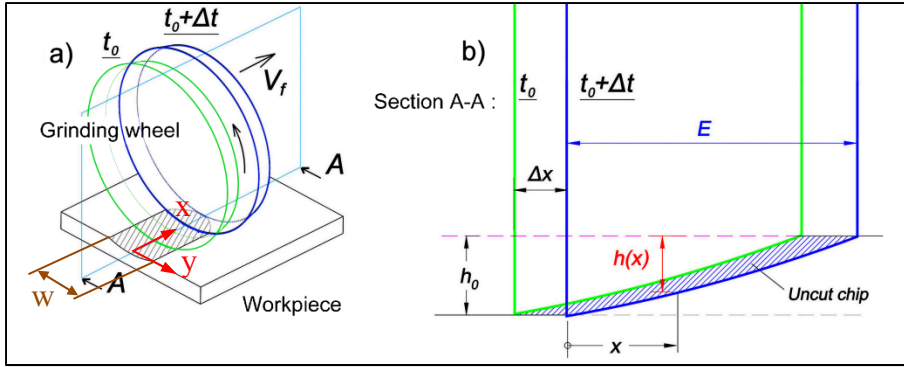


Figure 2-3 Kinematics of cut

A geometrical model for the depth of cut through the thickness of the wheel based on the shape of the wheel in steady-state condition was developed by (Hazel et al., 2012b). It is assumed that an imaginary blade, as the cutting tool, comes into contact with the workpiece at each impact and removes the chip. In the model, the depth of cut (h), which is actually the profile of the wheel under steady-state conditions, can be calculated based on the maximum depth of cut (h_0), wheel thickness (E) and position along the wheel thickness (x). Maximum depth of cut (h_0) can also be obtained from material removal rate (Z_w), feed speed (v_f) and wheel radius (R). Then, width of cut (w), which is necessary for determining the contact area, is obtained from the parameters above and maximum wheel radius (R_0) by the following geometrical equations as described in details in (Hazel et al., 2012b),

$$h(x) = h_0 \left(1 - \frac{x}{E}\right)^{\frac{2}{3}} \quad \text{where} \quad h_0 = \left[\frac{3Z_w}{4v_f} \sqrt{2R} \right]^{\frac{2}{3}} \quad (2.6)$$

$$w(x) = 2\sqrt{R_0^2 - (R_0 - h(x))^2} \approx 2\sqrt{2R_0 h(x)}$$

Then, local uncut chip thickness (δ) through the wheel thickness can be calculated as follows,

$$\delta(x) = \begin{cases} h(x) - h(x + \Delta x) & 0 \leq x < E - \Delta x \\ h(x) & E - \Delta x \leq x \leq E \end{cases} \quad (2.7)$$

Substituting $h(x)$ and $h(x+\Delta x)$ from Equation (2.6) and considering that $\Delta x=V_f/N$ and finally using Maclaurin series we can rewrite Equation (2.7) as below,

$$\delta(x) = \begin{cases} \delta_0 \left(1 - \frac{x}{E}\right)^{-1/3} & 0 \leq x < E - \Delta x \\ h_0 \left(1 - \frac{x}{E}\right)^{\frac{2}{3}} & E - \Delta x \leq x \leq E \end{cases} \quad \text{where, } \delta_0 = \frac{1}{EN} \left(\frac{Z_w^2 v_f}{12R} \right)^{1/3} \quad (2.8)$$

In this kinematic model, the cutting behavior is represented in a way similar to milling. A mechanical model by Altintas and Lee (1998) is thus used to obtain the instantaneous cutting force (F_T),

$$F_T(x) = \gamma(k_e + k_c \delta(x)) \quad (2.9)$$

where k_e is the edge force coefficient representing the force to overcome friction, k_c is the shear cutting coefficient representing the force to deform the chip and γ is the abrasive grit width. The average force is then calculated as below which is multiplied by peripheral speed ($V_s=2\pi RN$) to predict the power of process (P) (details can be found in (Hazel et al., 2012b)),

$$\bar{F}_T = \frac{1}{2\pi R} (k_e S + k_c \frac{Z_w}{N}) \quad (2.10)$$

$$P_M = P_{friction} + P_{chip} = k_e S N + k_c Z_w \quad (2.11)$$

where S is the area of contact surface and Z_w is the volumetric material removal rate. Parameters k_e and k_c must be determined experimentally for each combination of wheel and workpiece. The first term on the right-hand side of Equation (2.11) represents the power consumed to overcome friction ($P_{friction}$) and the second term is the power consumed for chip formation (P_{chip}).

Before and after each test, the workpiece plate was weighed and the material removal rate calculated based on the grinding time. Then, the edge force coefficient (k_e) and the shear cutting coefficient (k_c) were obtained using the nonlinear least-squares optimization method. The objective function was set to fit the predicted power (from the model in Equation (2.11)) and measured power through a series of test with different grinding parameters. The coefficients were identified as $k_e=177 \text{ N/mm}$ and $k_c=6787 \text{ N/mm}^2$ for the workpiece material and grinding wheel used for the experiments.

2.5.2 Heat input function

As stated earlier, two factors must be considered in defining the heat input for a thermal FE model of the grinding process: the contact area between grinding wheel and workpiece, and the heat input function. For several thermal simulations of conventional grinding found in the literature, contact area is established assuming continuous contact of the grinding wheel and workpiece. This contact is usually approximated as a line in 2D models or as a rectangular interface in 3D models (Lin et al., 2009) with a uniform (Mamalis et al., 2003b) or triangular heat input distribution (Brosse et al., 2008). Furthermore, heat flux (q) has been defined on a flat plane for shallow grinding, ignoring the small depth of cut; whereas, in creep-feed grinding simulations, an inclined plane is usually considered as the contact surface given the higher depth of cut (See Figure 2-4) (Anderson et al., 2008a).

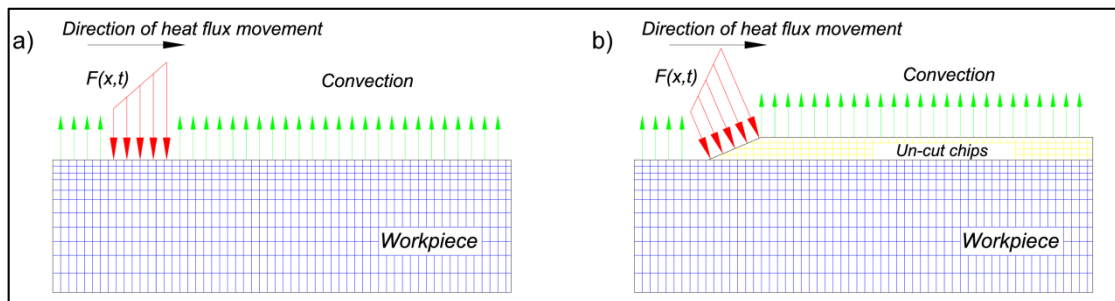


Figure 2-4 Heat input model for a) shallow grinding, b) creep-feed grinding, (Anderson et al., 2008a)

Heat generation at the wheel-workpiece interface can be attributed to the plastic work done to deform the chip, as well as to friction between the grits and workpiece surface. As explained

in the previous section, both of these are considered in the force model by k_e and k_c coefficients. The generated energy per unit area, hereafter called energy intensity function (J/mm^2), can be stated from the right-hand term of Equation (2.9),

$$e_d(x, y) = k_e + k_c \delta(x) \quad (2.12)$$

Considering that all the energy is converted in to heat and substituting the local un-cut chip thickness from Equation (2.8), we can derive the function for generated heat intensity as below,

$$e_d(x, y) = \begin{cases} k_e + k_c \delta_0 \left(1 - \frac{x}{E}\right)^{-1/3} & 0 \leq x < E - \Delta x \quad \text{where } \delta_0 = \frac{1}{EN} \left(\frac{Z_w^2 v_f}{12R} \right)^{1/3} \\ k_e + k_c h_0 \left(1 - \frac{x}{E}\right)^{2/3} & E - \Delta x \leq x \leq E \quad \text{where } h_0 = [3Z_w / (4v_f \sqrt{2R})]^{2/3} \end{cases} \quad (2.13)$$

The function for heat input distribution is then obtained by adding the energy partition ratio (ε),

$$H(x, y) = \varepsilon e_d(x, y) \quad (2.14)$$

$H(x, y)$ is used as the heat input in FE code at each time step which is selected as the impact time in the process. Multiplying Equation (2.13) by the number of the rotation of the wheel per second (N) gives the average power intensity which can be used as the generated heat flux distribution. An example of heat input distribution and chip thickness over the contact area is shown in Figure 2-5. The grinding wheel's outer radius was measured before each set of tests to update the calculation of the width of cut (Equation (2.6)) for contact zone and heat input distribution (Equation (2.13)), assuming that $R \approx R_0$ since $h(x) \ll R(x)$.

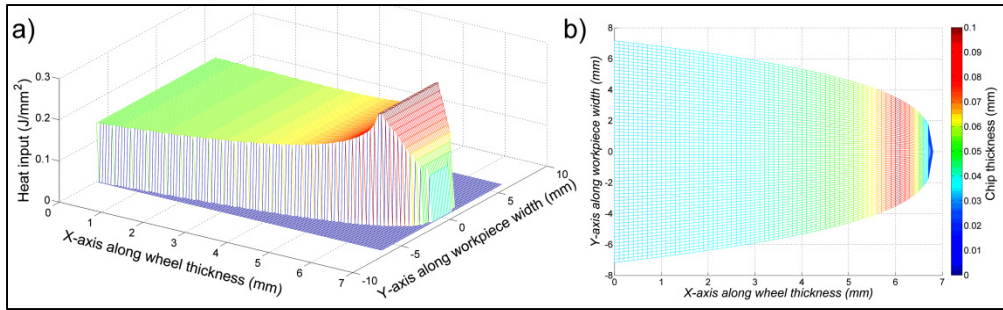


Figure 2-5 a) Heat input distribution, b) Uncut chip thickness over the wheel-workpiece interface

A second consideration in the heat input function for this study is the dynamic effect of impact-cutting behavior. The heat function obtained in Equation (2.14) is the average heat input into the workpiece. This function gives acceptable results for the temperature of points that are not very close to the surface being ground. For contact temperature in the cutting zone, however, this function ignores the dynamic effect of vibro-impact cutting. The input function was thus modified to represent more realistically impact-cutting conditions observed. A time variable is added to the heat input function $H(x,y)$ with an impacting function. Although the total heat input is the same, in the modified function, heat of higher intensity is applied in a very short lapse of time, the duration of the impact. The model then applies no heat input for the rest of revolution of the wheel when there is no contact. Figure 2-6 shows the impact heat input scheme through the simulation time steps.

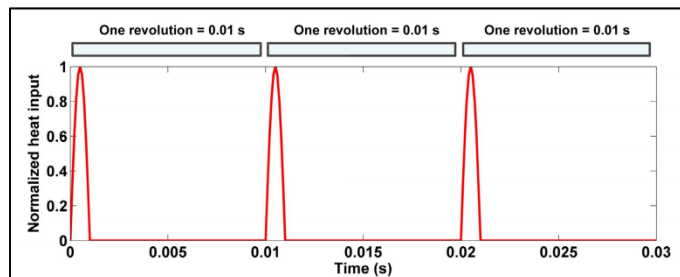


Figure 2-6 Impact heat input scheme

The frequency of impact is 100 Hz, derived from the rotational speed of the grinding wheel. The time step length of each phase in the simulations was obtained from the kinematic model of the cut.

2.5.3 Finite element formulation

Finite element simulations were carried out using an FE code developed in C++ at IREQ, Hydro-Quebec's research institute. This open source code was customized to fit the needs of this study. Several factors motivated the decision to use open source code rather than commercial FE software. First, the code could be modified to support the process characteristics required for this specific study. Second, the code could be adapted to any new hardware platform and implemented in future systems, if needed. Third, the code, enhanced with a faster solver using general-purpose computing on graphics processing units (GPGPU), made the simulation up to 20 times faster than commercial software.

The FE code was developed for solving transient thermal problems based on the following energy equation (Robert D. Cook, 2007),

$$\Pi = \int \left(\frac{1}{2} \{T_{\partial}\}' [k] \{T_{\partial}\} - QT + c\rho T\dot{T} \right) dV - \int (f_B T + h T_{fl} T - \frac{1}{2} h T^2) dS \quad (2.15)$$

where T and $\{T_{\partial}\}$ are the temperature and its gradient matrix, $[k]$ is the thermal conductivity matrix, c is the specific heat, ρ is the mass density, Q and f are internal heat generation and heat flux, and h and T_{fl} are the convection heat transfer coefficient and adjacent fluid temperature. Considering the principle of stationary potential energy and rewriting Equation (2.15) in matrix form results in,

$$[C] \{\dot{T}\} + ([K] + [H]) \{T\} = \{R_h\} + \{R_Q\} \quad (2.16)$$

where C is the specific heat matrix, K and H are conductivity and boundary convection matrices, and R_h and R_Q are boundary convection and heat generation vectors respectively. Numerical integration using a multidimensional Gauss quadrature rule is used to form Equation (2.16) for each element. The resulting equations are then assembled for the entire

model to obtain the FE equations of the whole system. Finally, GPU parallel processing is used to solve these FE equations and find the nodal temperature at each step of the simulation.

2.5.4 Finite element model

Two models were used for the simulations in this study. The first one was a full-size workpiece model ($300 \times 150 \times 12$ mm) containing 270,000 hexahedral eight-node elements. This model was used to evaluate the energy partition ratio to the workpiece. The second model was a symmetric model of the cutting zone ($20 \times 10 \times 4$ mm) containing 28,800 hexahedral elements for simulation of the contact temperature. As heat input distribution has a ZX plane of symmetry (see Figure 2-5), only one half of the cutting zone model was considered for thermal analyses relative to the symmetry plane. A workpiece length of 20 mm was found by trial and error to result in a steady maximum temperature in the contact zone. In both models, the mesh is denser toward the surface being ground in order to have accurate results close to the contact zone, and a mesh convergence study was performed to determine how fine a mesh was necessary to obtain accurate results. Heat generation (q) according to the function explained in Section 2.5.2 is applied in a thin layer of mesh representing the cutting zone. Elements there are removed from the model after the heat source has passed over them to account for the material removed in the form of chips during the process.

The heat source is moved through simulations over the workpiece surface following the grinding grooves performed in the experiments. For each set of tests, the thickness of the plate in the model was adjusted based on the actual measured thickness. Temperature-dependent material properties used in the simulations were for stainless steel 304L, the material of test workpieces (see Table 2.1).

Table 2.1 Temperature-dependent material properties for stainless steel 304L

Temperature (°C)	20	200	400	600	800	1000	1200	Units
Conductivity	16.2	18.2	21.3	23.5	26.8	28.1	30	W/(m·K)
Specific heat	460	515	548	580	611	618	625	J/kg-K
Emissivity		0.13	0.16	0.17	0.19	0.21	0.4	

2.6 Experiments

The experimental setup is illustrated in Figure 2-7a. The tests were conducted using the six degree-of-freedom SCOMPI robot with a cylindrical Type 27 NORZON III grinding wheel (Zirconia Alumina abrasive). Grinding parameters used during the experiments are selected based on the most appropriate robot working condition during the grinding process. The cylindrical grinding wheels were 6.8 mm thick and 230 mm in diameter. The rotational speed of the grinding wheel was kept constant at 6,000 rpm and a series of tests were conducted with grinder power set to 1,000, 1,250, 1,500, 1,750 and 2,000 W, and feed speeds of 40, 60 and 80 mm/s, leading to a maximum depth of cut ranging from 0.1 to 0.35 mm.

Embedded thermocouples were used to measure both the highly transient temperatures close to the contact area and subsurface temperatures. K-type thermocouples, composed of a single strand of Chromel and Alumel wires, were found to be the most suitable for the study. With diameters of 0.01 and 0.003 inch, such thermocouples can measure a wide temperature range (0°C to 1,250°C) with an acceptable response time and good accuracy.

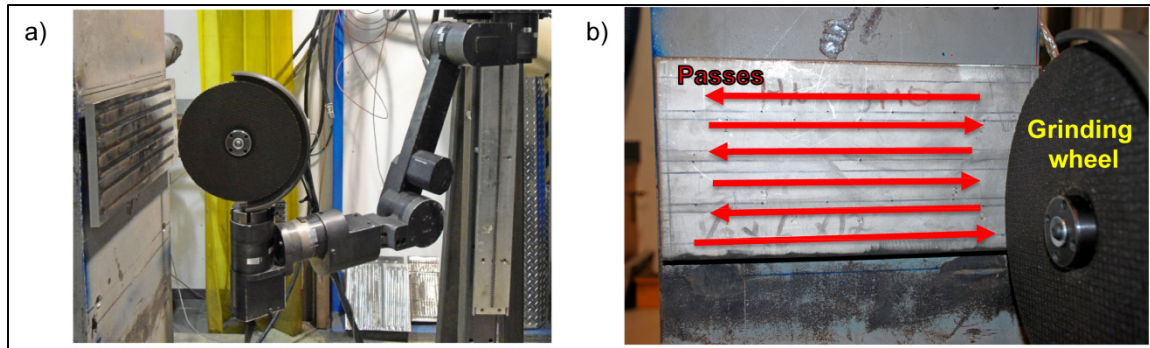


Figure 2-7 a) SCOMPI robot experimental setup, b) Grinding trajectories (one layer of material removal)

Some thermocouples were spot-welded to the back of workpiece plates, others electro-discharge-welded at the bottom of blind holes of different depths from the back of the plates. Ceramic insulators were installed inside the holes to make sure that temperature readings were really at the tip of the thermocouples. An ultra-high-temperature epoxy (Pyro-Putty 2400) was also used to hold the thermocouples in position after installation and during the grinding process. Grinding was continued until all the material above the thermocouples was removed and they were exposed to cutting (see Figure 2-8). The last maximum temperature before losing the output signal due to the thermocouple breaking is taken as the maximum temperature in the contact zone during the grinding process.

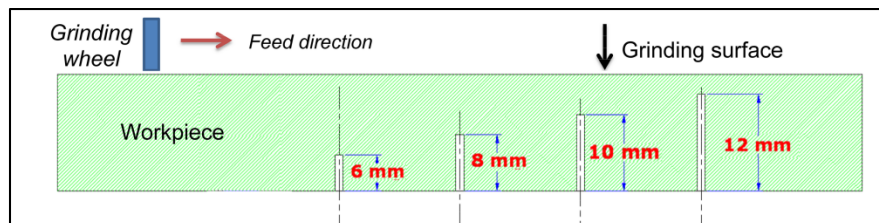


Figure 2-8 Position of subsurface thermocouples

Several stainless steel plates ($300 \times 150 \times 12$ mm) were used as the workpiece. The grinding passes were performed along the 300 mm length of the plate with 6 mm in feed distance. The robot thus required 23 passes to grind the whole surface of the plate once, which is referred as “one layer” in this study (Figure 2-7b). Mechanical power at the grinder’s spindle was also

calculated based on the measured current and temperature of the grinder, explained in details in section 3. This power is used to obtain the total energy converted into heat in the process.

2.7 Results and discussion

2.7.1 Energy partition results

The full-size workpiece FE model and corresponding temperature measurements were used to obtain the energy partition ratio by a temperature-matching technique. Apparently, the temperature at nodes close to the contact area is very sensitive to the heat input function. Several preliminary simulations were performed with different heat input distributions which had equal total energy. The purpose was to find the necessary distance below the contact zone where node's temperature is not affected by the shape of heat input distribution. This sensitivity analyses showed that if a check point for recording the temperature is chosen far enough away from the contact zone (3 mm or more), the amount of energy entering the workpiece is analyzed rather than heat input distribution shape. For each set of experiments, two or three layers were ground and temperatures at different depths and at the back of the plate were read from the thermocouples. The results were compared to the simulated temperature of the nodes at the same location to find the proper energy partition ratio. Figure 2-9a shows the temperature distribution in the middle of the process obtained by the FE code and Figure 2-9b shows the test rig.

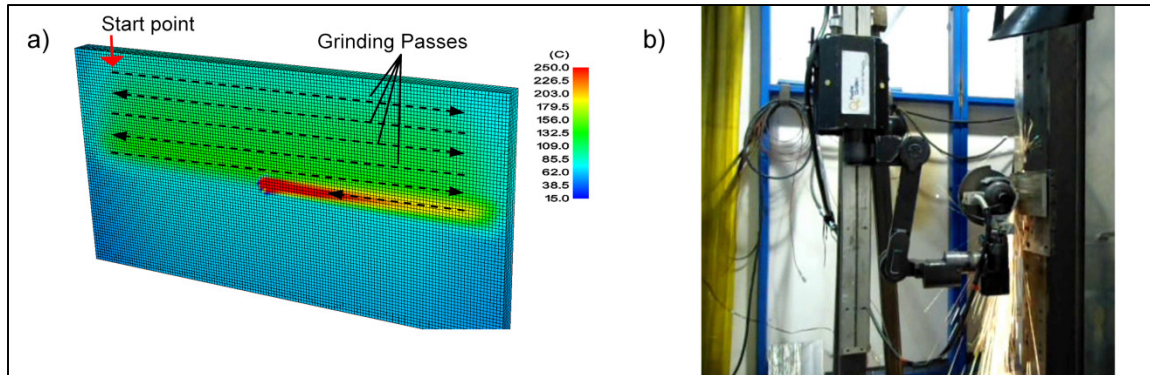


Figure 2-9 a) Full-size workpiece FE simulation, b) Test rig for determining the energy partition ratio

Figure 2-10 illustrates the temperature-matching technique for two sets of grinding parameters. Thick blue lines are the temperatures measured by the thermocouples and the other lines are the simulated temperatures of nodes at the same positions. Simulations are repeated for different energy partition ratios until the match with lowest RMS error is found for the specific grinding condition.

Figure 2-10a shows the results for two continuous layers of grinding at a power of 1,500 W and feed speed of 60 mm/s. In this set of test results, the thermocouple is 5 mm below the grinding surface. At each layer as grinding progresses, an increase in temperature is observed, as expected, in both simulated and experimental results. The peak temperature occurs when the moving heat source or grinding wheel is directly above the monitored node in the FE model or above the thermocouple in the experiment. It can be easily seen that applying all the energy ($\epsilon = 100\%$) as heat input to the model overestimates the results. Fig. 10b is the magnification of the area in the dotted rectangle from Figure 2-10a. In this case, an energy partition of 51% is found to be a good match with the experimental measurements (RMSD = 6.52). This matching technique is repeated for up to four thermocouples for each set of grinding parameters to obtain the average value for the energy partition under that grinding condition.

Figure 2-10c and Figure 2-10d illustrate another matching for a power of 1,500 W and feed speed of 80 mm/s. The point chosen for temperature measurements in this case is 12 mm inside the workpiece below the contact zone. Therefore, a noticeably smoother increase in temperature profile at each layer is seen in comparison with the previous case. The reason is the greater distance between the measurement point and grinding surface. Although a step-like temperature increment is evident, no sharp peak due to a flash temperature in the contact zone is measured by the thermocouple or simulated for the corresponding node by the FE model. A slightly lower energy partition of 46% (RMSD = 4.34) was found with these grinding parameters.

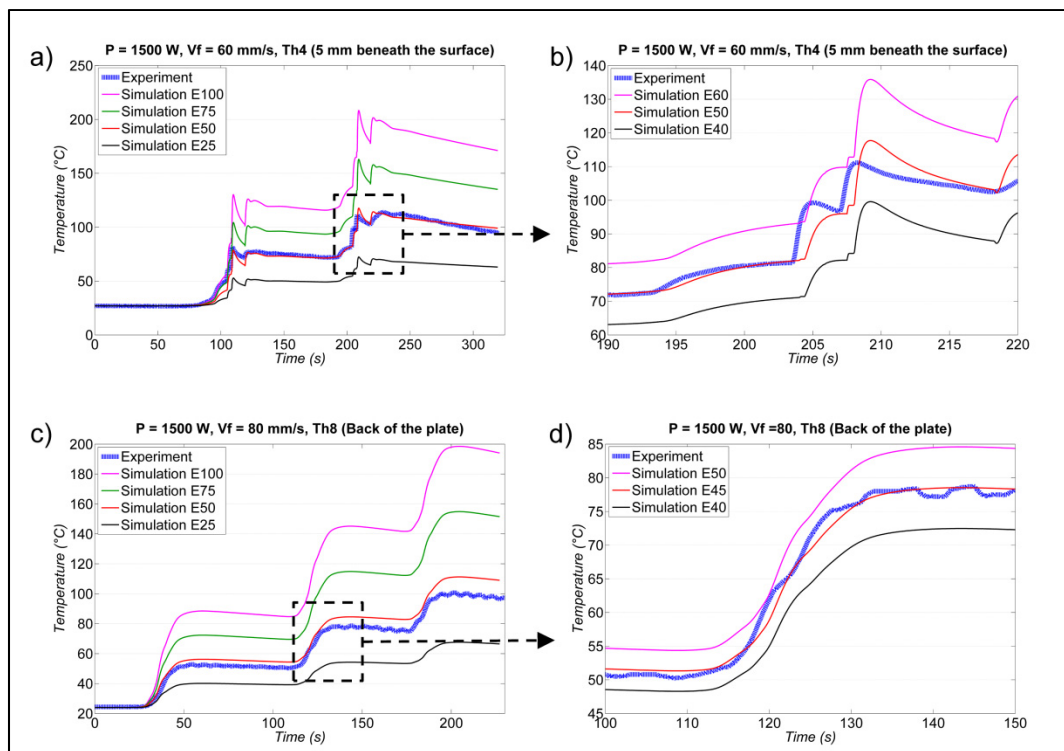


Figure 2-10 Temperature-matching technique for finding the energy partition ratio, a, b) $P = 1,500$ W, $V_f = 60$ mm/s, depth = 5 mm; c, d) $P = 1,500$ W, $V_f = 80$ mm/s, depth = 12 mm

The final energy partition ratio results for the range of study are shown in Figure 2-11. At lower feed speeds, high power levels are avoided to stay in the feasible working range of the process. Using high power at low feed speed leads to an unsatisfactory surface finish and to

excessive wheel wear rates. Due to the problems above and to avoid too deep a cut, which is undesirable in this process, the maximum power range is reduced at lower feed speeds.

As seen from the results, the energy partition ratio decreases as power is increased. This pattern of energy partition is due to how the depth of cut varies at different power levels. As stated earlier, sliding and plowing energy are primarily stored in the workpiece and hence play a major role in determining the energy partition ratio. Furthermore, with higher depth of cut, bigger chips are formed and carry a significant portion of the heat generated away from the workpiece. Therefore, higher power that leads to a higher chip volume-to-surface ratio, lowers the ratio of sliding and plowing energy in the total consumed energy.

Based on the results obtained, the energy partition ratio also tends to increase slightly as the feed speed is lowered. This behavior can again be associated to chip thickness. Low feed speed means a smaller uncut chip thickness at each impact cut and hence more energy wasted by friction and plowing.

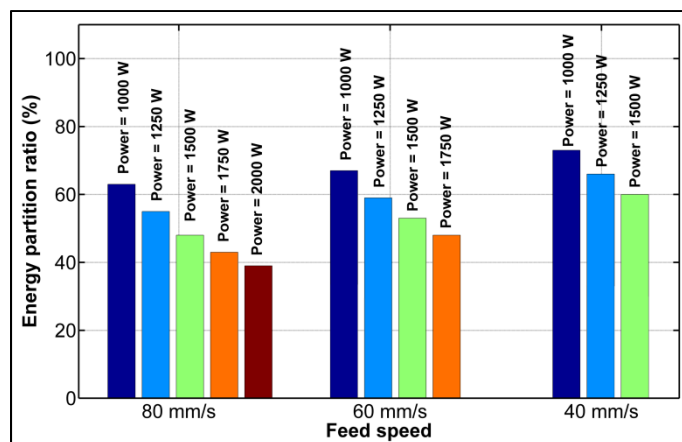


Figure 2-11 Energy partition ratio for different power levels and feed speeds

As explained in Section 2, (Malkin S., 2008,) developed an equation for energy partition during dry shallow conventional grinding with Aluminum oxide wheel. His empirical model, based on the specific energy consumed during the grinding process, is one that other studies most commonly use and refer to. However, Equation (2.2) was found to overestimate the

workpiece energy ratio for flexible robotic grinding of this study. The energy partition is lower than that in analogous conventional grinding because in the vibro-impact cutting regime of this flexible grinding process, much bigger chips are removed from the workpiece. The chip surface-to-volume ratio is thus smaller and less frictional energy, which is primarily dissipated as heat and stored in the workpiece, is produced in vibro-impacting.

Theoretical and experimental study by (Malkin and Anderson, 1973) showed that the heat transferred by sliding and plowing energies to the grinding wheel is negligible for Aluminum oxide wheels. As mentioned earlier grinding wheel in this study is the type with Zirconia Alumina abrasive, which has very small thermal conductivity ($2\sim5 \text{ Wm}^{-1}\text{K}^{-1}$) compared to Aluminum oxide (Bansal and Zhu, 2005). Therefore, almost all of the sliding heat generated at the wheel-workpiece interface will be transferred into the workpiece. Also, because plowing energy is associated with heat due to the deformation in the workpiece without material removal, it is reasonable to assume that in such high speed process, the plowing heat mostly stays in the workpiece. Hence, we make a similar assumption in our study, i.e., that most of the chip formation energy leaves with the chips whereas most of the sliding and plowing energy enters the workpiece, then the difference in the ratio is due to the percentage of chip thermal energy that stays in the workpiece. A modified version of the Malkin model is thus proposed in Equation (2.17), whereby only 40% of chip energy enters the workpiece in the flexible robotic grinding process studied. The results of the proposed equation fit well with the energy partition ratios from experiments, within 5% of relative error (Figure 2-12).

$$\varepsilon = \frac{u - 0.6u_{ch}}{u} \quad (2.17)$$

If the power model of the process (Equation (2.11)) is considered, we can write an equation for the energy partition ratio based on the percentage of each friction and chip formation parts as follows,

$$\varepsilon = \frac{\alpha P_{friction} + \beta P_{chip}}{P_M} \quad (2.18)$$

Substituting the process parameters, edge force and shear cutting coefficients we can derive an energy partition equation which can directly give the energy partition ratio based on the parameters that are already implemented and known in the control system of the process,

$$\varepsilon = \frac{\alpha k_e SN + \beta k_c Z_w}{k_e SN + k_c Z_w} \quad (2.19)$$

In an optimization process to fit the energy partition model with the experiments, α was found to be equal to 0.85 and β equal to zero. The goal on this optimization was to find fixed values of α and β for the entire range of process parameters in this study. Figure 2-12 shows the energy partition ratios from the experiments, the conventional Malkin's model, the modified Malkin's model and the power model.

It can be seen that the prediction by the power model with constant α and β has considerable error especially at lower feed speeds and low powers. This is due to neglecting the contribution of chip formation energy to the heat conducted into the workpiece which is found to be varying in different process conditions. Therefore another set of constrained optimization was carried out using a nonlinear least-squares method for variable β and constant α . It was found that $\alpha=0.76$ and β values mentioned in Table 2.2 can give best energy partition ratios in the power model.

Table 2.2 β values for the energy partition in power model

Power Feed speed	1000	1250	1500	1750	2000
40	0.49	0.33	0.2	-	-
60	0.36	0.21	0.13	0.08	-
80	0.27	0.17	0.09	0.05	0.03

The results for β show that the ratio of chip formation energy that enters the workpiece decrease when we have bigger chip thickness (i.e. higher powers or higher feed speeds). This means bigger chips carries most of the chip formation energy out of the workpiece, where small chips because of larger surface/volume ratio conduct more heat to the workpiece before they are completely separated and leave the contact zone.

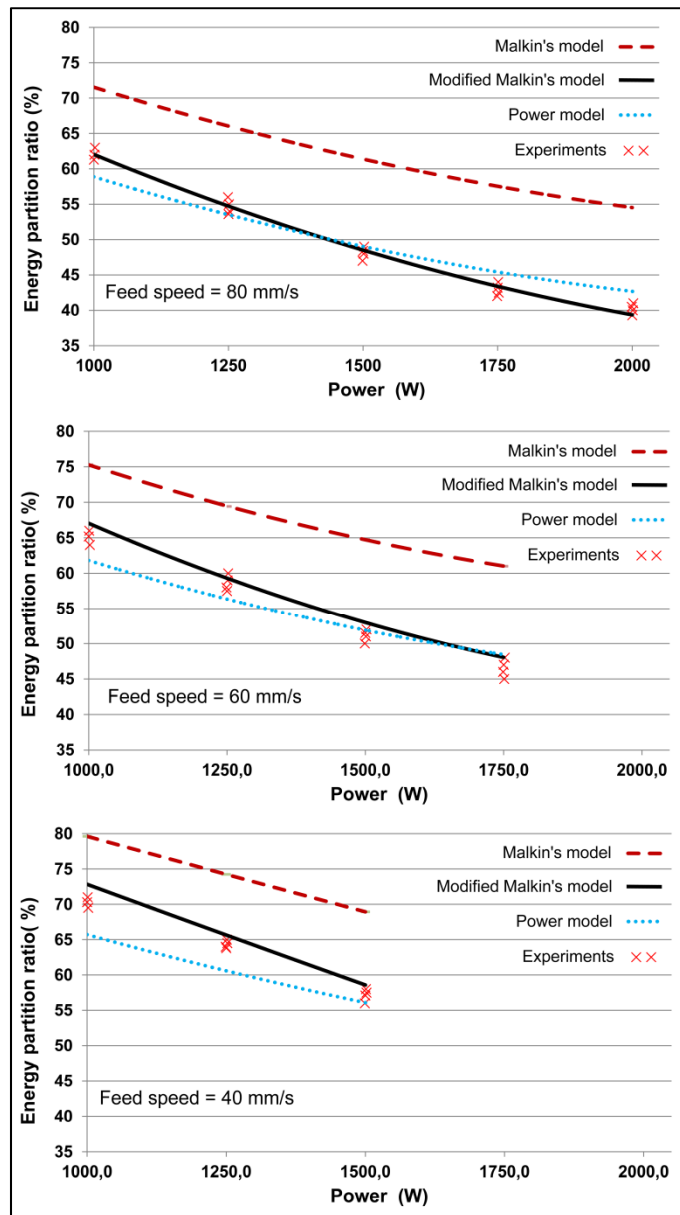


Figure 2-12 Energy partition fitting model

2.7.2 Contact temperature results

Having the correct energy partition ratio for the process, a second FE model was used to determine the precise temperature in the grinding contact zone. The high temperature gradient close to the contact zone means that a very fine mesh is needed to obtain sufficiently accurate results. Therefore, a smaller FE model with a finer mesh is chosen for simulations to capture the high transient temperature in the zone of interest. Thermocouples installed just below the surface being ground were used for experimental comparison and validation.

Figure 2-13 shows the temperatures obtained from a sample thermocouple initially 0.6 mm beneath the workpiece surface. As successive layers of material are removed, the flash temperature increases at the thermocouple. The main drawback in using thermocouples for measuring the temperature in grinding processes is the possibility of improper installation of the thermocouple tip. It is also time-consuming to install thermocouples and they can be used only once. The experiments were repeated several times to ensure reliable results.

Figure 2-14 shows temperature distribution results at the workpiece contact zone based on the heat input function described in Section 2.5.2 with a grinding power of 1,500 W and feed speed of 40 mm/s.

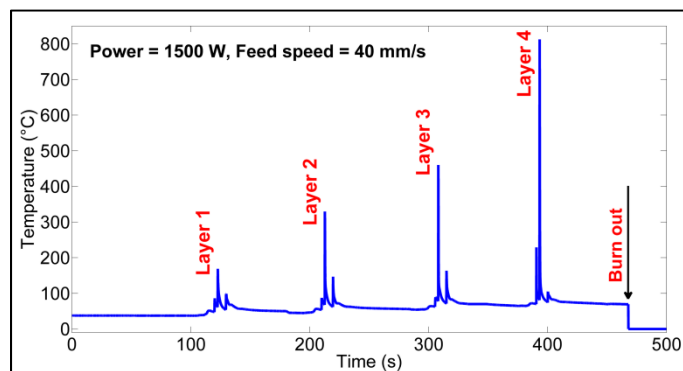


Figure 2-13 Experimental thermocouple temperature measurements during the grinding passes

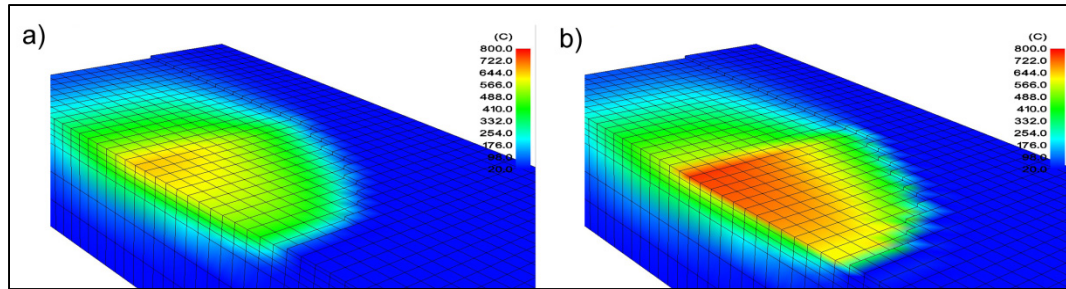


Figure 2-14 Finite element temperature distribution in the workpiece contact zone a) One step before the impact-cut, b) Impact-cut step (Power = 1,500 W, Feed speed = 40 mm/s)

Figure 2-15 summarizes results for the maximum temperature reached in the contact zone from finite element simulations (shown as lines) and from test thermocouples (shown as scattered points). Dashed lines are for simulations with average heat input, solid lines for simulations of dynamic heat input due to the vibro-impacting behavior in grinding. The total amount of heat entering the work piece at one revolution of the wheel in both cases is the same. However, in the latter, heat is applied with higher intensity only during the impact time compared to the former case where an average input is applied without interruption. Therefore, higher maximum temperatures can be seen in the impact-cutting process despite the fact that we have intermediate cooling between the impacts. The comparison shows a good match between tests results and the simulated temperatures obtained from the FE model with dynamic effects.

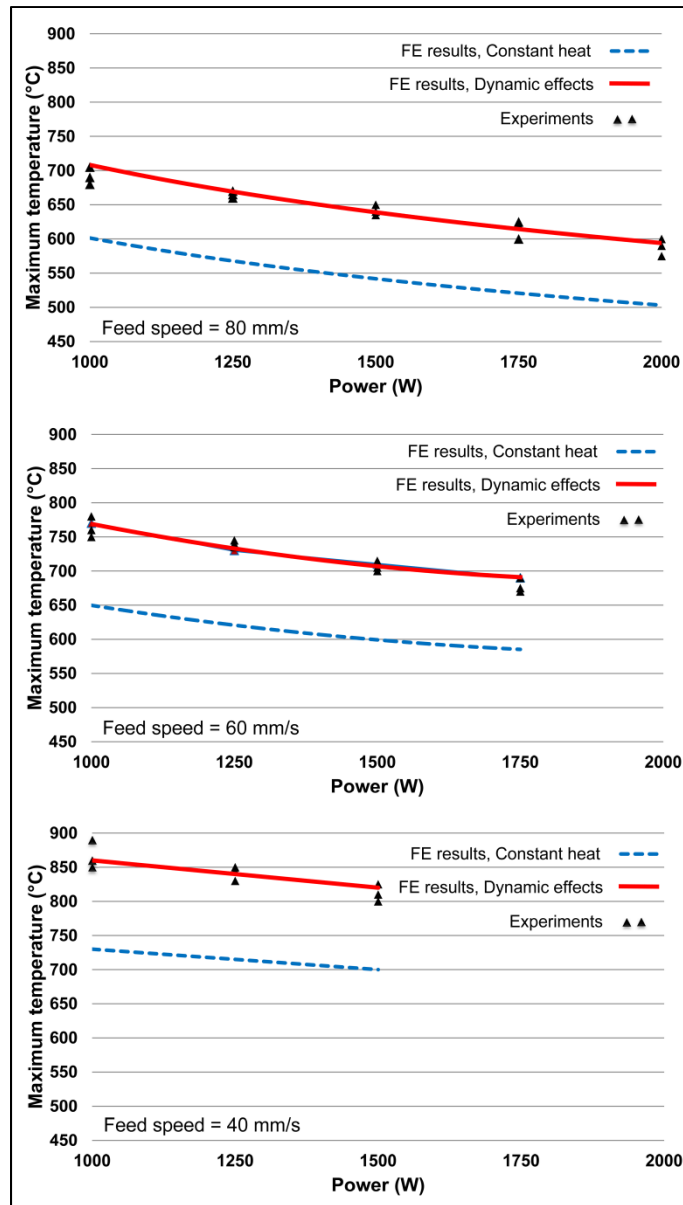


Figure 2-15 Contact temperature from finite element analyses and tests

Despite the lower energy partition ratio at higher power levels, the total amount of heat entering the workpiece increases with power. However, slightly lower temperatures were seen at higher power levels both in FE model and test results. The lower temperatures can be attributed to the lower intensity of heat input due to the larger contact area at higher power levels.

2.8 Conclusions

A new representation of the heat source in flexible robotic grinding process is proposed in this paper based on local chip thickness, friction and sequential impacting. Then, 3D finite element thermal simulations and test measurements of temperature were performed in order to adjust the energy partition ratio using a temperature-matching technique. Enhanced coding with a faster solver using general-purpose computing on graphics processing units (GPGPU), made the simulation up to 20 times faster than commercial software. The energy partition ratio was found to be lower for flexible robotic grinding than for analogous conventional precision grinding. A modified empirical model from the literature and a new formula developed from the power model of the process are proposed to determine the energy partition applicable to this study. Good agreement between the results from the models developed and test results with various grinding parameters show the validity of the models. Modifications and factors to include the dynamic effect of robotic grinding in the contact temperature model were also presented. The dynamic model predicted temperatures approximately 15% higher than when average parameters are considered. Predicted FE results showed a close match with test results.

2.9 Acknowledgements

The authors would like to thank the SCOMPI team at IREQ (Hydro-Quebec's research institute). The authors would also like to express their gratitude to the Natural Sciences and Engineering Research Council of Canada (NSERC) and to Hydro-Québec for supporting this research.

2.10 References

Altintas, Y., Lee, P., 1998. Mechanics and Dynamics of Ball End Milling. *Journal of Manufacturing Science and Engineering* 120, 684-692.

- Anderson, D., Warkentin, A., Bauer, R., 2008a. Comparison of numerically and analytically predicted contact temperatures in shallow and deep dry grinding with infrared measurements. *International Journal of Machine Tools and Manufacture* 48, 320-328.
- Anderson, D., Warkentin, A., Bauer, R., 2008b. Experimental validation of numerical thermal models for dry grinding. *Journal of Materials Processing Technology* 204, 269-278.
- Bansal, N.P., Zhu, D., 2005. Thermal conductivity of zirconia–alumina composites. *Ceram Int* 31, 911-916.
- Brinksmeier, E., Aurich, J.C., Govekar, E., Heinzl, C., Hoffmeister, H.W., Klocke, F., Peters, J., Rentsch, R., Stephenson, D.J., Uhlmann, E., Weinert, K., Wittmann, M., 2006. Advances in modeling and simulation of grinding processes. *CIRP Annals - Manufacturing Technology* 55, 667-696.
- Brosse, A., Naisson, P., Hamdi, H., Bergheau, J.M., 2008. Temperature measurement and heat flux characterization in grinding using thermography. *Journal of Materials Processing Technology* 201, 590-595.
- Chen, J., Xu, X., 2010. Temperature and energy partition in high-speed grinding of alumina with a brazed diamond wheel. *Machining Science and Technology* 14, 440-454.
- Doman, D.A., Warkentin, A., Bauer, R., 2009. Finite element modeling approaches in grinding. *International Journal of Machine Tools and Manufacture* 49, 109-116.
- Guo, C., Malkin, S., 1999. Energy partition and cooling during grinding. *Technical Paper - Society of Manufacturing Engineers*. MR, 1-10.
- Guo, C., Wu, Y., Varghese, V., Malkin, S., 1999. Temperatures and energy partition for grinding with vitrified CBN wheels. *CIRP Annals - Manufacturing Technology* 48, 247-250.
- Hadad, M.J., Tawakoli, T., Sadeghi, M.H., Sadeghi, B., 2012. Temperature and energy partition in minimum quantity lubrication-MQL grinding process. *International Journal of Machine Tools and Manufacture* 54–55, 10-17.
- Hahn, R.S., 1962. On the Nature of the Grinding Process, *Proceedings of the 3rd Machine Tool Design and Research Conference*, pp. pp. 129–154.
- Hazel, B., Côté, J., Laroche, Y., Mongenot, P., 2012a. Field repair and construction of large hydropower equipment with a portable robot. *Journal of Field Robotics* 29, 102-122.
- Hazel, B., Côté, J., Laroche, Y., Mongenot, P., 2012b. A portable, multiprocess, track-based robot for in situ work on hydropower equipment. *Journal of Field Robotics* 29, 69-101.

- Jaeger, J.C., 1942. Moving sources of heat and temperature at sliding contacts. Royal Society of New South Wales -- Journal and Proceedings 76, 203-224.
- James R. Hendershot, J., Miller, T.J.T.J.E., 1994. Design of Brushless Permanent-Magnet Motors. Magna Pysics Pub.
- Jin, T., Stephenson, D.J., 2004. Three dimensional finite element simulation of transient heat transfer in high efficiency deep grinding. CIRP Annals - Manufacturing Technology 53, 259-262.
- Kohli, S., Guo, C., Malkin, S., 1995. Energy Partition to the Workpiece for Grinding with Aluminum Oxide and CBN Abrasive Wheels. Journal of Engineering for Industry 117, 160-168.
- Lavine, A.S., Malkin, S., Jen, T.C., 1989. Thermal Aspects of Grinding with CBN Wheels. CIRP Annals - Manufacturing Technology 38, 557-560.
- Lin, B., Morgan, M.N., Chen, X.W., Wang, Y.K., 2009. Study on the convection heat transfer coefficient of coolant and the maximum temperature in the grinding process. International Journal of Advanced Manufacturing Technology 42, 1175-1186.
- Mahdi, M., Liangchi, Z., 1995. The finite element thermal analysis of grinding processes by ADINA, Nonlinear Finite Element Analysis and ADINA. 10th ADINA Conference, 21-23 June 1995, 2-3 ed, UK, pp. 313-320.
- Malkin, S., Anderson, R.B., 1973. Thermal aspects of grinding - 1. Energy partition. American Society of Mechanical Engineers (Paper).
- Malkin S., G.C., 2008,. Grinding Technology: Theory and Applications of Machining with Abrasives, 2nd ed. Industrial Press, New York.
- Mamalis, A.G., Kundra, J., Manolakos, D.E., Gyani, K., Markopoulos, A., 2003a. Thermal modelling of surface grinding using implicit finite element techniques. International Journal of Advanced Manufacturing Technology 21, 929-934.
- Mamalis, A.G., Kundra, J., Manolakos, D.E., Gyani, K., Markopoulos, A., Horvath, M., 2003b. Effect of the workpiece material on the heat affected zones during grinding: A numerical simulation. International Journal of Advanced Manufacturing Technology 22, 761-767.
- Mao, C., Zhou, Z.X., Ren, Y.H., Zhang, B., 2010. Analysis and FEM simulation of temperature field in wet surface grinding. Mater Manuf Process 25, 399-406.

- Mohamed, A.L.M., Warkentin, A., Bauer, R., 2012. Variable heat flux in numerical simulation of grinding temperatures. *The International Journal of Advanced Manufacturing Technology* 63, 549-554.
- Mohamed, A.L.M.O., Warkentin, A., Bauer, R., 2011. Use of surface roughness measurements to improve the estimation of the heat partition in grinding. *Journal of Materials Processing Technology* 211, 566-572.
- Rafieian, F., Girardin, F., Liu, Z., Thomas, M., Hazel, B., 2013. Angular analysis of the cyclic impacting oscillations in a robotic grinding process. *Mechanical Systems and Signal Processing*.
- Robert D. Cook, D.S.M., Michael E. Plesha, Robert J. Witt, 2007. *Concepts and Applications of Finite Element Analysis*. John Wiley & Sons
- Rowe, W.B., Pettit, J.A., Boyle, A., Moruzzi, J.L., 1988. Avoidance of Thermal Damage in Grinding and Prediction of the Damage Threshold. *CIRP Annals - Manufacturing Technology* 37, 327-330.

CHAPTER 3

CHARACTERIZATION OF GRINDING WHEEL GRAIN TOPOGRAPHY UNDER DIFFERENT WORKING CONDITIONS IN A ROBOTIC GRINDING PROCESS USING CONFOCAL MICROSCOPE

Amir Masoud Tahvilian¹, Zhaoheng Liu^{1*}, Henri Champlaud¹, Bruce Hazel², Marin Lagacé²

⁽¹⁾Department of Mechanical Engineering, École de technologie supérieure,
Montréal, Québec, H3C 1K3, Canada

⁽²⁾Expertise Robotique et civil, IREQ, Hydro-Québec's research institute
Varenes, Québec, J3X 1S1, Canada

This article is submitted to “International Journal of Advanced Manufacturing Technology”
in October 2014

Highlights

- New method distinguishes grains from resin bond in wheel structure.
- Only grain edges facing the cutting direction are considered.
- Grain topography is extracted for disk and cup grinding wheels.
- Yaw and rake angle results show a uniform and normal distribution, respectively.
- Mean rake angle tends to have a higher negative value at lower grinding power levels.

3.1 Abstract

Knowing the grain geometry in grinding wheels is an asset for better understanding the grinding processes. This study investigates the grain protrusion and rake angles of two self-dressing zirconia-alumina grinding wheels in a robotic grinding process. The topography of the wheel is measured using a confocal scanning laser microscope. An optical image of the surface is used to create a mask of the grains with image processing techniques. Grain geometry information is then obtained by applying the mask to the entire surface. A vertex normal technique is used to find the cutting edges facing the cutting direction and only

consider those edges in grain rake angle calculations. Surface parameters, including grain density, width, protrusion height and rake angle, are extracted from the topography. The grinding wheel is characterized in low, medium and high depths of cut in the range of robot operation. Results indicate that grain density, width and protrusion height distribution are not affected by the depth of cut. It is also found that in shallow grinding, grain rake angle shifts slightly to higher negative angles; whereas, with a higher depth of cut, sharper edges exist on the wheel surface, which improve process efficiency.

Keywords: Grinding wheel topography, 3D laser scanning, grain rake angle, robotic grinding process

3.2 Introduction

Grinding may be viewed as the combination of several micro-machining processes performed by individual grains in the wheel. Each grain's orientation and protrusion significantly influence its cutting ability. Consequently, overall grinding performance, including the grinding force, temperature and surface finish, is largely affected by the grinding wheel's characteristics. There is thus considerable interest in gaining an understanding of grain size, grain shape and protrusion topography in order to simulate micro-material removal. Though such micro simulations have been extensively investigated in the literature, the grain shape has most often been assumed to be spherical or conical for simulation purposes. Doman et al. (2009a) considered the grains to be spherical bodies in order to perform finite element analyses of the rubbing and plowing phases of material removal by a single grain. Some models have considered the grit to be of constant diameter with a random spatial distribution. In more advanced models, a probability of various grain sizes is considered in order to better represent the actual topography. Liu et al. (2013) used a grain distribution process where an initial uniform grain configuration is first specified, the topography then adjusted for varying grain sizes and, lastly, a shaking function applied to position grains randomly. (Aurich and Kirsch, 2012) develop a more sophisticated model for grains, selecting grain shapes that are 50% octahedrons and 50% tetrahedrons. The authors

use the grain topography in a kinematic simulation to investigate material removal by individual grains. Clearly, nothing short of 3D measurements of the grinding wheel surface can fully reveal the grain topography.

Several methods have been applied in the literature to determine or characterize the grinding wheel surface. Verkerk (1977) and Lonardo et al. (1996) are among the first to review progress in characterizing grinding wheel topography. The authors classified surface analysis as either 2D (elevation traced on a line) or 3D (elevation measured over an area) and measurement methods as either contact or non-contact.

Regarding contact methods, Blunt and Ebdon (1996) used 3D contact profilometry to characterize the topography of two different grinding wheels under similar dressing conditions. The authors showed that sampling size significantly affects results when using a stylus-based measuring instrument. They suggested an optimum sampling space by comparing the number of visually counted active grains to number of detected peaks, defined as the highest point among its eight neighbors. Ignoring this factor may lead to overestimating the number of grains since cutting edges are counted rather than actual grains. The authors propose an optimum sampling space (S_{opt}) given by $dg/4 < S_{opt} < dg/3$, where dg is the grain diameter.

Butler et al. (2002) used a Somicronic 3D stylus instrument to measure the topography of the grinding wheel and tried to relate it to the grinding forces. The authors determined the sampling space using the same techniques as in the earlier study and mentioned the need to identify active grains. Three parameters from the European Union standard for 3D topography have been used in this study to characterize the surface: summit curvature, density of summits and RMS (root mean square) roughness. Nguyen and Butler (2008) proposed a new criterion for the optimal sampling size in stylus profilometry, mentioning that using the mean diameter ignores the distribution of grain sizes and shapes. The authors correlated wheel topography to grinding performance. Xie et al. (2008) used a coordinate measuring machine (CMM) to investigate grain cutting edges on a diamond grinding wheel's

surface in terms of rake angle and clearance angle.

Generally, in all contact profilometry methods, it is impossible to distinguish between the grains and the bonding material. Also, small details are missed due to the stylus or probe size. Other sources of error, like stylus-wheel contact pressure and rapid stylus wear, may affect measurement results (Verkerk, 1977).

Regarding non-contact methods, Lachance et al. (2003) developed a system to measure wear flat areas on a grinding wheel surface using a conventional optical microscope. The authors employed image processing software to analyze their grayscale digital images of the grinding wheel and map on each the wear flat areas by applying a color threshold to the pixels. Inasaki (1996) applied an optical profilometry technique in which the height of each point on the surface is determined by tracking the movement of an auto-focus lens. With the help of a very accurate X-Y stage attached to this system, a 3D representation of the surface can be obtained. Grain detection in this study is based on a two-step algorithm. First, the cutting edge distribution at a given height is determined. Then, a search is made for closed-loop edges, which are regarded as cutting edges. Yan et al. (2011) employed a white-light interferometer method to characterize the surface topography of two alumina grinding wheels. The authors took three parameters (grit density, grit sharpness and chip space) from the Birmingham set, the best known standard for 3D surface analysis (Blunt and Jiang, 2003). They modeled all grains as blunt cones and tried to obtain the tip radius and cone angle for all measured grains. The same optimum sampling space was used as previously (Blunt and Ebdon, 1996) to avoid counting cutting edges rather than grains since one grain may have more than one cutting edge. The eight-nearest-neighbor criterion was again used to define peaks.

Weingaertner and Boaron (2012) developed an acoustic emission (AE) method for characterizing grinding wheel topography. It is based on mapping the captured AERMS signal originating from interference between wheel surface grains and a diamond tip. Interference between the grinding wheel and diamond tip is kept within the elastic range (1

μm) to avoid damaging grains. Although the authors validated AE maps of grinding wheel topography obtained with grinding wheel imprints and other models from literature, this method only locates and counts the number of kinematic cutting edges; it does not provide a geometrical topography. Matsuno et al. (1975) used a scanning electron microscope (SEM) to study the grinding wheel surface. Although the SEM is among the best options to distinguish between the grains and bonding material, it is expensive and impractical since the microscope's small chamber can only accommodate small samples.

3.3 Grain detection methods in wheel topography

Recent studies focused more effort on distinguishing grains from the bonding material in the topography. Cui et al. (2013) used white-light interferometry (WLI) to build a 3D topography of diamond grains. The authors used reflected peak intensities to distinguish grains on resinoid-bonded wheel. The main idea is that the diamond grains should reflect light at a higher peak intensity than the bonding material. Grain detection is thus achieved by applying a threshold to the peak intensity. This method has three main drawbacks. First, disturbance by environmental light may cause false peaks. Second, the method is only applicable to materials of higher reflectivity than the bonding material. Third, the small measurement area is not conducive to statistical analysis. Xie et al. (2011) used a laser microscope to investigate the grain topography of a diamond grinding wheel. The authors applied chloroazotic acid to the wheel's surface to remove the metal bond without damaging the diamond grains. This method ensures that the observed 3D topography is that of the actual abrasive grains, not that of the bonding material. The aim of the study is to characterize wheel protrusion topography in terms of grain height, volume, rake angle and clearance angle, and to correlate these parameters to grinding performance. Darafon et al. (2013) used a white-light chromatic sensor to build a non-contact WLI wheel scanning system to characterize grinding wheel topography. They used a motorized stage to move the sensor across the wheel surface for measurement over a large area. The system was used to measure an aluminum oxide grinding wheel. The results were compared to other measurements method like SEM and profilometry.

In this paper, a confocal laser microscope is used to measure the grain protrusion topography of two self-dressing zirconia-alumina grinding wheels used for robotic grinding in turbine runner rehabilitation. The objective is to investigate grain topography, including grain density, width, protrusion height and rake angle. In the next step, single-grain cutting simulations will be performed to obtain cutting forces. The results from these micro-material removal simulations will be compiled to obtain a statistical force model for the overall cutting area.

3.4 Experiments and preparation

Two types of grinding wheels, disk and cup, are considered in this study. They are commonly used with a light, flexible robot tool holder named “SCOMPI” in grinding processes for hydro turbine maintenance. The disk wheel is used for very high material removal rates. The cup wheel is more versatile for medium and low material removal rates. The robotic repair process has been in use at Hydro-Québec for a number of years. The disk grinding wheel in the experiments is a NORZON III depressed-center, 9" diameter, ¼" thick, heavy-duty foundry type 27, with grit size of 24 to 46. The cup grinding wheel used in the experiments is a NORZON IV, 5" front, 3-13/16" back diameter, 2" thick, type 11, with grit size of 14 to 24. Both wheels have zirconia-alumina grit and resin bonding.

For each wheel type, traverse grinding is performed with grinder power levels of 1,000, 1,500 and 2,000 W, a constant feed speed of 80 mm/s and a rotation speed of 6,000 rpm. Each grinding experiment is carried out long enough for the grinding wheel to reach steady-state. Figure 3-1 shows the laboratory setup used to perform the grinding test with SCOMPI. Three regions are selected on each wheel for measurements in order to provide sufficient statistical data. The entire cup wheel can be mounted under the microscope for measurements; whereas, destructive sample preparation is necessary for the disk wheel (see Figure 3-2). The samples are mounted on custom-built fixtures, designed to properly align the region of interest under the microscope.

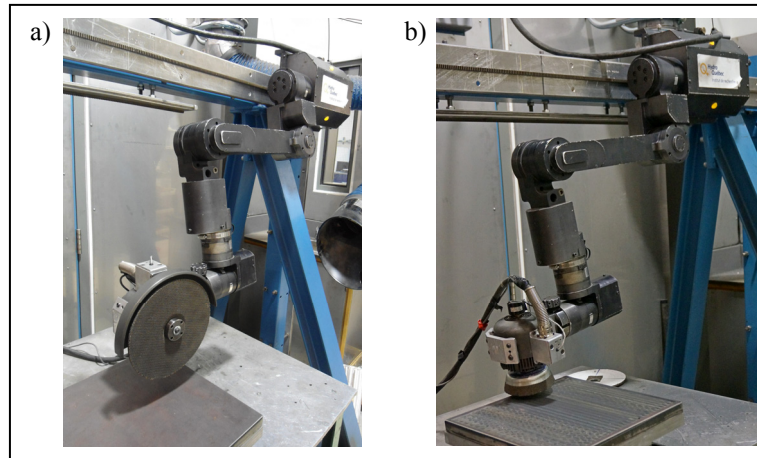


Figure 3-1 Laboratory setup of SCOMPI for grinding experiments, (a) disk wheel, (b) cup wheel

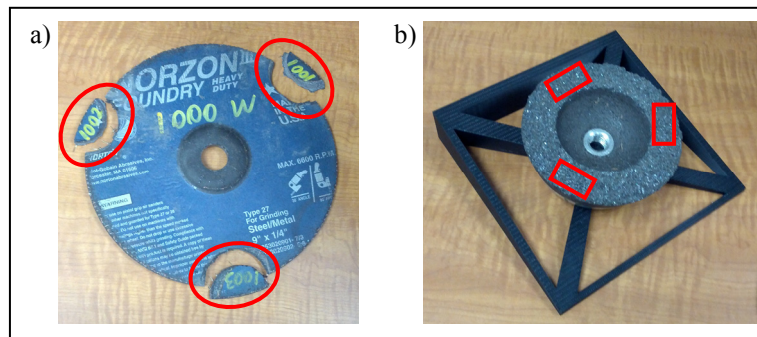


Figure 3-2 Samples of the grinding wheel prepared for measurements, (a) disk wheel, (b) cup wheel

3.5 3D topography measurement

A 3D laser confocal microscope (Keyence VK-X210) was employed to observe grain protrusion and topography. This microscope is capable of capturing an optical image as well as 3D topography. Four external angled lights were used to enhance optical image contrast and quality. Figure 3-3 shows the measurement equipment and external light sources.

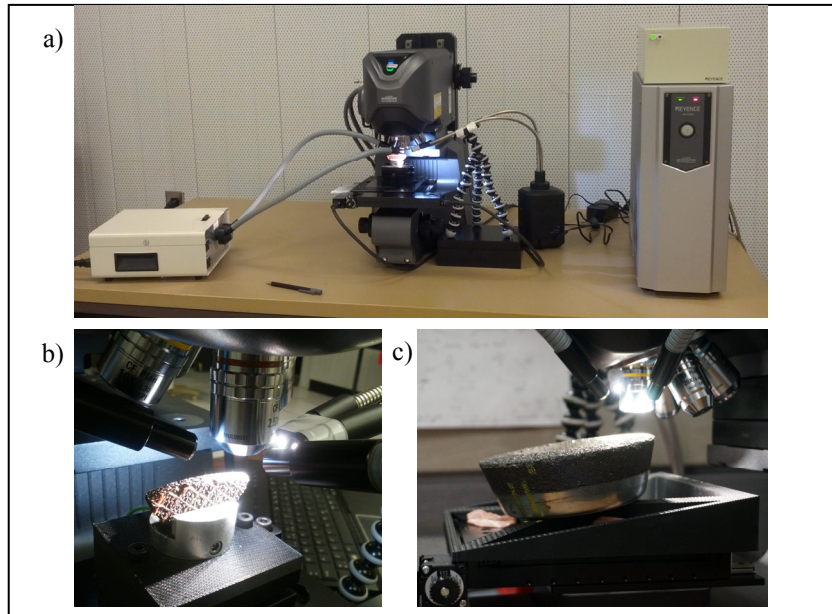


Figure 3-3 (a) Confocal microscope with external light source, (b) disk wheel sample and (c) cup wheel

Malkin S. (2008) introduced the following equation to calculate the average grain size (d_g) for conventional grinding wheels in millimetres,

$$d_g = 15.2M^1 \quad (3.1)$$

where M is the grit size. Given the stated grit size for the grinding wheels studied, grain size should range from 300 to 600 μm for the disk wheel and from 600 to 1,000 μm for the cup wheel. A 200X overall magnification was thus used. The captured image size is 1,024 x 768 pixels. This ensures a sufficiently small sampling space (2.8 μm), which should be adequate to capture all cutting edges of the grains.

For each of the three regions of interest, 84 images (14 horizontal x 6 vertical) for the disk wheel and 90 images (9 horizontal x 10 vertical) for the cup wheel were acquired. The images were stitched together to give one final image covering an area of 17.7 x 5.7 mm for the disk wheel and 11.5 x 9.2 mm for the cup wheel. Figure 3-4 shows a typical optical image of the disk wheel and its corresponding 3D topography.

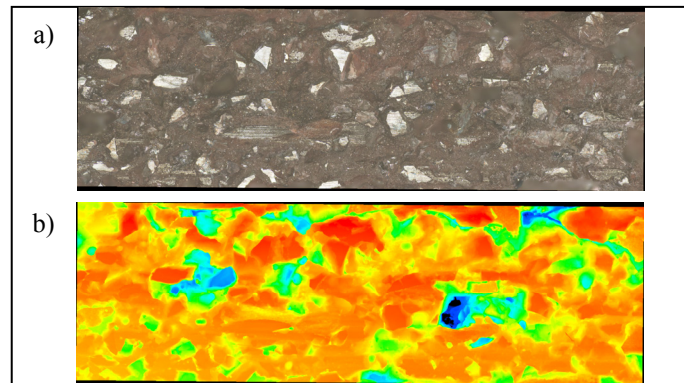


Figure 3-4 (a) Optical image (b) topography of the same region

3.6 Data processing

This section explains the methods used to process the 3D topography and extract useful information for individual grains from the raw measured data. The whole image processing and data extraction process used for grinding wheel characterization is shown in Figure 3-5.

An important first step is to distinguish between the grains and the surrounding bonding material in the 3D topography measurements. As explained in preceding sections, several methods have been used for this purpose in the literature. These methods include, eight-nearest-neighbors peak, visual inspection of SEM images, bond material removal with a corrosive chemical, monitoring reflected light intensity for diamond grains and applying a height threshold to detect cutting particles. In this study a novel approach is proposed: analyzing the optical image of the scanned surface to find grain positions

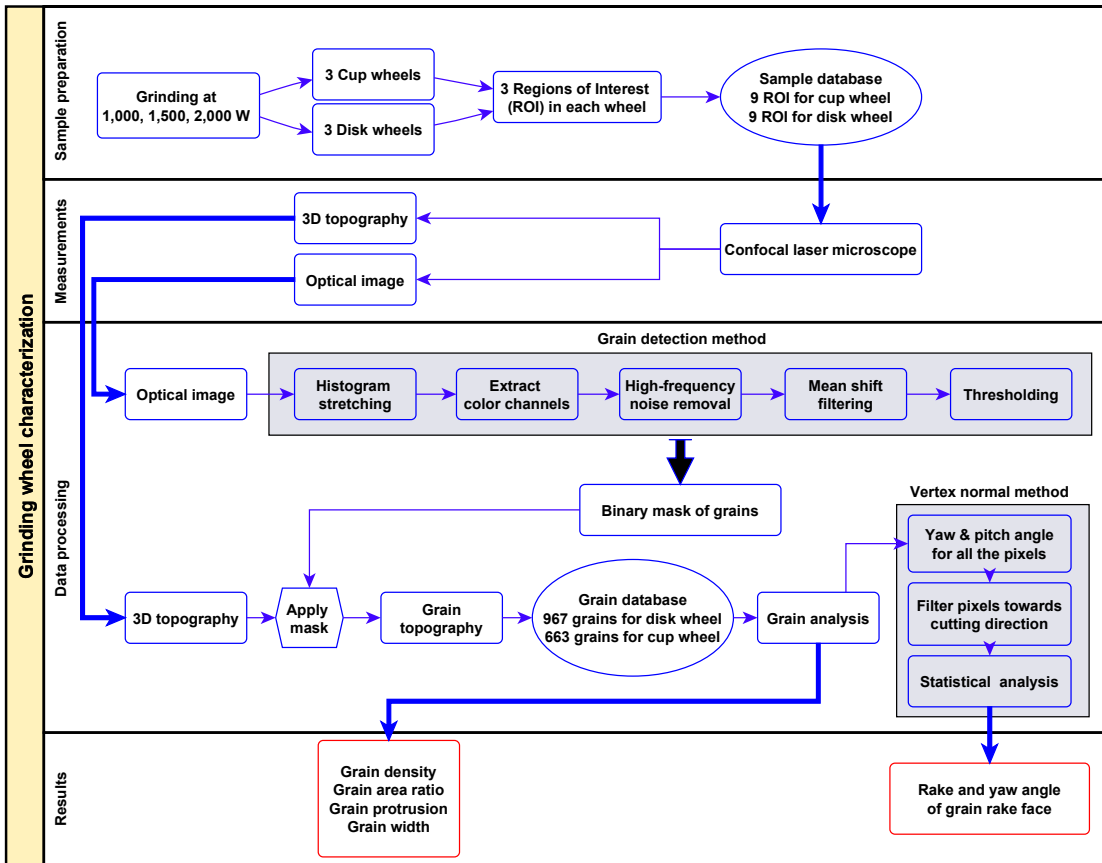


Figure 3-5 Process for grinding wheel characterization

A series of image processing steps are employed to create from the optical image a mask of the grains, which is then applied to the 3D topography to discard bonding regions. At first, the histogram of the image is stretched to enhance image contrast. Figure 3-6 shows the optical image and its histogram before and after stretching. The three color channels are then split and the blue channel, which had the highest contrast, is selected for the rest of the operation.

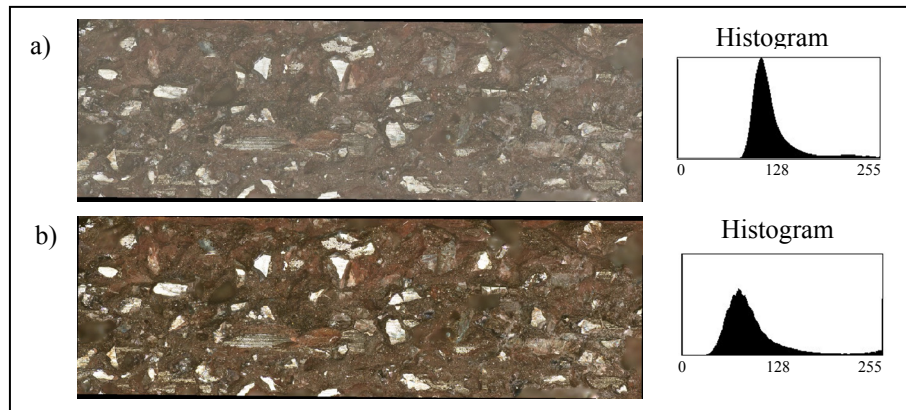


Figure 3-6 Optical image enhancement through histogram stretching, (a) raw image, (b) after stretching

Next, a 2D low-pass filter with a Butterworth kernel is applied in the frequency domain to remove the noise from the image (Gonzalez and Woods, 2007). Filtering is done in the frequency domain rather than in the spatial domain for shorter computation time. The filter kernel is given below,

$$f = \frac{1}{1 + \left(\frac{r}{c_f}\right)^{2n}} \quad (3.2)$$

where r is the normalized distance of each pixel from the center, c_f is the normalized cutoff frequency selected as 0.05 (150 pixels) and n is the filter power, which is selected as one to eliminate the ringing effect and to smooth the transition between high and low frequencies. Filter parameters were selected through trial and error to obtain the best output given the trade-off between noise removal and image blurring. The Butterworth filter transfer function magnitude and the 2D FFT of Figure 3-6 before and after applying the filter are shown in Figure 3-7. The horizontal and vertical axes are the image pixels.

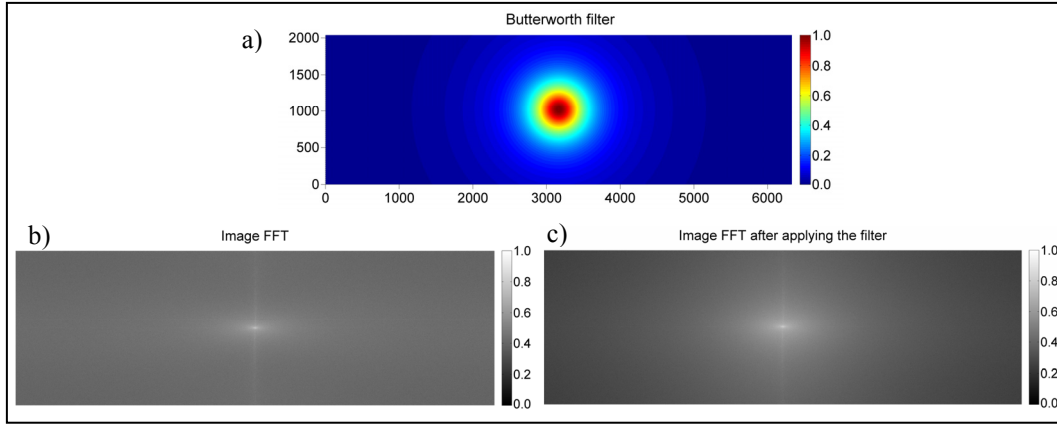


Figure 3-7 (a) Butterworth filter, (b) original FFT image, (c) filtered FFT image

To perform segmentation with a color threshold, the image must be smoothed. However, most smoothing filters will blur the image causing the loss of edges. As the next step, a smoothing algorithm called “mean shift filtering” is applied to the images (Roberto Rodríguez et al., 2012). This filter smooths the images and removes shading while preserving the edges for segmentation purposes. In the mean shift algorithm, for each pixel $S^k(c, x, y)$ a set of neighbors within the specified radius (R) and color distance (C) is defined through a kernel function $K(S_i, S)$. Then, a new color mean \bar{c} and spatial center coordinates (\bar{x}, \bar{y}) in the form of $S^{k+1}(\bar{c}, \bar{x}, \bar{y})$ are calculated with Equation (3.3). These become the new parameters for the next iteration. This loop will continue until the changes in the spatial mean and color mean become zero. The final color value will be assigned to the initial pixel of the iteration process and the procedure continues for the next image pixel (Comaniciu and Meer, 2002).

$$S^{k+1} = \frac{\sum_{i=1}^N K(S_i, S^k) S_i}{\sum_{i=1}^N K(S_i, S^k)} \quad (3.3)$$

where N is the total number of pixels in the image and k is the number of iteration in progress. Using a circular flat kernel we can write,

$$K(S_i, S^k) = \begin{cases} 1 & r_i \leq R \text{ \& } (c_i - c) \leq C \\ 0 & r_i > R \text{ \& } (c_i - c) > C \end{cases} \quad (3.4)$$

where $r_i = \sqrt{(x_i - x)^2 + (y_i - y)^2}$ is the distance of each neighbor from the center pixel, C and R are kernel values for spatial radius and color distance, respectively. Figure 3-8 illustrates the results of mean shift filtering the optical image for spatial radius of 40 pixels and color distance of 30 with a circular flat kernel mentioned above (Equation (3.4)).

A binary mask is then created by setting a color threshold. The mask is further processed by removing small objects from the foreground and filling the holes in the grains detected.

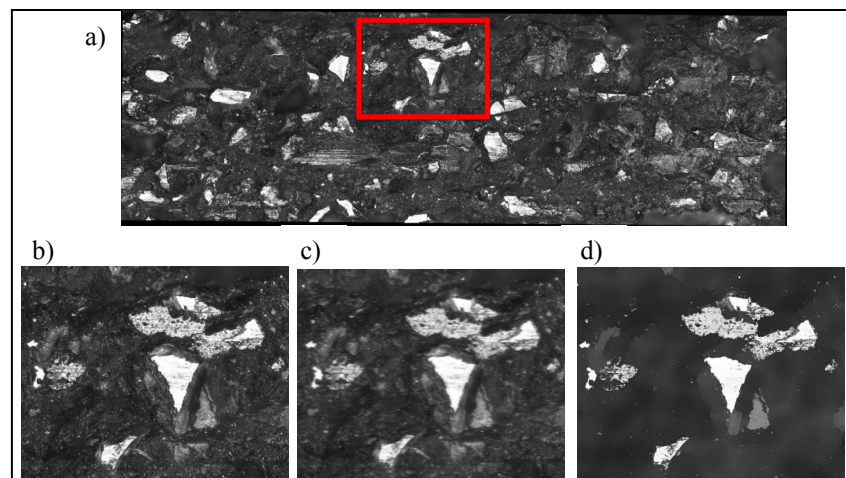


Figure 3-8 (a) One channel optical image of the wheel surface, (b) zoom of the region in red, (c) after high-frequency noise removal, (d) after mean shift filtering

Finally border smoothing and a visual check are performed to add any missed grains in the mask. Note that this method detected approximately 80% of the grains automatically. The binary mask is then overlaid on the topography image to extract grain geometry for the region of interest. Figure 3-9 shows the final overlay of detected grains in the optical image and its mask, as well as 3D representation of the wheel surface and grain topography. This procedure was performed on images obtained from both grinding wheel types (disk and cup) at three grinding power levels (1,000, 1,500 and 2,000 W).

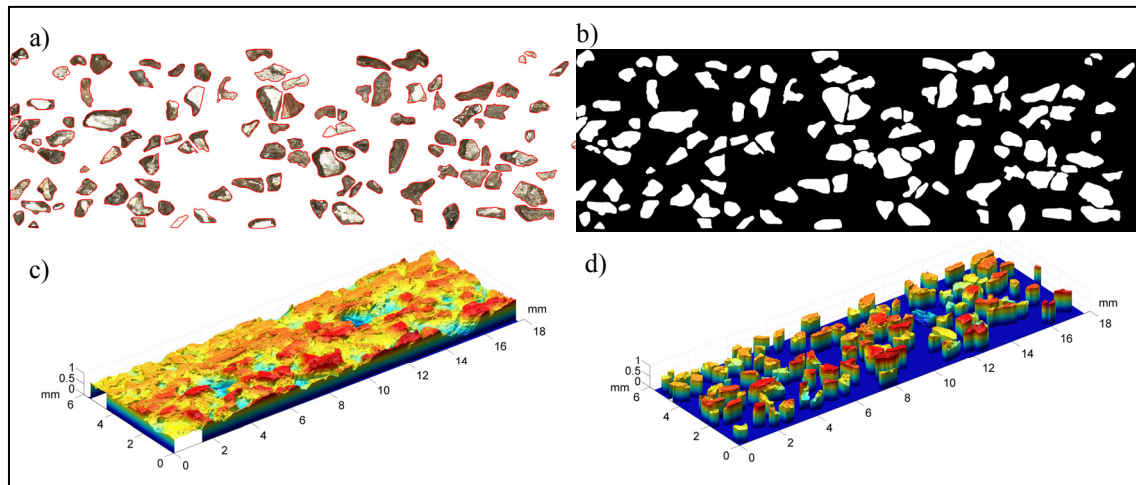


Figure 3-9 (a) Optical image of grains, (b) binary mask of grains, (c) 3D topography of wheel as measured with the microscope, (d) 3D topography of grains with overlaid mask to remove the bonding region

3.7 Results and discussion

Three regions of 17.7 x 5.7 mm (100.9 mm²) and of 11.5 x 9.2 mm (105.8 mm²) were scanned for the disk wheel and the cup wheel respectively. This gives a total scanned area of 302.7 mm² for the disk wheel and of 317.4 mm² for the cup wheel for each of the three grinding power levels tested. Table 3.1 lists the general statistics for the disk and cup wheel samples respectively. The grinding power levels in watts (1,000, 1,500 and 2,000) with the prefix “P” are used for naming each case. The three scanned regions on each wheel are distinguished by the suffixes “a”, “b” and “c”. Results from the three regions analyzed are summarized in the highlighted rows.

The results show that, for the disk wheel, about one quarter of the wheel surface area (25%) is covered with grains and that grain density is about 1 grain per square millimetre on the wheel surface. For the cup wheel, about 40% of the wheel is covered with grains and grain density is about 0.7 grains per square millimetre on the wheel surface. This is due to larger grains on the cup wheel than on the disk wheel.

Table 3.1 Statistics for the disk and cup wheel

Disk wheel					Cup wheel				
Sample Name	Number of Grains Processed	Grain Area / Total Area (%)	Grain Density (No./mm ²)	Average Grain Width (mm)	Sample Name	Number of Grains Processed	Grain Area / Total Area (%)	Grain Density (No./mm ²)	Average Grain Width (mm)
P1000a	124	24.1%	1.23	0.49	P1000a	74	41.4%	0.70	0.88
P1000b	106	24.9%	1.05	0.53	P1000b	85	42.3%	0.80	0.81
P1000c	139	24.3%	1.38	0.46	P1000c	73	37.3%	0.69	0.83
P1000	369	24.4%	1.22	0.49	P1000	232	40.3%	0.73	0.84
P1500a	119	21.8%	1.18	0.46	P1500a	78	43.2%	0.73	0.88
P1500b	94	27.8%	0.93	0.59	P1500b	82	39.9%	0.78	0.78
P1500c	88	25.4%	0.87	0.55	P1500c	61	34.5%	0.58	0.87
P1500	301	25.0%	0.99	0.53	P1500	221	39.2%	0.70	0.84
P2000a	110	26.0%	1.09	0.50	P2000a	72	45.0%	0.68	0.95
P2000b	89	25.8%	0.88	0.48	P2000b	83	39.6%	0.78	0.80
P2000c	98	24.6%	0.97	0.53	P2000c	55	33.0%	0.52	0.90
P2000	297	25.5%	0.98	0.50	P2000	210	39.2%	0.66	0.88

3.7.1 Grain analyses

In this section, individual grain topography is studied to determine the rake angles of its cutting surface. Two angles, pitch and yaw, are defined as illustrated in Figure 3-10. The pitch (commonly called “rake” in grinding) is the angle between the cutting face normal and wheel surface, ranging from 0 to 90 degrees. The yaw is the angle between the normal

projection on the wheel surface and the cutting direction axis, ranging from -180 to 180 degrees.

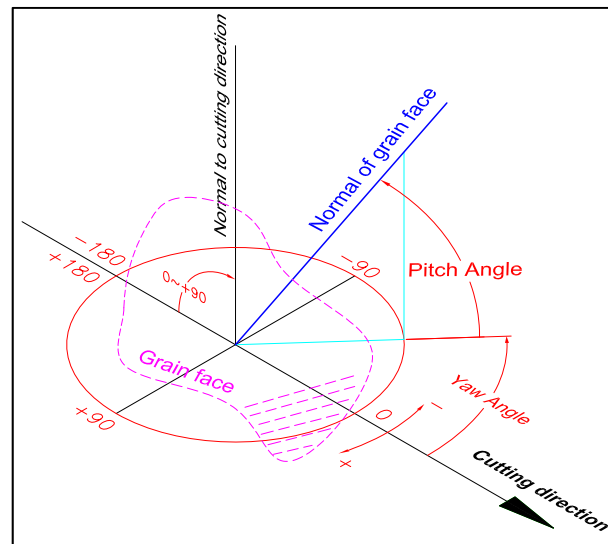


Figure 3-10 Pitch and yaw angle with respect to cutting direction

In order to extract the normal to the cutting surface for each grain, principal component analysis (PCA) is used. PCA is a statistical procedure that uses an orthogonal transformation to convert a set of possibly correlated variables to a series of uncorrelated variables called “principal components”. The first two principle components represent the best-fit plane for the data set and the third component is the normal of the plane. Figure 3-11a shows a sample grain with its best-fit plane using PCA. This method, called plane fit in this study, will work properly provided the grain is of a shape with one dominant face. However, if the grain has two or more faces, ambiguity results will be obtained. Figure 3-11b illustrates this problem with a grain having two faces. Rather than one single plane, two planes should be fitted, one for each slope of the grain, in order to have the correct normal directions. The face which is pointing toward the cutting direction ($-90 < \text{yaw} < +90$) should then be picked as the rake face of the grain.

Therefore, a second method was employed to extract the normal of each pixel based on its neighbors. This method adds the capability to discard pixels residing on the face opposite to the cutting direction. Figure 3-12 shows the same two-faced grain as in Figure 3-11b with the normal of its pixels plotted. To simplify Figure 3-12, the number of pixels is reduced and a limited number of normal vectors are plotted.

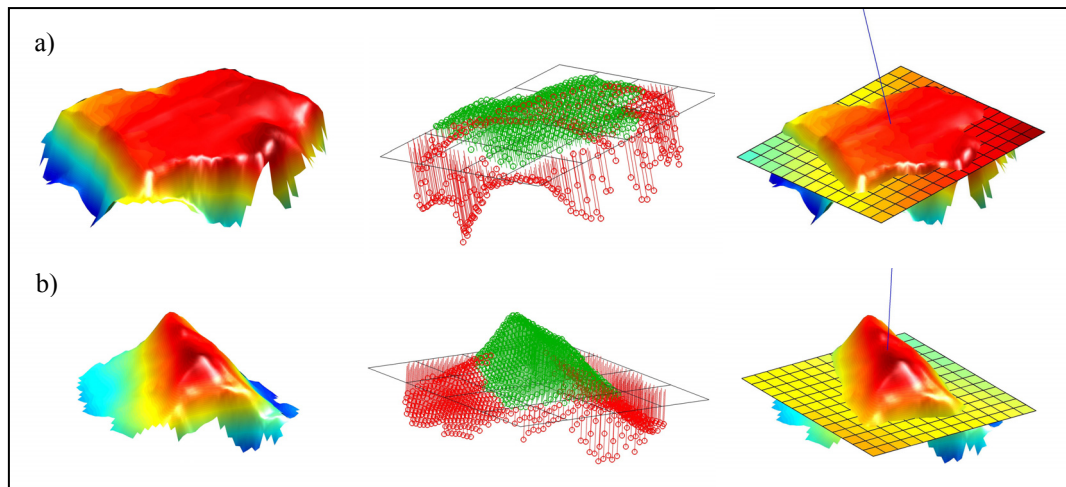


Figure 3-11 Normal extraction with plane fit method, (a) good result (grain with one face), (b) ambiguous result (grain with two faces)

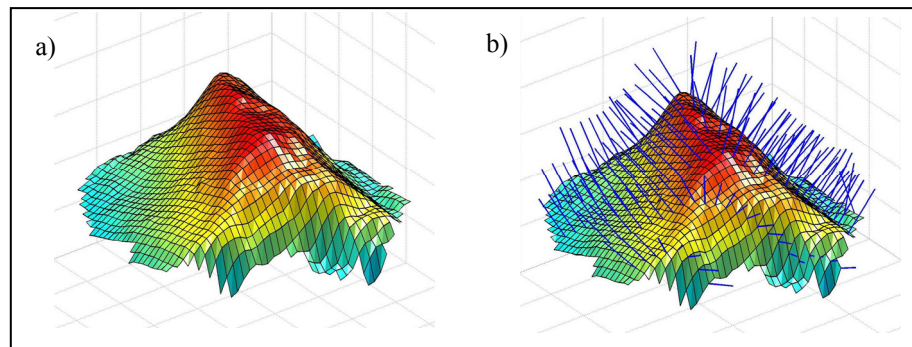


Figure 3-12 a) Grain surface without normal vectors, b) grain surface with vertex normal vectors

First, for each grain, the pitch and yaw angles at all of the pixels are extracted. Figure 3-13 shows the height and color map of the pitch and yaw angles for a sample grain. The pixels with a yaw angle above $+90$ or below -90 degrees are removed from the color maps on the

right. This means that the pixels not facing the cutting direction are removed from the analysis. Then the angles of highest occurrence are selected as the pitch and yaw angles for the grain.

Figure 3-14a shows the histogram of the probability for yaw angles considering all the grain's pixels. There are two maxima in the distribution: -10 degrees related to the green face of Figure 3-13c and 150 degrees related to the red face of Figure 3-13c. Figure 3-14b illustrates the same histogram without the pixels facing away from the cutting direction. Lastly, Figure 3-14c shows the rake angle histogram for the grain's pixels facing the cutting direction. The information for grain rake angles extracted using this method come only from the cutting faces. The results for rake and yaw angle probability distributions at different power levels for both disk and cup wheels are presented in the next section.

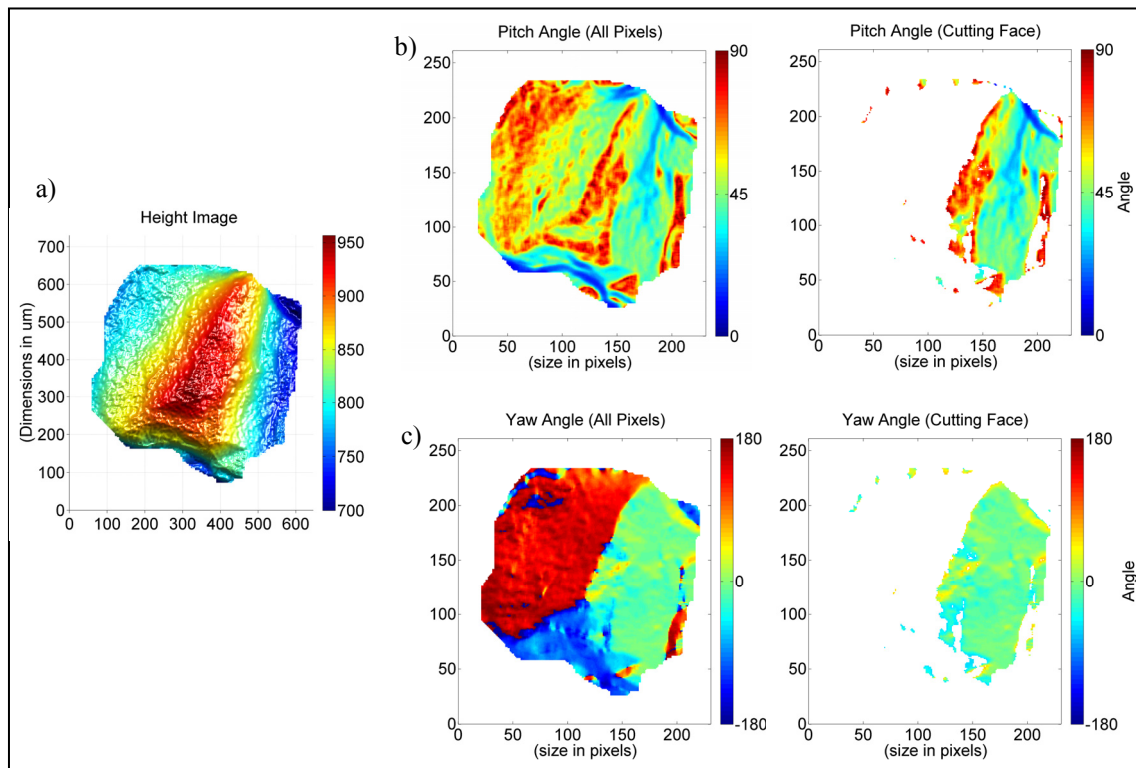


Figure 3-13 a) Height topography image, b) pitch angle for the whole grain (left), only the cutting face (right), c) yaw angle for the whole grain (left), only the cutting face (right)

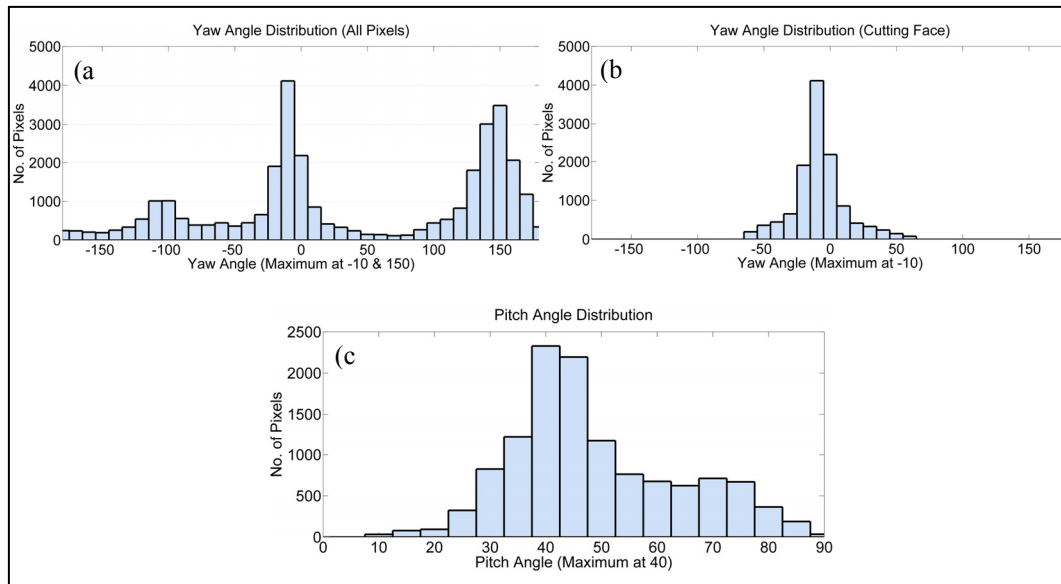


Figure 3-14 a) Yaw angle distribution for the whole grain, b) for cutting face pixels, c) pitch angle distribution for cutting face pixels

3.7.2 Grain rake and yaw angles distribution

Figure 3-15 shows the yaw and rake angle distributions for the disk wheel obtained by processing close to 950 grains. The yaw angle is shown from -85 to +85 degrees, which is the range for grains facing toward the cutting direction; other faces are discarded for the process as discussed above. It can be seen from these histograms that at all power levels, the yaw angle distribution is quite uniform. Also, there are no significant changes in the probability of yaw angles at different power levels. However, the rake angle distributions look more like normal distributions. They are slightly shifted toward higher negative values at lower grinding power levels. This can be explained as higher grinding power leads to higher normal and tangential forces in the material removal process making the self-sharpening effect in the wheel more dominant. Therefore, dull grains are pulled out of the wheel structure and new sharp edges come into contact with the workpiece.

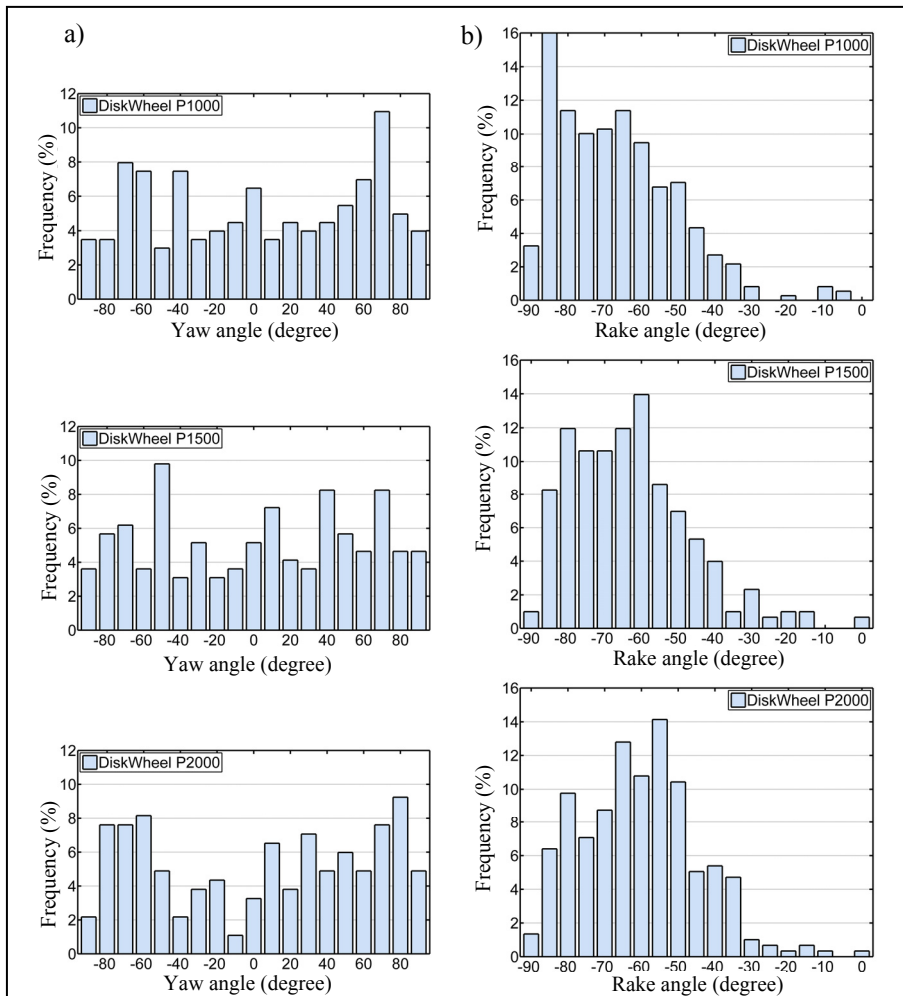


Figure 3-15 Distribution of (a) yaw angles and (b) rake angles at different power levels for disk wheel

Figure 3-16a shows the yaw angle distribution for the cup wheel. A total of 650 grains were processed for the cup wheel at the three power levels. As with the disk wheel, yaw angles are uniformly distributed. Figure 3-16b shows the occurrence of rake angles for the cup wheel. The slight left shift of the normal distribution toward higher negative rake angles at lower power levels is again evident.

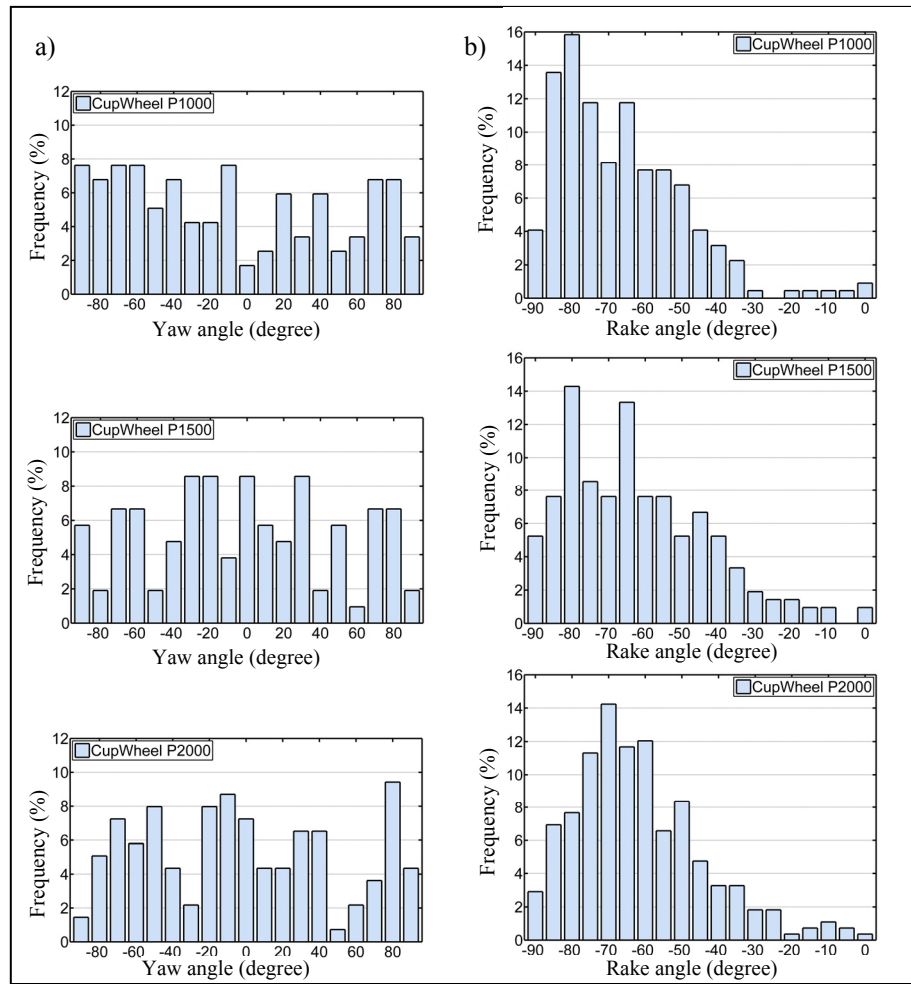


Figure 3-16 Distribution of (a) yaw angles and (b) rake angles in different grinding conditions for cup wheel

Figure 3-17 compares rake angle probability distributions at different power levels using a side-by-side color map. The rake angle distribution peaks for 1,000, 1,500 and 2,000 W are at approximately -85, -70 and -55 degrees for the disk wheel and -85, -75 and -65 degrees for the cup wheel, respectively.

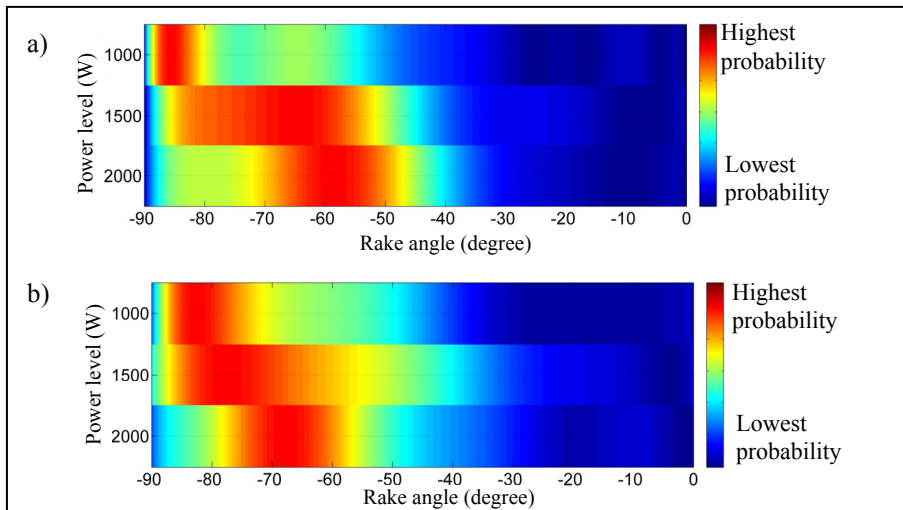


Figure 3-17 Comparison of grain rake angle probability at different power levels for (a) disk wheel, (b) cup wheel

3.7.3 Grain protrusion height and width

In order to investigate grain protrusion height, a virtual reference plane is placed $500\ \mu\text{m}$ below the highest point in the wheel topography. Then, the height of each grain is defined after removing outliers by the three-sigma rule. In other words, the height of the grain is assigned the maximum value of pixel heights within three standard deviations of the mean height for that grain.

Figure 3-18a and Figure 3-19a show the grain protrusion height for disk and cup wheels, respectively. These distributions are found to be similar for each wheel type regardless of power level. Figure 3-18b and Figure 3-19b show the distributions of processed grain width (perpendicular to the cutting direction) for disk and cup wheels. At all power levels, a normal distribution with a mean value of about $500\ \mu\text{m}$ for the disk wheel and $800\ \mu\text{m}$ for the cup wheel is observed. This is expected based on the wheel grit size, as mentioned earlier.

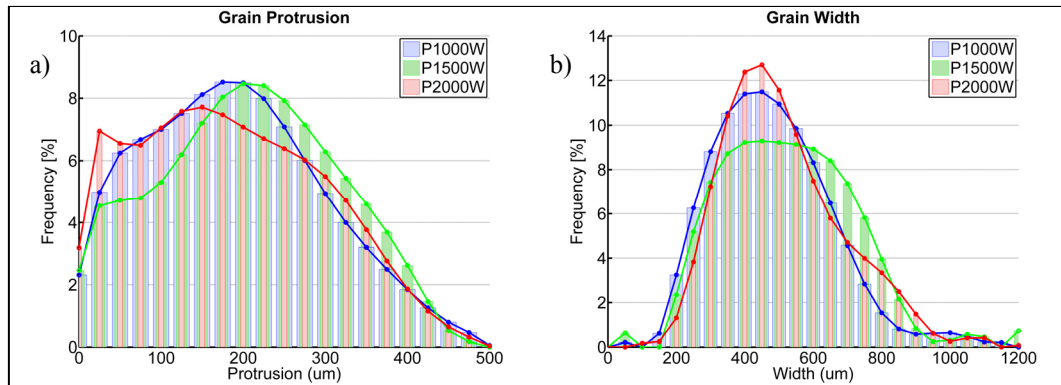


Figure 3-18 (a) Grain protrusion and (b) grain width probability for disk wheel

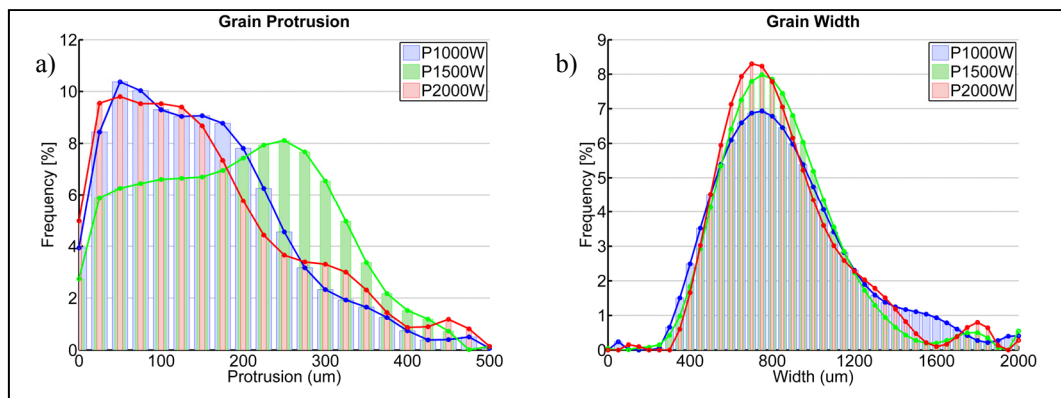


Figure 3-19 (a) Grain protrusion and (b) grain width probability for cup wheel

3.8 Conclusion and summary

A new method was developed that distinguishes grains from the resin bond material in the grinding wheel structure by processing the optical image of the surface. The topography of two types of grinding wheel, disk and cup, are captured using a laser confocal microscope. A grain mask is generated by performing a sequence of image processing techniques such as high-frequency FFT noise removal, mean shift smoothing and segmentation through thresholding. The mask is applied to the wheel topography to obtain grain height data for processing. Two fitting methods named “plane fit” and “vertex normal” were tested for detecting the grain face in the cutting direction and extracting the rake and yaw angles of each grain. Care has been given to only extract information for grain faces oriented toward the cutting direction by using the vertex normal method. Large areas from different regions

of each grinding wheel type are scanned to provide enough data for statistical analysis. The wheels are characterized at three different grinding power levels (1,000, 1,500 and 2,000 W) typical of those used in actual field applications. Grain rake angles, yaw angles, width and protrusion height for each type of wheel and power level are then extracted.

It is found that the yaw angles have a uniform distribution under all conditions studied regardless of wheel type or power level. For both wheel types, however, rake angle results approximate a normal distribution with the mean tending toward higher negative angles at lower grinding power levels. Grain protrusion and width results are also obtained through the procedure developed. These results are essential for simulating micro-material removal by a single grain. Grain protrusion heights are also needed to determine the active grains based on the specific grinding depth of cut. The work reported in this paper will be used for subsequent numerical modeling of the grinding process in the framework of single-grain simulations. Grain geometry statistics will be used as a database to perform a series of single-grain cutting actions. A comprehensive model for material removal in the robotic grinding process studied will then be built based on the kinematics of the contact zone and grains active in the removal process.

3.9 Acknowledgements

The authors would like to thank the SCOMPI team at IREQ, Hydro-Québec's research institute. The authors would also like to express their gratitude to the Natural Sciences and Engineering Research Council of Canada (NSERC) and to Hydro-Québec for supporting this research.

3.10 References

Aurich, J. C. and B. Kirsch (2012). "Kinematic simulation of high-performance grinding for analysis of chip parameters of single grains." CIRP Journal of Manufacturing Science and Technology 5(3): 164-174.

- Blunt, L. and S. Ebdon (1996). "The application of three-dimensional surface measurement techniques to characterizing grinding wheel topography." International Journal of Machine Tools and Manufacture 36(11): 1207-1226.
- Blunt, L. and X. Jiang (2003). Advanced Techniques for Assessment Surface Topography: Development of a Basis for 3D Surface Texture Standards "Surfstand", Elsevier Science.
- Butler, D. L., L. A. Blunt, B. K. See, J. A. Webster and K. J. Stout (2002). "The characterisation of grinding wheels using 3D surface measurement techniques." Journal of Materials Processing Technology 127(2): 234-237.
- Comaniciu, D. and P. Meer (2002). "Mean shift: a robust approach toward feature space analysis." Pattern Analysis and Machine Intelligence, IEEE Transactions on 24(5): 603-619.
- Cui, C., X. Xu, H. Huang, J. Hu, R. Ye, L. Zhou and C. Huang (2013). "Extraction of the grains topography from grinding wheels." Measurement 46(1): 484-490.
- Darafon, A., A. Warkentin and R. Bauer (2013). "Characterization of grinding wheel topography using a white chromatic sensor." International Journal of Machine Tools and Manufacture 70(0): 22-31.
- Doman, D. A., R. Bauer and A. Warkentin (2009). "Experimentally validated finite element model of the rubbing and ploughing phases in scratch tests." Proceedings of the Institution of Mechanical Engineers, Part B (Journal of Engineering Manufacture) 223(Copyright 2010, The Institution of Engineering and Technology): 1519-1527.
- Gonzalez, R. and R. Woods (2007). Digital Image Processing (3rd Edition), Prentice Hall.
- Inasaki, I. (1996). "Grinding Process Simulation Based on the Wheel Topography Measurement." CIRP Annals - Manufacturing Technology 45(1): 347-350.
- Lachance, S., A. Warkentin and R. Bauer (2003). "Development of an automated system for measuring grinding wheel wear flats." Journal of Manufacturing Systems 22(2): 130-135.
- Liu, Y., A. Warkentin, R. Bauer and Y. Gong (2013). "Investigation of different grain shapes and dressing to predict surface roughness in grinding using kinematic simulations." Precision Engineering 37(3): 758-764.
- Lonardo, P. M., H. Trumpold and L. De Chiffre (1996). "Progress in 3D Surface Microtopography Characterization." CIRP Annals - Manufacturing Technology 45(2): 589-598.

- Malkin S., G. C. (2008). Grinding Technology: Theory and Applications of Machining with Abrasives, Industrial Press, New York.
- Matsuno, Y., H. Yamada, M. Harada and A. Kobayashi (1975). "The microtopography of the grinding wheel surface with SEM." CIRP Annals - Manufacturing Technology 43(1): 237-242.
- Nguyen, A. T. and D. L. Butler (2008). "Correlation of grinding wheel topography and grinding performance: A study from a viewpoint of three-dimensional surface characterisation." Journal of Materials Processing Technology 208(1–3): 14-23.
- Roberto Rodríguez, M., D. Didier, T. Esley and H. S. Juan (2012). Image Segmentation Through an Iterative Algorithm of the Mean Shift.
- Verkerk, J. (1977). Final Report Concerning CIRP Cooperative Work on the Characterization of Grinding Wheel Topography, Lab. for Prod. Technol.
- Weingaertner, W. L. and A. Boaron (2012). "A method to determine the grinding wheel's topography based on acoustic emission." International Journal of Abrasive Technology 5(1): 17-32.
- Xie, J., F. Wei, J. H. Zheng, J. Tamaki and A. Kubo (2011). "3D laser investigation on micron-scale grain protrusion topography of truncated diamond grinding wheel for precision grinding performance." International Journal of Machine Tools and Manufacture 51(5): 411-419.
- Xie, J., J. Xu, Y. Tang and J. Tamaki (2008). "3D graphical evaluation of micron-scale protrusion topography of diamond grinding wheel." International Journal of Machine Tools and Manufacture 48(11): 1254-1260.
- Yan, L., Y. M. Rong, F. Jiang and Z. Zhou (2011). "Three-dimension surface characterization of grinding wheel using white light interferometer." The International Journal of Advanced Manufacturing Technology 55(1-4): 133-141.

CHAPTER 4

FORCE MODEL FOR IMPACT CUTTING GRINDING WITH A FLEXIBLE ROBOTIC TOOL HOLDER

Amir Masoud Tahvilian¹, Bruce Hazel², Farzad Rafieian¹, Zhaoheng Liu^{1*}, Henri Champlaud¹,

⁽¹⁾Department of Mechanical Engineering, École de technologie supérieure,
Montréal, Québec, H3C 1K3, Canada

⁽²⁾Expertise Robotique et civil, IREQ, Hydro-Québec's research institute
Varenes, Québec, J3X 1S1, Canada

This article is submitted to “Journal of Materials Processing Technology” in October 2014

Highlights

- Enhancements are made in determining the empirical coefficients of a semi-analytical grinding force model.
- The impact cutting regime in robotic grinding is identified at various grinding power levels.
- The variable cutting regime is used to determine the empirical coefficients in the model.
- An energy partition model and the friction-chip energy ratio are combined to determine new force model constants.
- The new constants confirmed the validity of the model for a wide range of grinding power levels.

4.1 Abstract

Traditionally, grinding is used as a finishing process in the manufacturing chain. However, in recent years, it has been also used to machine hard or brittle materials. Another application, developed by Hydro-Québec's research institute, IREQ, is robotic grinding for in situ

maintenance of large hydropower equipment. This high material removal rate grinding process is performed with a flexible robot as the tool holder. In a robotic grinding process, having an accurate model to predict the process force is crucial in order to achieve the desired material removal rate. This paper presents an experimental study that breaks new ground in determining the empirical parameters of an existing semi-analytical force model. An impact cutting behavior has been clearly observed at various grinding power levels both with high-speed video and force measuring equipment. The force model is based on an imaginary cutting notch acting to remove a chip at each wheel impact on the surface. The number of impacts per revolution of the grinding wheel is ascertained and used to determine the empirical coefficients of the force model. The previously determined energy partition ratios and correlated model are also used to determine the ratio of energy consumption through friction to that for chip formation. The empirical coefficients are then fine-tuned and updated using the energy partition model and friction-chip energy ratio for the process. The newly determined coefficients are validated through a series of tests and shown to be a good agreement with measured grinding forces. The results show that the new enhancements in determining model parameters can be used to better predict the process force, power and depth of cut in different cutting regimes and at various grinding power levels.

Keywords: Robotic grinding, force model, impact cutting, model identification

4.2 Introduction

Grinding is generally considered a finishing process with a very low material removal rate (MRR) and small depths of cut. However, there are applications in which grinding is primarily used to remove material in a process that is more like machining than finishing. This includes the grinding of very hard or brittle materials like super-alloys and ceramics. The special robotic grinding process studied here is another application of grinding primarily for machining purposes. Both a high MRR and high surface quality are normally required. A high MRR entails high grinding forces, which if not properly controlled may lead to inaccuracy, chatter, workpiece burn or other undesirable results.

A robotic process has been developed at Hydro-Québec's research institute, IREQ, for field repair jobs on hydropower equipment. A portable 6-degree-of-freedom robot manipulator named "SCOMPI" (Super-COMPact Ireq) was designed and built as the tool holder for use in such processes as welding, grinding, plasma gouging and hammer peening (Hazel et al., 2012a). The goal of the robotic grinding process is to achieve both a high MRR and a high-quality surface finish with great accuracy. The number of in situ repair jobs carried out with SCOMPI over the past 20 years has proven the robot's capabilities for hydropower equipment maintenance. However, since the robot is track-based and light-weight for maneuverability and portability, it is also very flexible. Given its low stiffness and the high force required for material removal in the specific grinding operations, a conventional position control strategy cannot be used to shape the part. Instead, the robot is coupled to an accurate measurement system and a controlled material removal rate (CMRR) strategy is employed to shape the part (Hazel et al., 2012a). The low stiffness of the robot also affects the dynamics of the grinding process. An impact cutting regime has been observed and documented through several methods. Care must be taken to include this impact cutting regime in the force model.

Grinding force prediction is essential to control the MRR. This is needed to maintain precision. A random number of grains are involved in the grinding removal action. This influences the force and makes it hard, if not impossible, to develop a fully analytical force model for grinding. For robotic grinding performed with a light, flexible tool holder such as that in this study, dynamic effects caused by low robot rigidity also add to the complexity. However, regardless of grinding regime and conditions, an accurate force model is necessary for process control. Grinding force greatly influences process quality. An accurate force model is even more important if it is used in the robot control process to achieve the desired MRR. Also, predicted forces are vital for thermal and vibration analysis, and for predicting potential workpiece burn or chatter.

4.3 Literature review

A grinding force model is an essential tool for process and quality control, particularly in industrial applications. It is difficult to specify accurately the physical interrelationships in grinding given the random, uneven distribution of the abrasive grains involved. Empirical models thus commonly come into play to predict the grinding force. (Tönshoff et al., 1992) reviewed basic empirical grinding force models developed before the 1990s. These models are primarily comprised of regression coefficients and process parameters, such as depth of cut, wheel speed, workpiece properties and wheel geometry. In an early study, (Malkin and Cook, 1971) experimentally verified that the grinding force increases with the growth of wear-flat areas on the wheel. They explained this behavior by separating the grinding force into cutting and sliding forces due to chip formation and rubbing, respectively. However, no force model formula was proposed at this point. (Werner, 1973) introduced a force model based on two elements. First, there is a stochastic distribution of cutting edges in the grinding process. Second, the theory of kinematics is involved in single-grain cutting, which is composed of chip formation and friction mechanisms. Soon after, (Snoeys et al., 1974) proposed a force model using their equivalent chip thickness model, which was based on the continuity equation. The models above are called “basic models”. Their main drawback is that they disregard the grinding time and coolant effect.

4.3.1 Empirical models

Normally for empirical models, parameters such as depth of cut, grinding wheel diameter, feed speed, wheel rotational speed and contact length are combined to predict the process force. Pure empirical models largely depend on extensive tests that are time-consuming and costly. Experimental observations under a wide range of process conditions are important in order to accurately characterize empirical models. (Fan and Miller, 2006) developed a grinding force model for segmental grinding. This type of grinding is performed with a segmented wheel, which leads to intermittent grinding since the wheel spacers do not come into contact with the workpiece. The authors divided each grinding force into a MRR-

dependent cutting component and a constant rubbing component. Empirical coefficients must be determined for every process condition, grinding wheel material and workpiece material. (Johnson et al., 2008) also established a grinding force model for face grinding. The authors found that the feed rate and inclination angle have the greatest influence on the force. They developed a polynomial equation with four process parameters for predicting the grinding forces. Through regression analysis, the constants in the force equation are determined for specific wheel and workpiece materials. They claim that the model is simple and fast for industrial applications, admitting its limited accuracy as a drawback. (Liu et al., 2008) used multivariate analysis to build an empirical grinding force model for an aerospace alloy. Like earlier models, the coefficients are determined experimentally and further test data is used to show a good correlation between the predicted results and actual measurements. (Tang et al., 2009) also mention that grinding forces are mainly comprised of two parts: chip formation force and sliding force. They showed that assuming a constant friction coefficient is a major drawback in existing models. The authors proposed a mathematical force model for surface grinding with a new formula for predicting the sliding force that included the effect of process parameters on the friction coefficient. A series of tests were carried out to validate the model proposed through agreement between measurements and results calculated based on the model.

4.3.2 Grit based models

Another approach for grinding force models extends the single-grit force formula to a more comprehensive force model. Although random distribution of grains is a basic assumption in such models, other assumptions are common for simplification, such as uniform grit shape with negative rake angle. (Hecker et al., 2007) evaluated a grinding force model assuming single-grit force and active-grain density as a function of the wheel. Grit force is calculated based on the mechanics of a single grain in contact using the workpiece's Brinell hardness, an undeformed chip thickness and the grain's effective diameter. Grains are all assumed to be spherical in shape. The authors then use the dynamic cutting edge density to predict total normal and tangential forces. The model calculation is validated and compared to test

measurement data. (Chang and Wang, 2008) developed a stochastic force model based on grinding conditions and a random grain distribution. A single-grit force, dependent upon the grinding geometry, is obtained. The total grinding force is then formulated by combining the single-grit forces and grit density function. The authors validated their model by a series of tests. (Park and Liang, 2008) also considered a similar single-grit interaction model to establish a comprehensive predictive model for micro-grinding. The authors considered in their model both a size effect, which is important in micro-machining, and a thermal effect. Analytical models for single-grit interaction, temperature and contact length are established and used to construct the force model. Tests performed to validate the model showed good agreement for small depths of cut but deviations were observed for larger depths of cut.

4.3.3 Semi-analytical models

Semi-analytical models place more emphasis on the process kinematics that govern the actual physical interaction between the grinding wheel and workpiece. Such models also normally include parameters that must be tuned experimentally. Once the necessary coefficients are determined empirically, the model is capable of predicting the force in the designated process range. (Patnaik Durgumahanti et al., 2010) developed a force model incorporating a variable friction coefficient and plowing force. The authors established cutting force equations in terms of process parameters and experimental constants. The force equation has three components: chip formation force, friction force and plowing force. Through a series of tests, coefficients are determined for chip formation and friction. Single-grit tests are performed to investigate the plowing force component. The predicted forces were in acceptable agreement with those obtained experimentally. (Mishra and Salonitis, 2013) proposed a multiple linear regression model for the grinding force ratio. Using test data, model coefficients were determined and the results were validated by the ratio of measured forces within an acceptable error. (Agarwal and Venkateswara Rao, 2013) stressed the importance of the chip thickness model, usually used as an input parameter for the force model. The authors established a force model for ceramic grinding using a new analytical undeformed chip thickness model. The chip thickness model was developed based on a random distribution of

grains and their geometry, and on the actual contact length in the contact zone. Results from the new model were shown to be in good agreement with the test data under a range of process conditions. (Yao et al., 2014) proposed a mathematical force model for three types of wheels used to grind an ultra-high-strength steel workpiece. The force model was again composed of chip formation and plowing parts. Five constants in the model were determined through the least-square method by using six sets of test data. The authors compare the grinding forces predicted from the model to those determined experimentally and found them to be in reasonable agreement. (Aslan and Budak, 2014) developed a semi-analytical force model for the grinding process based on a modified micro-milling analogy. The topography and grain geometry for two types of grinding wheels were measured using an optical measurement system. For each workpiece-wheel pair, model coefficients were then determined experimentally. Lastly, the authors validated the model by showing that predicted and experimentally measured force values were in good agreement.

Despite the many force models in the literature, developed for several types of grinding, few studies have been dedicated to robotic grinding, especially when performed with flexible robots. A simple, practical model for controlling the process then plays a crucial role. In this study, an existing force model for robotic grinding (Hazel et al., 2012b) is further analyzed and a new method is proposed for determining coefficients empirically. The micro-machining analogy and impact cutting kinematics are the main characteristics of this force model. Also, using the concept of energy partition, the empirical coefficients are determined more precisely. The number of impacts per turn of the grinding wheel, n_c , is a key parameter in determining coefficients. This parameter was set to one in earlier studies. The power, depth of cut and force values predicted by the model agreed closely with experimental force values measured during the process. The good correlation between the model and tests was found over a wide range of operating conditions and cutting regimes.

4.4 Grinding kinematics

This section introduces the kinematics of the impact cutting grinding process observed while performing traverse grinding with the robot. Conventional grinding force models are not applicable when a flexible robotic manipulator holds the grinder. This is due to much lower stiffness of the robotic manipulator compared to the heavy structure of conventional grinding machines. The robot arm is made of aluminum and its total weight is about 33 kg. A traverse surface grinding technique is employed with this flexible robot to perform high-MRR grinding. Figure 4-1a shows the grinding wheel performing a single pass. The feed direction is normal to the arc of the wheel in the contact zone. A thorough study on the material removal dynamics when grinding with this robot is reported in (Rafieian et al., 2014a), who detected a vibro-impact cutting behavior. At each impact, an idealized notch (see Figure 4-1b) is formed in the workpiece surface. In fact, the number of impacts per revolution of the wheel is not constant but varies as a function of the process parameters. It has been clearly shown that there are interruptions in cutting during the process when the wheel bounces off the workpiece. This can be explained by the low stiffness of the tool holder and high impact force in the direction normal to the workpiece surface.

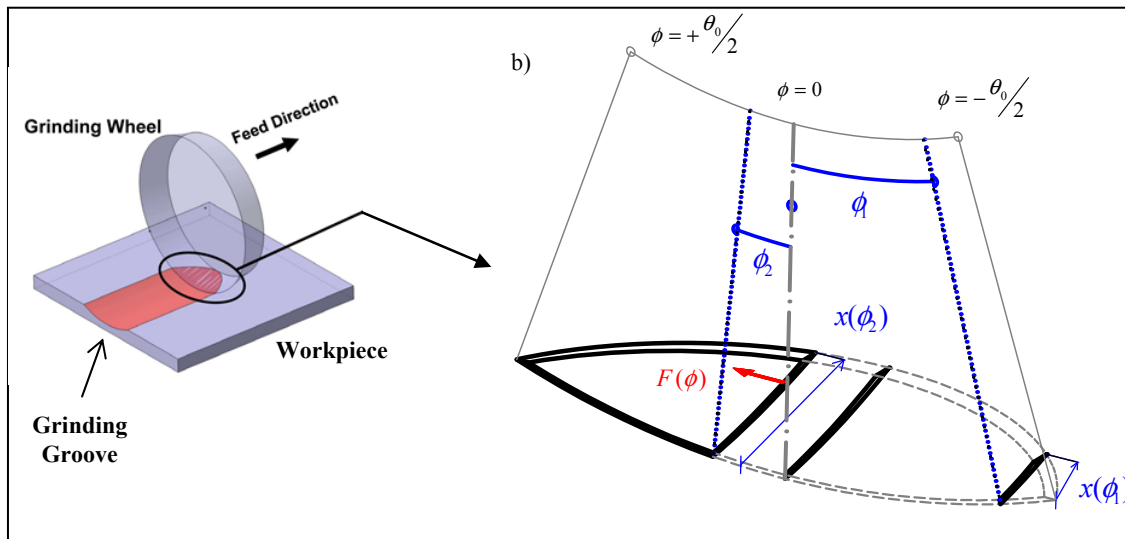


Figure 4-1 Grinding kinematics, (a) traverse grinding, (b) idealized notch

4.5 Process force model

Given the kinematics discussed above and the form of material removal, each abrasive grit acts as a micro-machining tool, removing a chip at each impact of the wheel. As commonly acknowledged, abrasive grits in a grinding wheel have several small cutting edges with negative rake angles. The cutting action of all abrasive grits involved during each impact is assumed to be similar to single-tooth milling. A force model for milling tools is thus used to calculate the instantaneous tangential cutting force in the process. The predicted force has two parts: the force exerted to overcome friction and the force to form a chip. The instantaneous tangential force can be calculated by (Altintas and Lee, 1998),

$$F_T(x) = \gamma(k_e + k_c \mathcal{E}(x)) \quad (4.1)$$

where k_e and k_c (identified empirically) are edge force and shear force coefficients respectively, γ is the grit width and $\mathcal{E}(x)$ is the undeformed chip thickness. The first term on the right-hand side of the force equation is the friction component and the second term is the chip formation component. Replacing grit width γ by the instantaneous undeformed chip width $x(\varphi)$, where φ is the immersion angle, and considering the total contact angle of θ_0 for one impact cut (see Figure 4-1b), the force equation can be rewritten as follows,

$$F_T(\varphi) = k_e x(\varphi) + k_c \int_0^{x(\varphi)} \mathcal{E}(x) dx = k_e x(\varphi) + k_c A(\varphi) \quad \left(-\frac{\theta_0}{2} < \varphi < \frac{\theta_0}{2}\right) \quad (4.2)$$

where $A(\varphi)$ is the instantaneous cross-sectional area of the undeformed chip. A comprehensive geometrical and force model for this process is established in (Hazel et al., 2012b). Replacing the instantaneous chip width and cross-section in Equation (4.2) gives,

$$F_T = k_e E \left(1 - \left| \frac{\varphi}{\sqrt{2h_0/R_0}} \right|^3 \right) + k_c \frac{v_f}{n_c N} \left(h_0 - \frac{R_0 \varphi^2}{2} \right) \quad (4.3)$$

where E is the wheel thickness, h_0 is the depth of cut, R_0 is the wheel radius, v_f is the feed speed, n_c is number of impacts per turn of the wheel and N is the wheel rotational speed (Hz). The depth of cut is also obtained based on geometrical calculations and the MRR (Z_w),

$$h_0 = [3Z_w / (4\sqrt{2R_0v_f})]^{2/3} \quad (4.4)$$

The average force can be calculated by integrating the instantaneous force over one turn of the wheel, considering the number of impacts per turn in the process,

$$\overline{F_T} = \frac{1}{2\pi} \int_0^{2\pi} F_T(\varphi) d\varphi = \frac{n_c}{2\pi} \int_{-\frac{\theta_0}{2}}^{\frac{\theta_0}{2}} F_T(\varphi) d\varphi = \frac{1}{2\pi R_0} (k_e n_c S_{chip} + k_c V_{chip}) \quad (4.5)$$

where S_{chip} is the undeformed chip's surface area and V_{chip} is the undeformed chip's volume. Writing the average force in terms of process parameters gives,

$$\overline{F_T} = \frac{1}{2\pi} \sqrt{\frac{h_0}{R_0}} \left[k_e n_c \frac{3}{\sqrt{2}} E + k_c \frac{v_f}{N} \frac{4\sqrt{2}}{3} h_0 \right] \quad (4.6)$$

Finally, multiplying the average tangential force (Equation (4.6)) by the peripheral wheel speed gives the process power,

$$P_M = \overline{F_T} \cdot 2\pi R N = k_e n_c E N \frac{3}{4} \left(\frac{12R_0 Z_w}{v_f} \right)^{1/3} + k_c Z_w \quad (4.7)$$

4.6 Test and measurements

A series of tests was conducted with SCOMPI, keeping the robot in its most stable configuration to minimize undesired dynamic and vibration behaviors (see Figure 4-2). All

tests were performed with a self-dressing depressed-center grinding wheel (Type 27 NORZON III) with zirconia alumina abrasive. The feed speed was set to a constant 80 mm/s. The wheel rotational speed was 6,000 rpm. Tests were run at four grinding power levels in the typical range for field tasks: 500, 1,000, 1,500 and 2,000 W. Single-groove tests were performed over a length of 250 mm. Tests at each power level were repeated four times to ensure consistent measurements. During the tests, the three component forces applied to the workpiece were recorded by a dynamometer. In addition, the instantaneous rotational speed of the wheel was measured using both optical and magnetic encoders. The control system of the robot also logged the grinding power consumed, feed speed and wheel displacement normal to the workpiece surface.

4.6.1 Test setup

A piezoelectric three-component dynamometer (Kistler Type 9255C) was used to measure the three orthogonal force components. In order to avoid measuring system disturbances, an ultra-rigid table was designed and built using a special concrete-and-steel structure whose first natural frequency is over 1.2 kHz. Both the dynamometer and workpiece were mounted on the table. A multichannel charge amplifier (Kistler Type 5070A) receives the charges from the four piezoelectric sensors of the dynamometer through a high-insulation cable and converts them to the proportional voltage levels for the DAQ input. Before the tests, the dynamometer was calibrated both by static and dynamic loading to ensure that the test setup was suitably designed and force measurements would be accurate. In static calibration tests, the robot is used to apply force on the dynamometer in three directions. Measurements from a load cell attached to the robot end effector and those from the dynamometer table were compared and found to be in very close agreement. Dynamic calibration tests were performed as free-rotation tests with an unbalanced disk installed on the grinder motor, which was mounted in various locations on the dynamometer table. Rotational speeds ranged from 1,000 to 6,000 rpm in increments of 1,000. Calibration test results showed that the measured force values correlated well with the theoretical unbalance force.

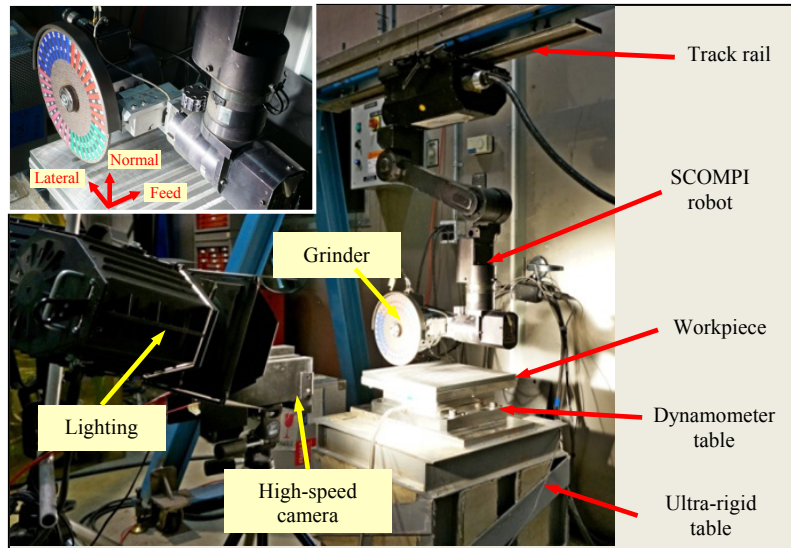


Figure 4-2 Test setup

The grinder was equipped with a Quantum Device QPhase optical encoder (Type QD145) and a Heidenhain modular magnetic encoder to measure the rotational speed of the grinder shaft. The optical encoder had TTL output and a resolution of 1,000 pulses per revolution (ppr), which a divider circuit then converted to 250 ppr. The digital encoder was also adjusted to 3,000 ppr. An IDT high-speed 1 megapixel digital camera (Y4 series) was used to capture high-frame-rate video of the process along the steadiest section in the grinding passes. Three 750-W halogen lamps (each connected to different phases of a 3-phase power supply) with 7-inch Fresnel lenses rated at 1,7000 lm ensured sufficient and continuous lighting of the workpiece-wheel contact zone while recording. Video capture of 1016 x 600 pixel images was at 6,000 fps with an exposure time of 40 μ s. Since the rotational speed of the grinding wheel was 6,000 rpm or 100 rps, each video frame corresponds to a 6-degree shift in the angle of the wheel. A number of lower-resolution frames at higher frame rates up to 25,000 fps were also captured to study the duration of contact during each impact. Each frame at this speed corresponds to a 1.44-degree rotation of the wheel.

The data acquisition system for angular sampling was set up based on the commercial software platform Measure Foundry[®]. A high-speed camera was also triggered and kept in sync with all recording channels. With the angular sampling method, signal values are recorded at specific position intervals in the grinding wheel rotation rather than at fixed time

intervals as is the case with time sampling methods. Recording occurs each time a pulse is received from the magnetic encoder. The time between recordings is also calculated using a 36-MHz internal clock on the data acquisition card. A Data Translation DT9836 Series module in a BNC box was used to capture the signals. This system is capable of simultaneously capturing analog and digital I/O, and has a counter/timer for encoders. Output signals were then converted to an ASCII text file and imported to Matlab for signal processing and plotting.

4.7 Results and discussion

4.7.1 Impact cutting regime

Observations with the high-speed camera confirmed that, rather than through continuous wheel-workpiece interaction, material is removed through an intermittent impact cutting regime. Normal- and high-speed video recordings during grinding are shown Figure 4-3 (online version only). In earlier studies with this robot, the number of impacts per turn of the wheel is assumed to be one (Rafieian et al., 2014b). In this study, careful review of high-speed video recordings under various operating conditions revealed that the number of impacts per turn varies according to the process power. The normal force signal from the dynamometer and drop in wheel rotational speed acquired by the encoders in this study also support the results obtained in an earlier study (Rafieian et al., 2014a).

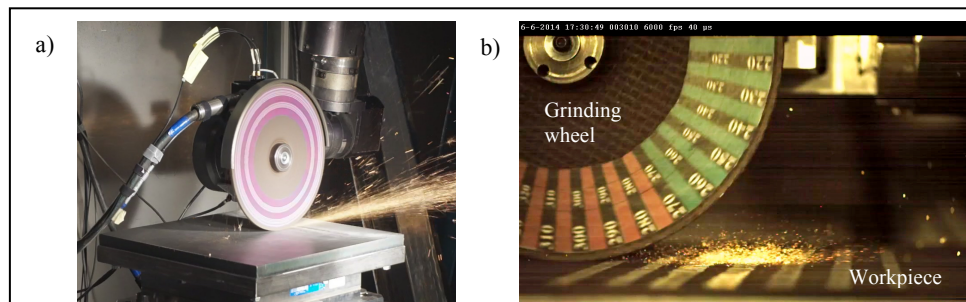


Figure 4-3 (a) Normal-speed video at 30 fps, (b) high-speed video at 6,000 fps, played at 30 fps (online version)

Figure 4-4a shows the angular speed of the grinder spindle recorded during a grinding test. Signal recording begins when the grinder starts to turn and the rotational speed ramps up from 0 to its 100-Hz nominal value in about 250 turns. After reaching the desired rotational speed, the robot starts to stretch out toward the workpiece in the normal direction to establish contact. This free-rotation phase last about 600 turns until contact is established and the power consumed reaches a predefined value. The robot then starts moving in the feed direction while controlling the normal position of the end effector to maintain the desired process power. When the groove is finished, the robot moves away from the workpiece and the grinder decelerate to zero rotational speed. Figure 4-4a also shows the grinding portion of measurements with an enlargement to the right. The drop in angular speed at the start of the pass is caused by the initial wheel-workpiece contact and continues until it is compensated by the control system. The rise in angular speed at the end of the pass is due to a similar effect as the load is removed at the end of the grinding pass when the wheel moves off the workpiece. Figure 4-4b shows the three components of the measured force and a zoom of the force and rotational speed signals during a 10-turn window under steady-state grinding conditions. In this region, one impact per turn of the wheel is clearly seen as a peak in the measured normal force and as a drop in measured rotational speed.

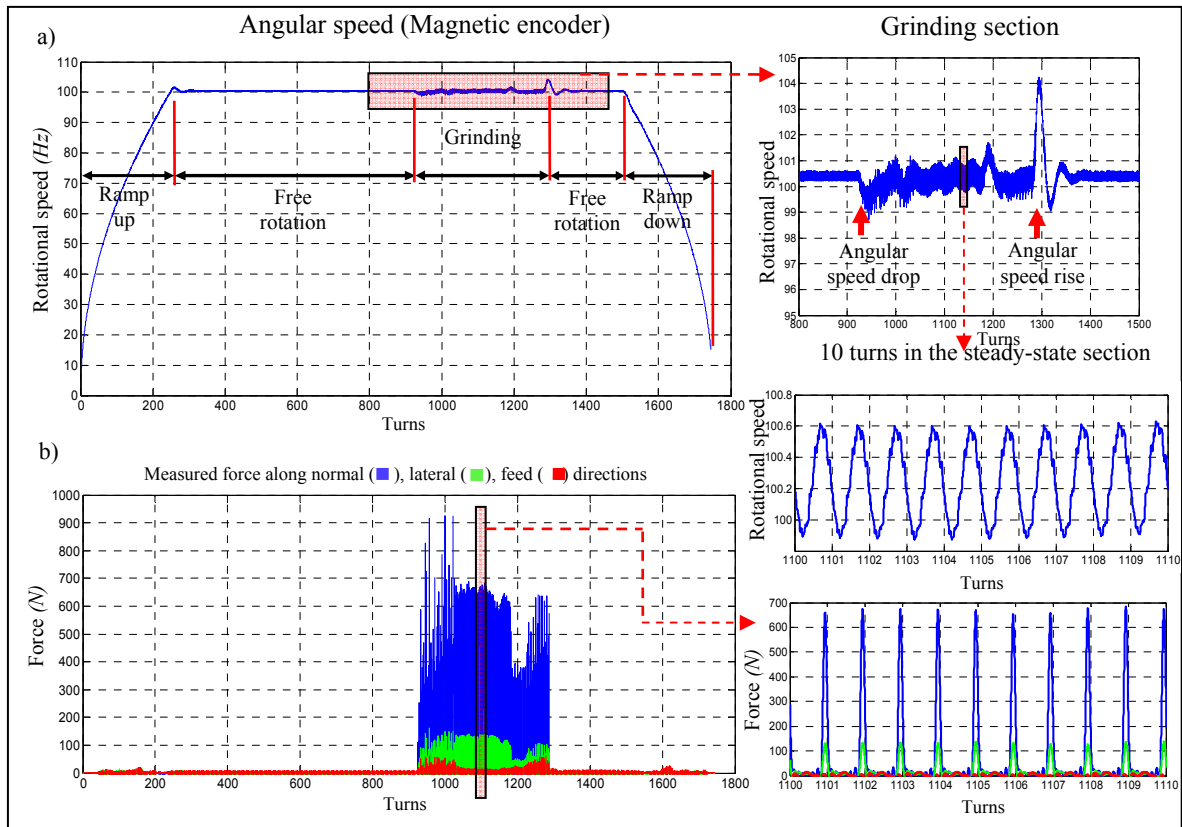


Figure 4-4 Angular speed and force measurements

Figure 4-5a and Figure 4-5b show separately the signals for the normal and lateral forces during the grinding pass. The data acquired for the initial and final sections of the pass are discarded given disturbances when grinding at the edges of the workpiece. The steadiest conditions are reached in the middle of the pass from 1030 to 1180 turns. The friction coefficient is introduced as the ratio of the average lateral force to normal force. Figure 4-5c shows the instantaneous value of the friction coefficient. Figure 4-5d shows an impact cutting map of the normal force signal. The vertical axis is the angular position of the wheel and the color map represents the normal force value relative to the moving average for the signal. In this figure, the position and number of impacts can be easily detected. One impact per turn almost in the same angular position (≈ 330 degrees) for this entire period is clearly observed in the steady-state section.

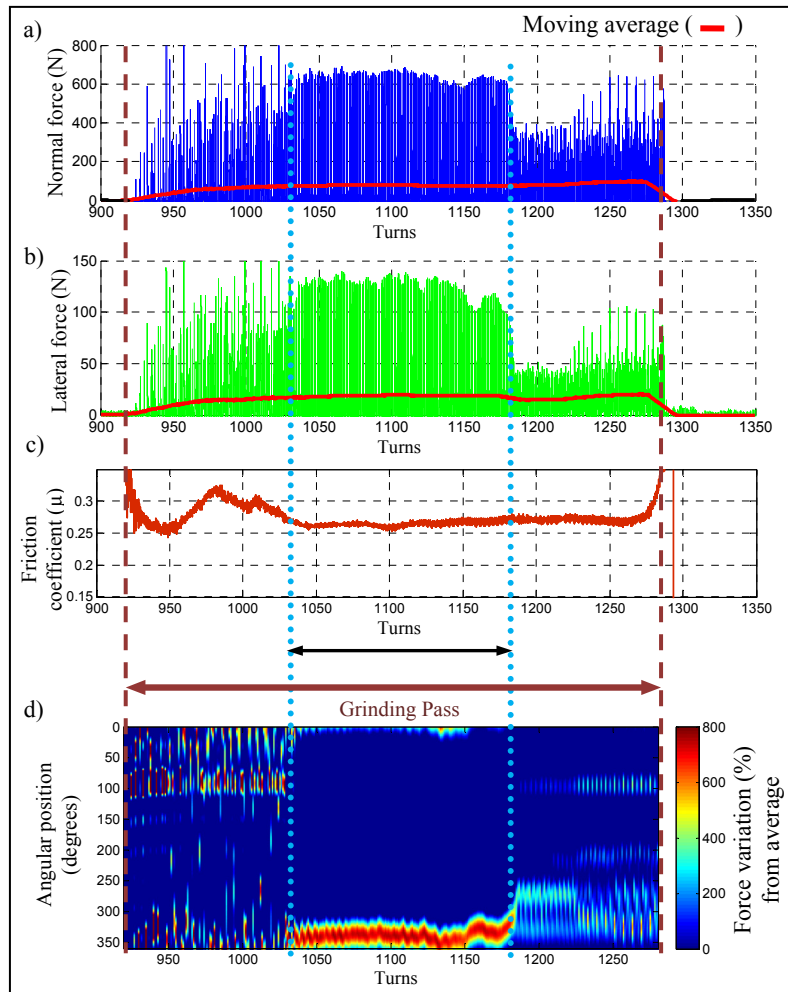


Figure 4-5 (a) Normal and (b) lateral force signal, (c) friction coefficient, (d) impact cutting map

As mentioned earlier, the tests and measurements above were repeated four times at each grinding power level. The impacting behavior was found to vary as a function of grinding power. Figure 4-6 summarizes the results for all four power levels, including an impact map of 50 turns of the wheel from the steady-state section and a zoomed 10-turn window for the normal force signal. The number of impacts during each turn appears in red above each turn in the force plots. Increasing the grinding power, which is directly correlated to the normal force applied by the robot to hold the end effector in position, clearly causes a higher number of impacts.

Figure 4-7 summarizes the probability of each number of impacts per turn for each grinding power level based on 50 turns in the steady-state section from all the tests. Note that at a very low grinding power level ($P = 500$ W), no contact occurs during more than 40% of the turns. This behavior can also be seen in the measured force signal in Figure 4-6a. In fact, the restoring force from the robot is so small that after an impact, the wheel sometimes spins for two entire revolutions before it again makes contact with the workpiece. Also note that one impact per turn is dominant in the range of 1,000 to 1,500 W. The angular position of impacts under these conditions (see Figure 4-6b and Figure 4-6c) is unchanged in the impact maps. If this behavior persisted, the wheel would wear unevenly and gradually become oval in shape. The short duration of grinding during these tests explains this. It has been observed in longer runs that the position of impact moves around the entire circumference of the wheel. For grinding at 2,000 W the dominant regime is 2 to 3 impacts per turn (Figure 4-6d). A weighted average is used for all power levels to find the number of impacts during each turn (n_c) to be used in the force model. These values are 0.75, 1.29, 1.56 and 2.25 impacts per turn for grinding power levels of 500, 1,000, 1,500 and 2,000 W, respectively.

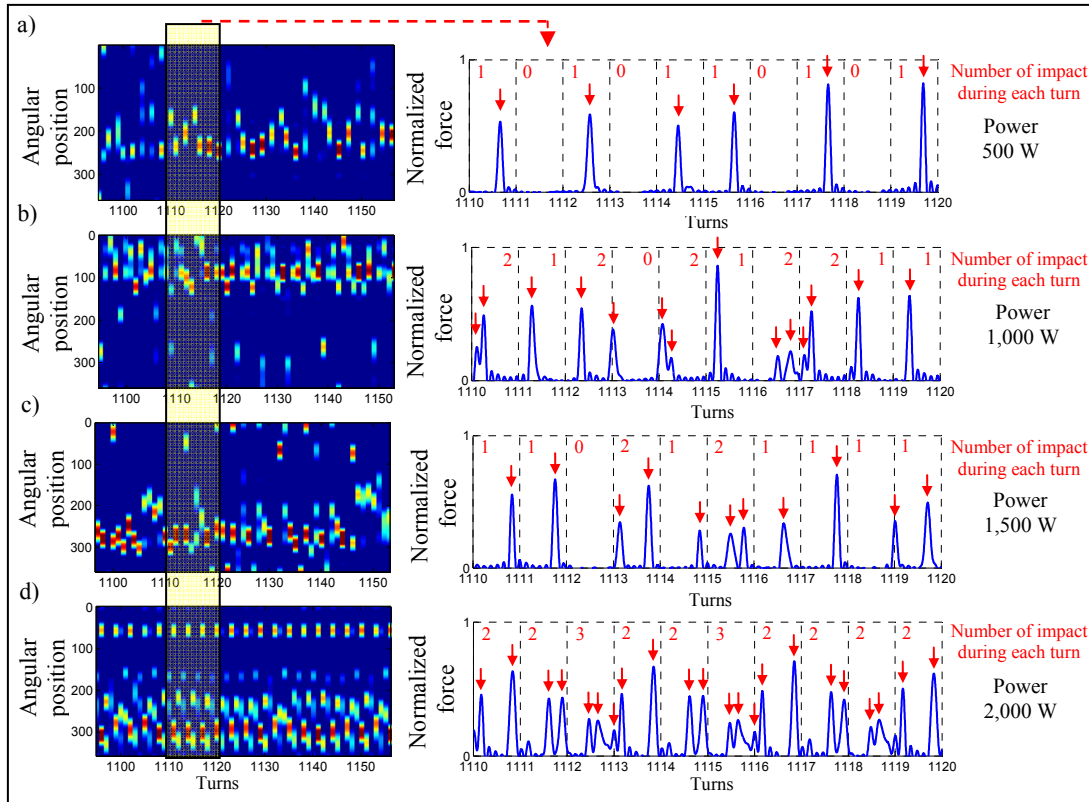


Figure 4-6 Impact regime at different power levels, (a) $P = 500 \text{ W}$, (b) $P = 1,000 \text{ W}$, (c) $P = 1,500 \text{ W}$, (d) $P = 2,000 \text{ W}$

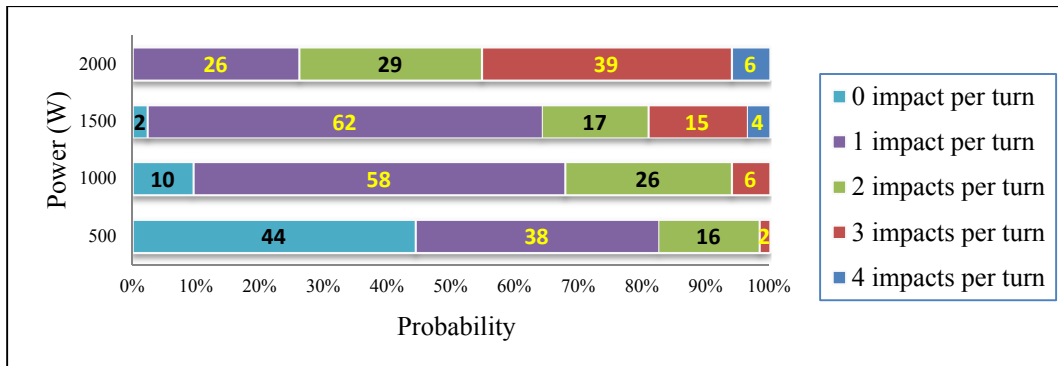


Figure 4-7 Probability of number of impacts per turn

4.7.2 Profilometer scans

All grinding grooves (see Figure 4-1) were scanned using an AltiSurf 530 profilometer with a chromatic confocal probe (CL4), which has axial accuracy of $0.4 \mu\text{m}$ and a resolution of

0.075 μm . A general scan of the grooves was performed with measuring steps of 10 μm in the lateral direction and 250 μm in the feed direction. A high-resolution scan with 10- μm steps in both directions in the steady-state region was also carried out to have more accurate measurements for analysis. Figure 4-8 shows the measuring equipment as well as a photo of an actual groove and its scan. Before further analysis of the scan measurements, a preprocessing step is performed on the data for each groove. First, linear interpolation and a median filter are applied to remove outliers that deviate by more than 4 sigma from the mean. Second, an unskew process is applied to correct the workpiece deflection that occurs after grinding. This is necessary to avoid misleading results in calculating the depth and volume of cut. A mask is thus applied over the measured region to exclude the sides of the groove so only the relatively flat regions at the top and bottom of the groove remain. These are used to detect the curvature of the plate surface in both the feed and lateral directions. Then, the correction algorithm is applied using linear regression to the entire measured region, including the groove.

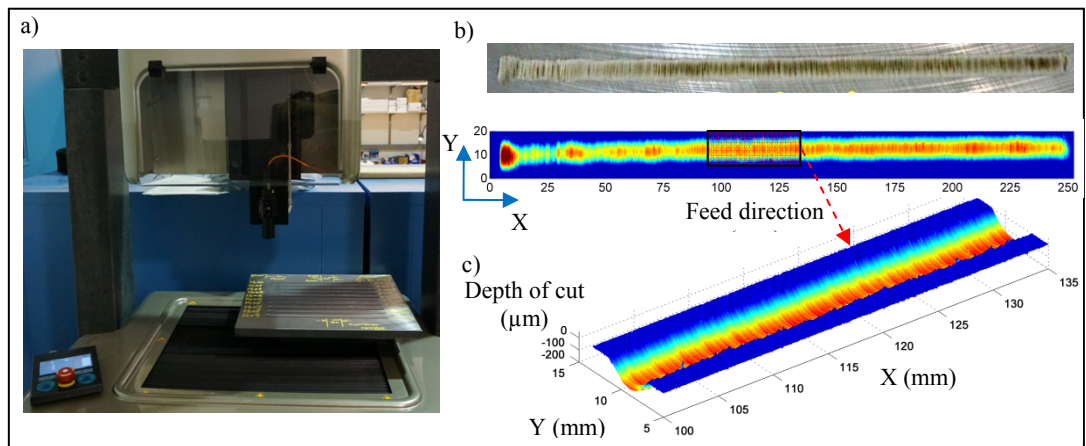


Figure 4-8 (a) Scanning the grooves, (b) top view of a groove (image and measured), (c) sample 3D view

For each section of the groove (see Figure 4-9a), the lowest point is taken to calculate depth of cut. The cross-sectional area is also calculated at each measuring step, which gives the instantaneous MRR when multiplied by the feed speed. Figure 4-9b and Figure 4-9c show

the MRR obtained and the depth of cut along the groove in the feed direction for different power levels.

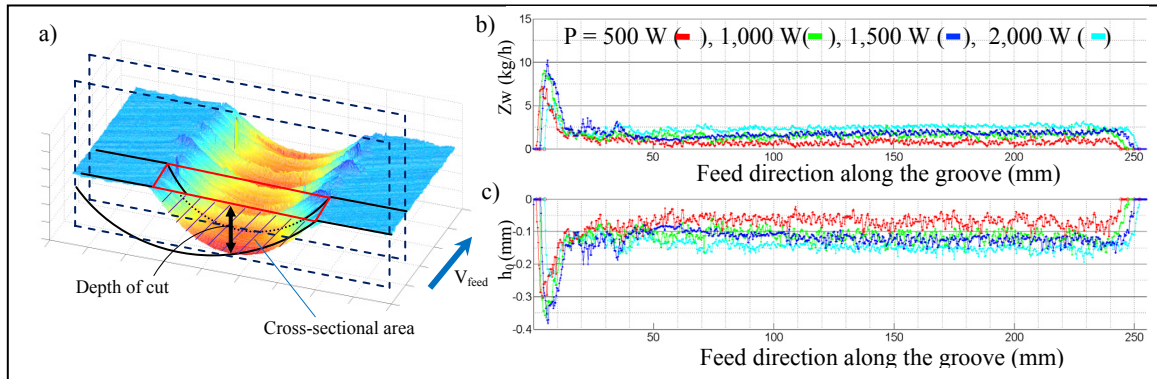


Figure 4-9 (a) Analysis of scanned groove, (b) instantaneous MRR, (c) depth of cut

4.8 Determination of model coefficients

In the tests, the data needed to determine model coefficients is acquired from three different sources: logged data from the robot controller, recorded signals from the data acquisition system and groove scan measurements. The logged data, recorded at constant time intervals, includes grinder power consumption, and the position and velocity of the robot in the feed and normal directions. The grinder used in this study is built around an electric three-phase synchronous permanent-magnet motor. The mechanical power delivered at the spindle is accurately monitored, considering all the effects of motor losses and temperature on motor power. Motor losses include drag and friction in the bearings, power to drive the fan, and power dissipation as core losses in the stator iron armature. The permanent-magnet electric grinder was tested on a dynamometer bench in an IREQ lab in order to ensure an accurate estimate of the mechanical power delivered at the spindle. The results showed that the estimated power differs by less than 2% from the actual mechanical power. The data acquisition system, as mentioned earlier, gathers the angular velocity from encoders and the three components of force from dynamometer measurements, recorded at different angular positions of the grinder shaft. The data obtained from the scanned grooves includes the depth of cut and the MRR at constant feed interval positions. For instantaneous determination purposes, all three sources are synchronized with respect to the feed position along the

groove. Ten data samples in the stable range of the groove are thus used as input to determine the empirical coefficients in the force model. A sample of the synchronized data is given in Figure 4-10.

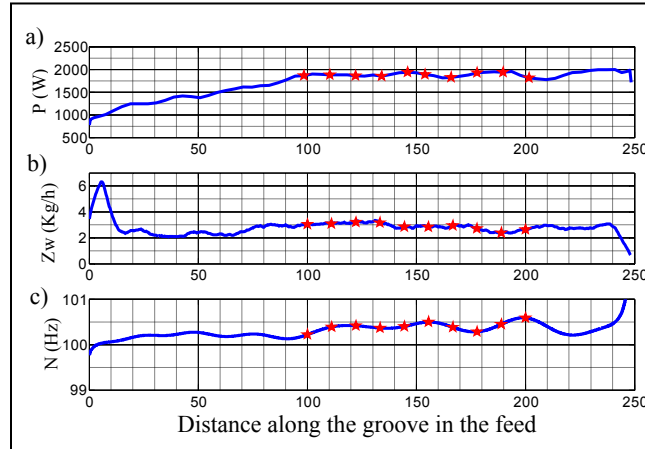


Figure 4-10 Synchronized data for (a) power consumption measured from robot controller, (b) MRR from groove scan data, (c) angular speed from DAQ

To determine the model parameters, a cost function is defined as the root-mean-square error of the predicted and measured powers at these 10 sample data points summed for all 16 tests,

$$C_{power} = \sum_{j=1}^{16} \left(\frac{\sqrt{\sum_{i=1}^{10} [P_m - P_M]^2 / 10}}{\bar{P}_M} \right) \quad (4.8)$$

where P_m and P_M are the instantaneous measured and predicted powers. Measured power P_m is obtained from the robot controller, which is synchronized by the scanned groove position. Predicted power P_M is calculated with Equation (4.7) using the instantaneous MRR, wheel rotational speed and weighted average number of impacts n_c . The cost function error is plotted in Figure 4-11. The error in the acceptable region, the white area inside the iso-line with the smallest value, is 9.3%. Any pair of points for edge and force constants k_e and k_c on the line in Figure 4-11 predicts acceptable process power. However, it may be assumed that only one pair of k_e and k_c coefficients optimally model the process. A further constraint on

the correct ratio of friction and chip formation powers will thus be considered. In the following section, an energy partition model is used for final selection of these empirical coefficients.

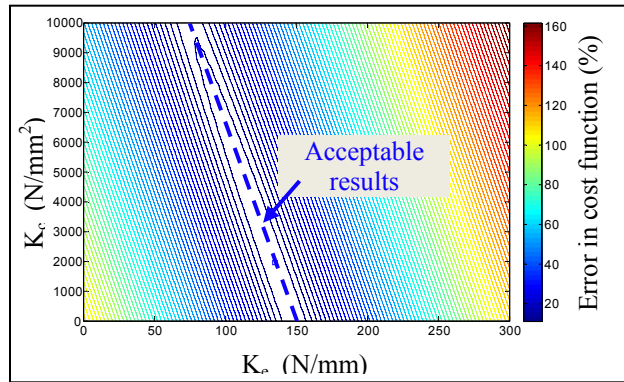


Figure 4-11 Error in cost function

4.8.1 Friction and chip formation power

Minimizing the cost function in Equation (4.8) for grinding power does not bring into play all of the physical parameters of the process. A friction-chip energy ratio check is thus performed in this section. It is widely acknowledged that almost all the energy consumed in grinding is converted into heat (Malkin S., 2008). There are four main sources of heat dissipation in a grinding process: the workpiece, grinding wheel, chips, and coolant. An energy partition is defined as the ratio of the amount of energy entering the workpiece to the total consumed energy.

$$\mathcal{E} = \frac{\text{energy entering the workpiece}}{\text{total consumed energy}} \quad (4.9)$$

In order to further constrain the acceptable region for the empirical coefficients, an energy partition model of the process developed earlier (Tahvilian et al., 2013) is used here. The model was developed considering the vibro-impact nature of the steady-state regime in this

robotic grinding process. The model for the energy partition is based on the chip and friction fractions of consumed power,

$$\varepsilon = \frac{\alpha P_{friction} + \beta P_{chip}}{P_M} \quad (4.10)$$

where $P_{friction}$ is the power consumed to overcome friction in the process, P_{chip} is the power consumed to form the chip, α and β are constants, and P_M is the total consumed power. The last parameter can be formulated as follows according to the force model,

$$P_M = P_{friction} + P_{chip} = k_e SN + k_c Z_w \quad (4.11)$$

Through a series of tests, the energy partition ratio and the value $\alpha = 0.76$ and variable β (see Table 4.1) based on the grinding power were validated by (Tahvilian et al., 2013).

Table 4.1 β values and energy partition versus grinding power

Power	1000	1250	1500	1750	2000
β	0.27	0.17	0.09	0.05	0.03
ε	0.62	0.55	0.48	0.43	0.40

The values of edge and cutting coefficients k_e and k_c that best predict the friction and chip power are thus chosen using Equation (4.10) and Equation (4.11). The values $k_e = 75$ N/mm and $k_c = 10,020$ N/mm² give the correct ratio of powers. Figure 4-12 plots the results for data points acquired at various power levels using Equation (4.7) with the empirical coefficients so determined. The test data at different power levels is plotted in different colors (see figure legend). This plot shows four markers, corresponding to each MRR value on the horizontal axis. One is the test measurement mentioned earlier and the other three are total predicted power P_M , friction power $P_{friction}$ and chip formation power P_{chip} . As specified in Equation (4.11), the total predicted power from the model is the sum of the friction and chip formation

power. These two parts of the power are equivalent to the first and second terms on right-hand side of Equation (4.7). The chip formation power is a linear function of MRR Z_w . The friction power increases with the cube root of MRR Z_w , while the number of impact n_c changes the multiplier factor. The friction power thus shifts when the cutting regime is altered due to a change in grinding power. The effect of the number of impacts in different cutting regimes can be seen in the friction power in Figure 4-12.

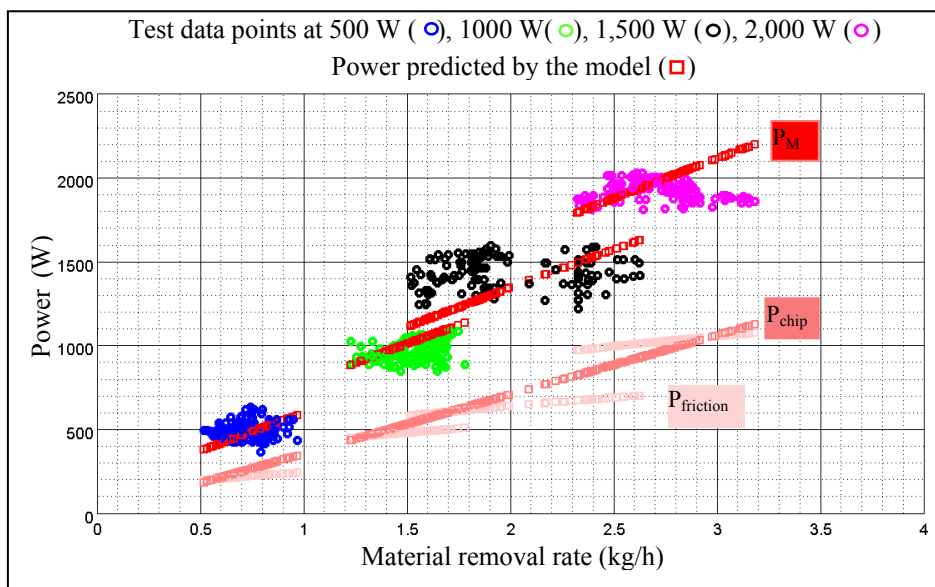


Figure 4-12 Predicted and measured grinding power

4.8.2 Force and depth of cut

The depth of cut and average normal force can also be predicted by the model. Figure 4-13 compares the measured and predicted depths of cut in the stable region of the groove. The depth of cut is predicted using Equation (4.4) and the measured value is from the corresponding groove scan data. A good correlation can be seen at all four grinding power levels. The results obtained by selecting a constant cutting regime (i.e., $n_c = 1$) are also shown in Figure 4-13.

The predicted average normal force Equation (4.6) was also validated with the dynamometer force measurement. The average force ratio of 0.26 found from the test data was used to

calculate the normal force in the model. Similarly, results are plotted considering variable and constant cutting regimes. It is clear that the multi-impact model can better predict the process over a wider operating range.

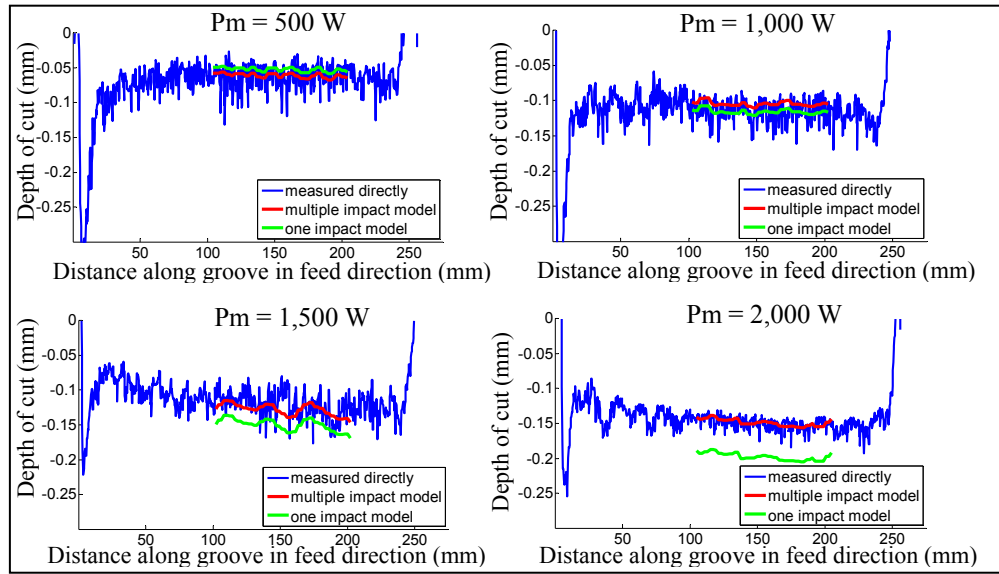


Figure 4-13 Measured and predicted depth of cut at different power levels

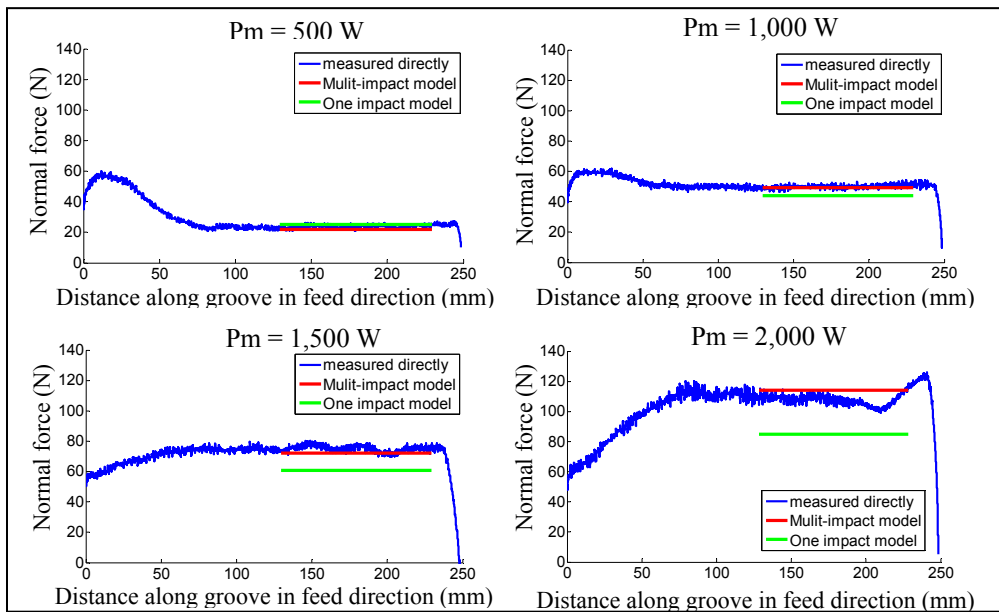


Figure 4-14 Measured and predicted average force at different power levels

4.9 Conclusion

New enhancements have been introduced to determine the parameters of an existing semi-analytical force model for a flexible robotic grinding process. The force model was originally developed based on the micro-machining analogy assuming an impact cutting behavior where an idealized notch is formed at each impact. The empirical coefficients in the model were determined through tests considering the observed cutting regime. The impact cutting action was verified by high-speed video observations, the angular speed from an encoder and the force signal from a dynamometer. The number of impacts per turn at different grinding power levels was determined by carefully studying force signal impact maps. This varying cutting regime, the synchronized MRR, measured grinding power and the angular speed of the wheel were used to determine an acceptable boundary for empirical coefficients in the force model. An energy partition model of the process, developed earlier, was used to determine the portions of power consumed to overcome friction and to form chips. Through optimization, the coefficients that satisfy the friction-chip energy ratio are then determined. The two new enhancements made to the force model—consideration of the variable cutting regime and use of an energy partition to determine optimal parameters—lead to a model that is valid over a wide range of grinding power levels. Predicted grinding power, depth of cut and average normal force were in excellent agreement with test measurements at different power levels. This work will make it possible to improve robotic process control by using the optimally determined force model parameters. Currently, the impact regime is detected through the force signal. Though impacts are very clear in the normal force measurements, it is infeasible to use a dynamometer in the field. Detection of the impact regime outside the lab should thus rely solely on the angular speed measured by the encoder installed in the grinder. This requires very sophisticated signal filtering appropriately applied since it is sometimes very difficult to distinguish the speed drop caused by an impact from the background noise in the signal. This work is part of a broader effort to establish a micro-scale FE model of chip formation in the cutting process performed with the flexible SCOMPI robot.

4.10 Acknowledgments

Financial support from the Natural Sciences and Engineering Research Council of Canada (NSERC) through a collaborative research and development (CRD) grant is gratefully acknowledged. The authors also extend their thanks to the SCOMPI team at Hydro-Québec's research institute for their great technical support.

4.11 References

- Agarwal, S. and P. Venkateswara Rao (2013). "Predictive modeling of force and power based on a new analytical undeformed chip thickness model in ceramic grinding." International Journal of Machine Tools and Manufacture 65(0): 68-78.
- Altintas, Y. and P. Lee (1998). "Mechanics and Dynamics of Ball End Milling." Journal of Manufacturing Science and Engineering 120(4): 684-692.
- Aslan, D. and E. Budak (2014). "Semi-analytical Force Model for Grinding Operations." Procedia CIRP 14(0): 7-12.
- Chang, H.-C. and J. J. J. Wang (2008). "A stochastic grinding force model considering random grit distribution." International Journal of Machine Tools and Manufacture 48(12-13): 1335-1344.
- Fan, X. and M. H. Miller (2006). "FORCE ANALYSIS FOR GRINDING WITH SEGMENTAL WHEELS." Machining Science and Technology 10(4): 435-455.
- Hazel, B., J. Côté, Y. Laroche and P. Mongenot (2012). "Field repair and construction of large hydropower equipment with a portable robot." Journal of Field Robotics 29(1): 102-122.
- Hazel, B., J. Côté, Y. Laroche and P. Mongenot (2012). "A portable, multiprocess, track-based robot for in situ work on hydropower equipment." Journal of Field Robotics 29(1): 69-101.
- Hecker, R., S. Liang, X. Wu, P. Xia and D. Jin (2007). "Grinding force and power modeling based on chip thickness analysis." The International Journal of Advanced Manufacturing Technology 33(5-6): 449-459.
- Johnson, E. C., L. Rui, A. J. Shih and H. Hanna (2008). Design of experiments based force modeling of the face grinding process. Transactions of the North American Manufacturing Research Institution of SME.

- Liu, Q., X. Chen, Y. Wang and N. Gindy (2008). "Empirical modelling of grinding force based on multivariate analysis." Journal of Materials Processing Technology 203(1-3): 420-430.
- Malkin, S. and N. H. Cook (1971). "The Wear of Grinding Wheels: Part 1—Attritious Wear." Journal of Manufacturing Science and Engineering 93(4): 1120-1128.
- Malkin S., G. C. (2008). Grinding Technology: Theory and Applications of Machining with Abrasives, Industrial Press, New York.
- Mishra, V. K. and K. Salonitis (2013). "Empirical Estimation of Grinding Specific Forces and Energy Based on a Modified Werner Grinding Model." Procedia CIRP 8(0): 287-292.
- Park, H. W. and S. Y. Liang (2008). "Force modeling of micro-grinding incorporating crystallographic effects." International Journal of Machine Tools and Manufacture 48(15): 1658-1667.
- Patnaik Durgumahanti, U. S., V. Singh and P. Venkateswara Rao (2010). "A New Model for Grinding Force Prediction and Analysis." International Journal of Machine Tools and Manufacture 50(3): 231-240.
- Rafieian, F., F. Girardin, Z. Liu, M. Thomas and B. Hazel (2014). "Angular analysis of the cyclic impacting oscillations in a robotic grinding process." Mechanical Systems and Signal Processing 44(1-2): 160-176.
- Rafieian, F., B. Hazel and Z. Liu (2014). "Vibro-impact dynamics of material removal in a robotic grinding process." The International Journal of Advanced Manufacturing Technology 73(5-8): 949-972.
- Snoeys, R., J. Peters and A. Decneut (1974). "SIGNIFICANCE OF CHIP THICKNESS IN GRINDING." Ann CIRP 23(2): 227-237.
- Tahvilian, A. M., Z. Liu, H. Champlaud and B. Hazel (2013). "Experimental and finite element analysis of temperature and energy partition to the workpiece while grinding with a flexible robot." Journal of Materials Processing Technology 213(12): 2292-2303.
- Tang, J., J. Du and Y. Chen (2009). "Modeling and experimental study of grinding forces in surface grinding." Journal of Materials Processing Technology 209(6): 2847-2854.
- Tönshoff, H. K., J. Peters, I. Inasaki and T. Paul (1992). "Modelling and Simulation of Grinding Processes." CIRP Annals - Manufacturing Technology 41(2): 677-688.
- Werner, G. n. (1973). Konzept und technologische Grundlagen zur adaptiven Prozessoptimierung des Aussenrundschleifens.

Yao, C., T. Wang, W. Xiao, X. Huang and J. Ren (2014). "Experimental study on grinding force and grinding temperature of Aermet 100 steel in surface grinding." Journal of Materials Processing Technology 214(11): 2191-2199.

CONCLUSION

This research combined experimental and numerical investigations to improve fundamental knowledge useful in modeling flexible robotic grinding. On the numerical side, finite element simulation and empirical modeling were the principal axes of the study. These methods, combined with comprehensive test data, provided a better understanding of material removal in robotic grinding and the consequences of the process involved. Results for the models developed can be used to improve process efficiency or perform a sensitivity analysis of the process. The main characteristic of the simulations, i.e., low stiffness of the robot structure and the resulting impact cutting regime, were addressed. Critical aspects of the process and considerations needed to model it were introduced. The major findings and contributions of this research pertain to robotic grinding processes performed by light, flexible robots and are summarized below.

In the first article, local chip thickness in material removal and dynamic effects in the process are combined to propose an appropriate heat source for FE simulation of flexible robotic grinding. A FE solver was used for the simulations. The solver code was enhanced by general-purpose computing on graphics processing units (GPGPU), which significantly reduced the solution time. Given the sequential impact cutting observed in the process, the boundary conditions in the model were adjusted to predict accurately the temperature distribution and energy partition in the workpiece. If this dynamic effect is ignored and average parameters are used in the numerical model, workpiece temperatures may be underestimated. Test measurements of temperature agreed closely with predicted values. An empirical model for energy partition in flexible robotic grinding was also introduced based on grinding power. This model is an important part of grinding process investigations as it provides insight into the amount of energy that enters into the workpiece.

In the second article, grinding wheel topography was determined for two commonly used types of grinding wheels: disk and cup. A laser confocal microscope was used to obtain both an optical image and the topography of the region of interest on the wheel surface. The

optical image was then used to detect the grains and distinguish them from the bonding material through image processing techniques. The mask generated was applied to the topography to extract the geometry of individual grains. A vertex normal method was introduced to analyze the grain faces and select those in the cutting direction. Yaw and rake angles for the grain attack face were then extracted. Wheel topography was characterized for low, medium and high grinding power levels. The results indicated that the yaw angle has a uniform distribution and the rake angle a normal distribution. The yaw angle distribution remains unchanged at different power levels; whereas, the mean rake angle in its normal distribution tends to have higher negative values at lower grinding power levels. This confirmed that when grinding at lower power levels, the grains become duller and process efficiency will consequently drop. Statistical data for grain face angles, grain width and protrusion are necessary for micro-scale simulation of grinding. This is an ongoing part of the research project.

In the third article, new enhancements in the empirical determination of parameters were introduced for an existing semi-analytical force model of the grinding process. An accurate force model plays an important role in the robot control strategy, and thus helps achieve higher precision and better surface quality in the process. The force model is based essentially on the micro-machining analogy and an impact cutting regime governing the process. In earlier studies on flexible robotic grinding, a constant single impact per turn of the wheel during the material removal process was assumed in determining the empirical constants in the force model. The impact cutting regime was observed, however, to vary at different grinding power levels. The measured normal force signal during the process proved to be the clearest sign of impacts and was used to identify the number of impacts under different operating conditions. High-speed video recordings during grinding with the robot under study also confirmed the impact cutting regime. The grooves, left after a single-pass grinding test, were also scanned to determine the instantaneous depth of cut and material removal rate (MRR). The impact cutting regime detected, synchronized MRR, measured grinding power and angular speed of the grinder were then used to obtain the empirical coefficients within an acceptable range. Lastly, the energy partition of the process from the

first part of study was used to determine the empirical coefficients. The new model has a force prediction capability over a wider range of power levels for the robotic grinding process studied. The force model was validated through comparison of predicted and measured average normal force and depth of cut.

RECOMENDATIONS

Some directions for future research related to this study are proposed below.

The thermal FE model developed in the first part of this study pertains to grinding with a disk wheel. However, the heat source function and other boundary conditions can be modified and extended to other types of wheels. The energy partition ratio is also an important aspect to be investigated with a cup wheel, a type of wheel commonly used in grinding with SCOMPI. Although thorough testing and numerical simulations are needed, a foundation will thus be built for further investigation on other aspects of the process.

The grinding wheel grain shapes obtained from the second part of this study can be used for micro-scale simulation of the robotic grinding process studied. The procedure proposed is to conduct several single-grain cutting FE simulations. Then, an overall model for material removal will be built to predict the total force based on the wheel topography. Some preliminary results have already been obtained in this direction and have been published in a conference paper (see Appendix I). Note that the results presented in that paper were prior to the topography study in second article so comparisons in it only pertain to changes in grain shape, specifically rake angle. Further investigations are needed, however, to make sure that the correct material behavior and friction models are employed in the overall model. The material model for micro-scale FE simulation has now been extracted from the literature available on the subject. Comprehensive experimental investigations may be needed to completely understand material behavior under such loading conditions. Since using the appropriate material model in numerical simulation is critical in order to obtain correct results, any effort deployed to better understand material behavior will be beneficial.

In the third part of this study, empirical coefficients in the force model were determined based on the experimentally observed impact cutting regime in the process. Impacts were detected from the normal force signal measured by a dynamometer, which is inapplicable outside a laboratory environment. In practical use of this robot, such high-precision force

measurements are not feasible. The only signature of impacts available is thus the drop in angular speed measured by grinder encoders. Further work is required focusing on appropriate signal processing and filtering to detect the impact regime based on angular speed.

APPENDIX I

Influences of Grit Shape and Cutting Edge on Material Removal Mechanism of a Single Abrasive in Flexible Robotic Grinding

Amir Masoud Tahvilian¹, Zhaoheng Liu^{1*}, Henri Champlaud¹, Bruce Hazel²

⁽¹⁾Department of Mechanical Engineering, École de technologie supérieure,
Montréal, Québec, *H3C 1K3*, Canada

⁽²⁾Expertise Robotique et civil, IREQ, Hydro-Québec's research institute
Varenes, Québec, *J3X 1S1*, Canada

This article is published in "Proceeding of the ASME 2013, International Mechanical Engineering Congress & Exposition, IMECE2013", November 15-21, 2013, San Diego, California, USA

A I-1 Abstract

A flexible robotic grinding system has been used for in situ maintenance of large hydro turbine runners by Hydro-Quebec. Field trials for more than 20 years have proven the reliability and efficiency of the technology for hydropower equipment maintenance and repair. This portable robot named SCOMPI, is developed by IREQ, Research Institute of Hydro-Quebec and can perform high material removal rate grinding on hardly accessible areas of turbine runner blades. Due to the light weight and low rigidity of the robot, traditional position control of conventional grinding is not applicable in this process. Instead a hybrid force/position controller is employed to ensure the accuracy of the predefined material removal rate. Therefore, having a good force model for a specific removal rate is a prerequisite for controlling the grinding task. Understanding the grinding process as the cutting action of several single grits participating in the material removal process provides an insight to predict the needed forces.

This paper presents an investigation of the effects of grits shape on cutting forces in single abrasive cutting mechanism during high removal rate grinding by SCOMPI robot. A three-dimensional finite element model is developed to simulate the chip formation process with different grit shapes. Thermal results from our previous study of temperature distribution in the contact zone for this special robotic grinding are imposed to the undeformed chips. Then, Johnson-Cook plasticity model is employed to investigate effects of hardening and thermal softening of work piece material in cutting forces. It is also found that, rake angle and cutting edges of the grit can have significant effects on the cutting and normal forces.

A I-2 Introduction

Finite element analysis has been an effective numerical tool since mid 1960's to predict and understand processes behaviors and has played an important role for improving the processes. Grinding wheels are composed of several small abrasives, which are responsible of removing the material from the work piece surface. Finite element simulation of grinding process is more complex compared to other machining processes due to the arbitrary grit contact positioning relative to the work piece surface in grinding. Distinct characteristics and kinematics in flexible robotic grinding process is also adding to this complexity because of lower rigidity of system compared to conventional grinding machines. Among all the metal cutting processes, orthogonal cutting is the mostly studied one meanwhile, similar to the single grit cutting action in grinding process. Early experimental observations by (Kita et al., 1978) showed that a negative rake angle tool can approximately represent the mechanism of material removal by an abrasive grain in grinding. Although extensive studies, both numerically and analytically, have been done on simulation and understanding of the orthogonal cutting process, less attempts have been performed on material removal simulations of single abrasive grit with a negative rake angle.

Therefore, the aim of current study is to build a Finite Element (FE) model capable of capturing the effect of grit shape especially in the negative rake angle domain with work

hardening and thermal softening effects for micro-cutting simulation of single abrasive grit. The geometry and other kinematics of these grits are based on the flexible robotic grinding process under study. The results will be used to develop a force model of the process which will be integrated in the robotic system in a future work.

A I-3 Background

(Shaw, 1993) highlighted the major difference of grinding and orthogonal cutting in their energy distribution among the components and uncontrolled geometry of cutting edge in grinding. Other than the main difference of having a negative rake angle in a single abrasive material removal in grinding compared to positive rake angle in an orthogonal cutting model, the basic ideas of modeling chip formation are somehow the same. However, other assumptions and approximations should be considered for modeling the grinding processes. Some of these conditions that can be seen in almost all of single abrasive simulations are as follows: each single grain moves in a complete circular path; the work piece is stationary during a single contact; no simultaneous contact grains occur at the same time. Simulating the chip formation phenomenon is an important issue in finite element modeling of metal cutting processes and has been under investigation in recent decades. In the process, as the tool advanced into the work piece, material ahead of the tool tip needs to be pushed away to let the chip and the new surface form. This involves in the simulation separation of finite element mesh during the solution. Basically, in order to handle material separation mechanism in finite element models, three techniques are commonly used as node separation criteria (geometrical or physical), adaptive re-meshing with ALE formulation and element deletion with damage law. Either one or a combination of the techniques can be implemented to form the chip in metal cutting simulations.

Node separation criteria are based on splitting of nodes on a pre-defined path when a specified condition is satisfied. This method can be divided into two main categories, geometrical separation criteria and physical separation criteria. Adaptive re-meshing is a local or global re-meshing of the work piece with respect to an activation criterion, i.e. a limit

for change of angles in elements or a constant time interval. This method is usually very costly in terms of computation time. In element deletion, a damage law is utilized to control the elements in the distorted zones. Each of elements that reach the limit is deleted from the mesh. This method is used in Lagrangian or ALE formulation to model the most realistic material behavior in chip formation.

A I-4 Literature review

(Shih, 1995) used a plane strain FE model to investigate the effect of rake face angle in the orthogonal cutting process. Geometrical separation criterion and updated Lagrangian formulation is used in order to obtain cutting force and residual stresses. Although acceptable results are obtained, the author highlighted the lack of damage modeling in his simulation as the reason of unrealistic chip and free surface boundary compared to the experimental data. (Mamalis et al., 2001) also used geometrical chip separation criterion for orthogonal cutting simulation. When the distance between the nodes and tool tip reaches a critical limit, separation occurs. (Ohbuchi and Obikawa, 2003) was among the first who tried to simulate the grinding mechanism by introducing a FE model of orthogonal cutting with a large negative angle using updated Lagrangian formulation. A predefined separation line is used to allow chip formation in the simulation. Each node on the separation path is divided into two nodes when the tool tip has reached the node. The authors found that cutting speed and grinding parameters like depth of cut have great influences on the chip formation process. Therefore, a cutting speed adjusted with the grain rake angle for efficient material removal is suggested.

The main disadvantages of a geometric criterion are the absence of physical interpretation and need of pre-defined separation path. In addition, there is no relevant magnitude for the critical distance, and it should be determined by try and error for each cutting condition. Small magnitude of distance will cause excessive mesh distortion around the tool tip and large values causes the chip to separate too early and consequently, this results in a crack in the work piece, ahead of the tool tip. As for physical criteria, physical parameters like stress,

effective plastic strain or energy density are used as the separation threshold. Although use of physical criteria for chip separation is more reasonable, there still exists an open issue for determining the critical value of the physical parameter. This method has been used by several researchers for separation threshold (Huang and Black, 1996; Lin and Lin, 1992).

(Yen et al., 2004) used updated Lagrangian formulation with continuous re-meshing to simulate the chip formation mechanism for orthogonal cutting. A better way to handle the mechanism of chip formation is to implement Arbitrary Lagrangian Eulerian (ALE) formulation to avoid frequent re-meshing in the whole model. However, local adaptive re-meshing around the tool tip is still necessary and a pre-defined chip geometry should also be defined as an input of FE model to simulate the chip formation (Ozel and Zeren, 2005).

(J. Zouhar, 2008) used Lagrangian formulation with damage law to investigate the effect of rake angle and tool nose radius in cutting force, stress and temperature. As the aim of their study is the simulation of orthogonal cutting process, only rake angles of -10, 0 and 10 are studied. (Guo and Yen, 2004) implemented damage law to study discontinuous chip formation in hard machining. The authors found a good correlation between simulated chips and experimental results. In another study, (Doman et al., 2009a) presented a three dimensional FE model to investigate the sliding and ploughing phases of material removal in grinding. Comparison of the normal and tangential forces between FE results and experimental measurement in scratch tests were carried out to validate the proposed model. (T.T.Opoz, 2010) also considered a negative rake angle tool in orthogonal cutting to represent the single grit cutting in grinding. 2D and 3D models are simulated by ALE formulation and adaptive re-meshing technique to avoid element distortion. (Xun and Opoz, 2010) used a single grit approach to simulate surface generation in grinding process by finite element analyses. In their study, three stages of grinding i.e. rubbing, ploughing and cutting, are discussed with effect of different friction coefficients. In each condition, force variation during the grit movement is derived. Although there is no experiment verification in this study, effect of friction in ploughing stage is clearly shown. (Hoffmeister and Gerdes, 2011) used a quick-stop device to measure the cutting force of a single grit with rake angle of -45 degree. The authors also developed a FE model with Lagrangian formulation and damage

law to simulate the chip formation, stress and heat distribution in the workpiece material during the cutting process. A good agreement is reported between the simulation results and quick-stop experiments.

In another recent study, (Anderson et al., 2011; 2012) performed experimental and numerical analyses to investigate and compare effect of two different geometries for the cutting grain. A so-called hybrid Euler-Lagrange numerical implementation is used in their work to prevent the need of adaptive re-meshing and reduce computation time. The authors carried out a comprehensive study on the forces due to the single grain action, showing effects of cutting speed and depth of cut. It is noted that prior studies are limited to spherical and truncated cone with a fixed rake angle and very low depth of cut suitable for conventional grinding processes.

In the present study, emphasis is oriented on variation of grain geometry in term of changing the rake angle and depths of cut in the range of the robotic grinding process under study. Effects of cutting speed and thermal softening is also considered to achieve more realistic behavior and cutting forces in FE modeling.

A I-5 Robotic grinding by SCOMPI robot

This work is intended to study a grinding process performed by a robotic system. The robot named SCOMPI is developed by research Institute of Hydro-Quebec to handle the entire repair procedure for cracks and defects of turbine blades and other components. Because of its versatility of performance, a light weight and flexible robot was needed to meet the requirements of on-site maintenance of hydro turbine blades. More detail information on this robot can be found in (Hazel et al., 2012b). Because of its light weight design, the robot has low stiffness structure for the task force and unwanted vibration and deformation of arms are likely to happen during the processes. Observations of the grinding process performed by this robot revealed that in steady-state condition, material removal occurs only once per turn of grinding wheel and for the rest of the revolution the wheel detach from the work piece

surface. This special behavior, captured by high speed camera in our lab (See Figure A I-1), is called impact-cutting and should be distinguished from chatter in conventional machining. Grinding with SCOMPI robot is categorized as high removal rate traverse surface grinding. This process is performed with a self-dressing aluminum oxide wheel with diameter of 200 mm and rotation speed of 6000 RPM. Accordingly, linear peripheral speed of grains at each impact during material removal process is 62.8 m/s. Normally feed speed and depth are preferably kept at maximum stable values which are 80 mm/s for feed speed and 0.1~0.3 mm for depth of cut. Based on the mentioned impact-cutting behavior, kinematics of un-cut chip at each revolution of wheel can be extracted.

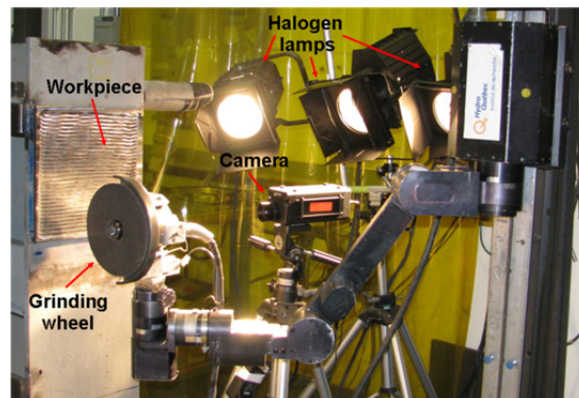


Figure A I-1 High speed camera setup used for observation of impact cutting

Figure A I-2 shows this undeformed chip and how it is sectioned in several small strips which are individually considered as the uncut-chip removed by a single grain. For a groove depth of 0.2 mm and feed speed of 80 mm/s in the process at each impact of the grinding wheel these uncut-chip sections may have thicknesses between 10 to 50 micrometers, hereafter referred to as the depth of cut in the simulations.

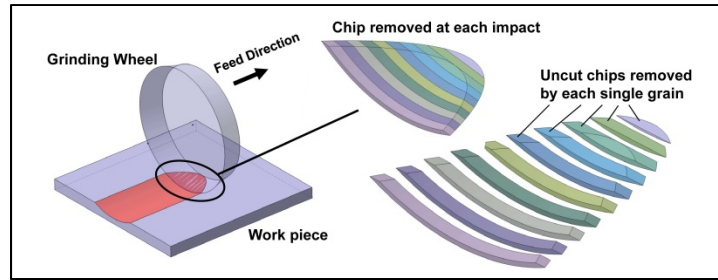


Figure A I-2 Kinematics of uncut chips at each impact

Figure A I-3.a shows the scan of grinding wheel surface. The scan is performed at 10 micrometers steps in both x and y directions to get an insight of rake angles in the cutting grains. This scan is cut to several random sections for better clarification in Figure A I-3.b.

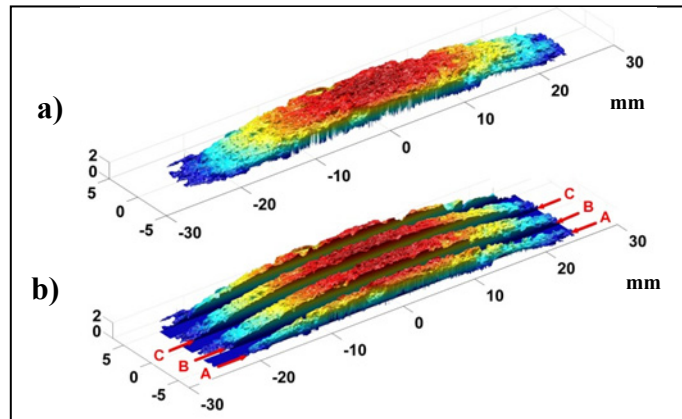


Figure A I-3 Surface of wheel a) 3D scan,
b) Separated sections of wheel scan

Figure A I-4 shows the straightened profile of the random sections from Fig.3.b in 2D. It is clearly seen that the cutting edges consist of a wide range of negative rake angles.

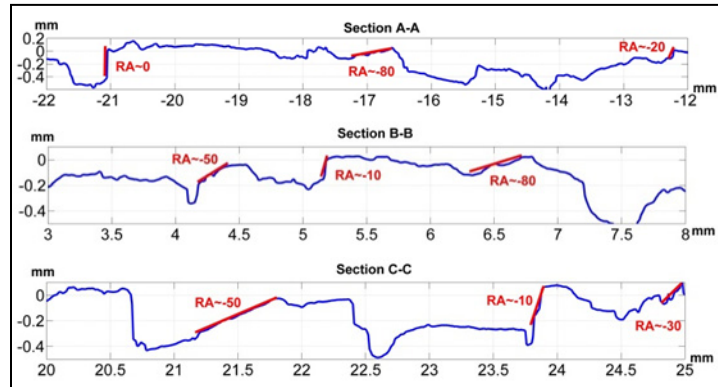


Figure A I-4 2D profiles and rake angles

A I-6 Finite element model

A three-dimensional thermo-mechanical finite element model is developed in Ls-Dyna explicit code to perform the chip formation simulations. Due to the computation cost and need of very fine mesh, a very small section of work piece is modeled for the simulation. The length of the model is considered sufficiently long to obtain the steady-state cutting and normal forces. A coupled thermal-structure simulation is performed to account for the heat generation in elements due to mechanical work. The small portion model of a single grit cut in simulation cannot represent the total heat generation during the process due to cutting action by lots of grits in real process. Therefore, temperature data obtained from our previous work (Tahvilian, 2012) is mapped to the FE model as initial temperature to include the real effect of thermal softening in material behavior. The bottom of the work piece is fully constrained and it is ensured that boundary condition does not affect the chip formation zone. For this reason, height of the finite element mesh is properly varied based on the simulated depth of cut in the model to have very low strains near the bottom of work piece. Mesh study is performed to find the optimal mesh size in terms of computation time and accuracy. Element size range between 2 to 6 micrometers is used for the chip formation zone and the mesh gradually becomes coarser toward the depth of work piece to reduce the total number of elements in the model. Figure A I-5 shows a schematic of FE model used in this study.

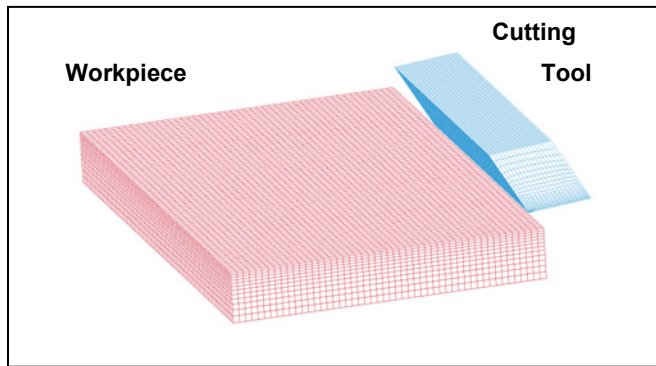


Figure A I-5 Finite element mesh

The grain is modeled with rigid shell elements having the same mesh density of work piece mesh to maintain good contact interface compatibility. Grain width size is 0.5 mm based on the type of the grinding wheel used in the process. According to the surface scans of wheel (See Figure A I-4) a range of 10 to -70 degree is chosen for the rake angle of the tool. Depth of cut is also varied between 5 to 50 micrometers based on the uncut-chip section thicknesses. The standard penalty formulation contact computes the contact force as function of the material data and detected penetration of slave nodes in master segment. In this study, the more recent contact formulation, called Segment-based penalty (Livermore, 2006), is used. This method improves the contact stability especially between parts with sharp edges by considering both sides of contact (slave/master) as segments, rather than nodes, to calculate the penetration distance. Results in our chip formation simulations showed a good ability of this formulation to maintain the contact between sharp edges of grain and workpiece.

A I-7 Material model

Material behavior in metal cutting is known to be one of the dilemmas in simulation procedure. Due to the existence of excessive strain, large strain rate and high temperature, material does not behave as common elastic-plastic behavior. There are numbers of constitutive models in the literature used by researchers to determine the visco-plastic material flow in machining processes. (Fang, 2005b) compared 18 engineering materials and concluded that strain rate hardening has the least effect on flow stress compared to the other

terms, i.e. strain hardening and thermal softening. A full list of common constitutive material models for flow stress can be found in (Grzesik, 2008). A frequently used material model for chip formation simulations in the literature is the one by (Johnson and Cook, 1985b). Having been proven to be reliable for metal cutting simulations, this material model is also used in this study. J-C model predicts the flow stress by the following equation,

$$\sigma = [A + B(\varepsilon^p)^n] [1 + c \ln(\frac{\dot{\varepsilon}^p}{\dot{\varepsilon}_0})] [1 - (\frac{T - T_{room}}{T_{melt} - T_{room}})^m] \quad (A I.1)$$

where, ε^p is the effective plastic strain, $\dot{\varepsilon}^p$ is the effective plastic strain rate, $\dot{\varepsilon}_0$ is the reference strain rate, T_{melt} is the melting point of material, T_{room} is the ambient temperature and A, B, c, m, n are the material's constants.

The Johnson-Cook damage law is also used in chip formation. Similar to J-C material model strain, strain rates and temperature are taken into account in this damage model. For each element, damage is defined by,

$$D = \sum \frac{\Delta \dot{\varepsilon}^p}{\dot{\varepsilon}^{pf}} \quad (A I.2)$$

where, $\Delta \dot{\varepsilon}^p$ is the increment of equivalent plastic strain during each time step in each element, and $\dot{\varepsilon}^{pf}$ is the equivalent failure plastic strain under the same condition of temperature, strain rate and stress. Whenever D reaches 1 failure is occurred in the element and that element is removed from the mesh. The empirical Johnson-Cook failure plastic strain is given by,

$$\varepsilon^f = [D_1 + D_2 \exp(D_3 \sigma^*)] [1 + D_4 \ln(\frac{\dot{\varepsilon}^p}{\dot{\varepsilon}_0})] [1 + D_5 (\frac{T - T_{room}}{T_{melt} - T_{room}})] \quad (A I.3)$$

where D_1, \dots, D_5 are material constants, σ^* is the ratio of pressure divided by effective stress and the rest of parameters are identical as defined in J-C material model. Several studies can be found in the domain of orthogonal cutting simulation in which J-C damage model (Ng and Aspinwall, 2002; Pantalé et al., 2004) were used. The constants for constitutive material and damage model are shown below.

Table A I.1 J-C material constants for
AISI 1045 (Jaspers and Dautzenberg, 2002)

A (MPa)	B(MPa)	n	c	m
553	600	0.234	0.0134	1

Table A I.2 J-C damage constants for
AISI 1045 (Vaziri et al., 2010)

D1	D2	D3	D4	D5
0.05	4.22	-2.73	0.0018	0.55

A I-8 Results and discussion

FE analyses are performed at the mentioned range of depths of cut (10 to 50 micrometers) and rake angles (10 to -70 degree). The outcomes and conclusion are applicable in the domain of single grain cutting with negative rake angle. Figure A I-6 shows the Von Mises stresses in the work piece during chip formation with depth of cut of 20 micrometers and rake angle of -10 and -50 degree. As expected at -10 degree the chip is formed completely whereas in -50 degree the work piece material is mostly pushed away and grit is more rubbing on the surface.

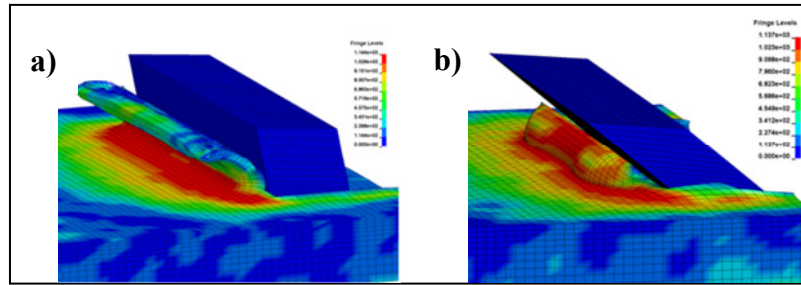


Figure A I-6 Von-Mises stresses, depth of cut = $20 \mu m$
 a) rake angle = -10 degree, b) rake angle = -50 degree

Based on the simulations, it is found that increase of cutting speed reduces the normal force, whereas cutting forces are not much affected by the speed variation. Also, effect of cutting speed on the normal force is more significant in cutting with high negative rake angles. The results showed that the reduction of cutting force due to increase of wheel speed is valid to a certain speed and after that the forces remain constant. The same trend can be observed in the experimental force measurements of single grit cutting action by (Patnaik Durgumahanti et al., 2010). Figure A I-7 shows a sample variation of normal force presented versus cutting speed for the depth of cut of 20 micrometer in different rake angles.

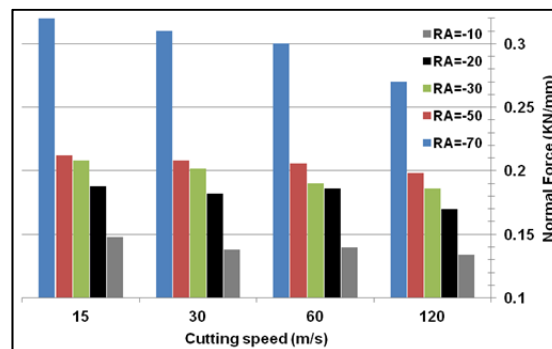


Figure A I-7 Normal force versus cutting speed

As mentioned earlier thermal softening effect can play an important role in softening the work piece material and reduce the cutting forces. In order to add the effect of high local heat in the chip formation zone, an initial temperature is added to the work piece element to investigate this effect in the material during the chip formation. Figure A I-8 shows the cutting force during the simulation at initial temperatures of 20, 500 and 800 degrees of

Celsius. As expected, the cutting force is decreased with increase of temperature. The noise of the force in this graph is normal and it is due to the element deletion in the FE model. The temperature distribution in the chip formation zone is also shown in Figure A I-9.

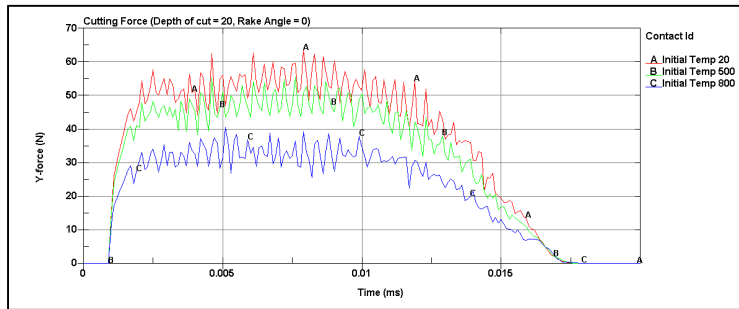


Figure A I-8 Effect of initial temperature on cutting force

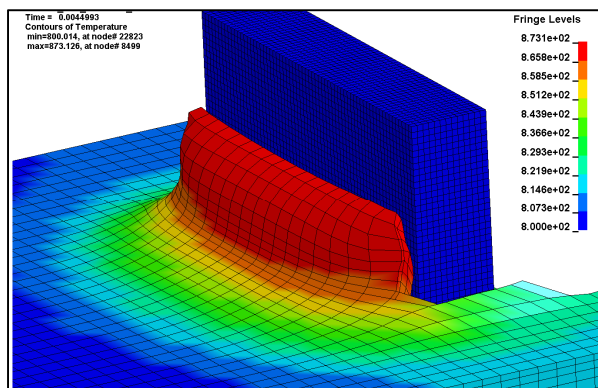


Figure A I-9 Temperature contour during the chip formation

According to our previous study (Tahvilian, 2012), an initial temperature of 500 degree of Celsius is mapped to FE mesh prior to chip formation simulations. This temperature is determined based on the groove depth and feed speed of grinding wheel. Applying such an initial temperature in the model leads to an average value of 9% reduction in cutting forces compared to the simulation that the temperature in elements is just due to mechanical work converted into heat. Figure A I-10 and Figure A I-11 summarize the normal and cutting forces for the range of the simulations in this study versus the depth of cut with different rake angles.

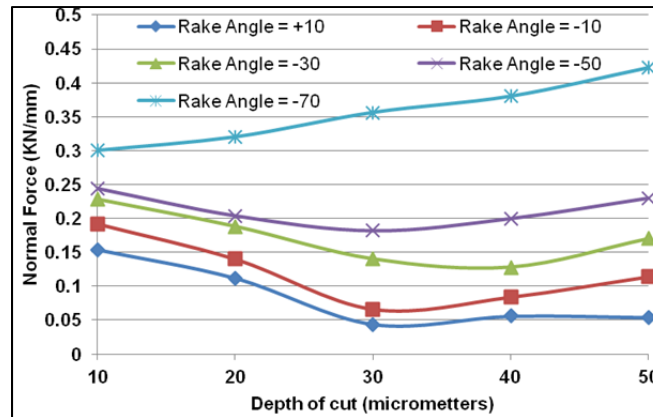


Figure A I-10 Normal force versus depth of cut and rake angle

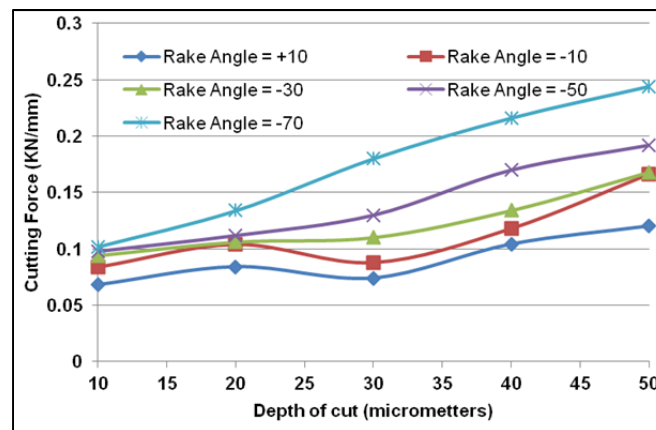


Figure A I-11 Cutting force versus depth of cut and rake angle

It is interesting to notice that except the rake angle of -70 all the normal forces decrease until the depth of cut reaches 30 micrometers and then increase with the depth of cut. This can be explained by the size effect phenomena, where lower depths of cut results in higher forces although not much material is removed from the surface. In this case, most of the force contributed to rubbing and plowing phases of the process rather than chip formation.

The same trend is seen in the force ratio in Figure A I-12. The force ratio starts to increase at depths of cut lower than 30. This size effect phenomena of increase in force or specific energy of grinding processes is also reported in previous studies (Hwang et al., 1999).

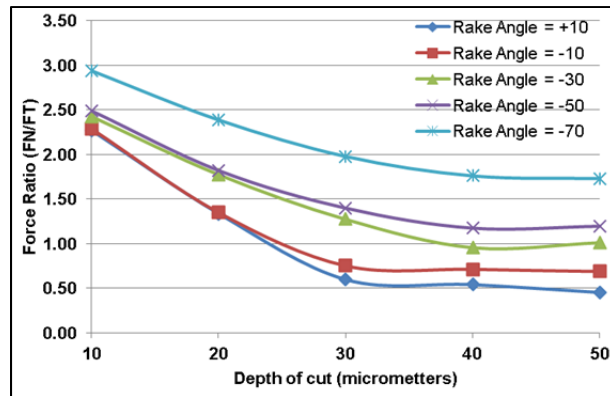


Figure A I-12 Force ratio versus depth of cut and rake angle

A I-9 Conclusion

Single grain cutting action in a robotic grinding process is simulated using dynamic finite element method in this work. The developed model is capable of handling the necessary conditions and characteristics of cutting action in highly negative rake angle grits. It is found that in the range of wheel speeds and the negative rake angles applicable to the process under study, cutting forces are not much affected by variation of speed, where a slight decrease in normal forces are observed. The results showed a decrease of approximately 9% in cutting forces due to thermal softening effects by applying the elevated initial temperature in the model. The influences of cutting depth and rake angles on normal and cutting forces caused by the thermal softening effect due to the high local heat generation in the process and strain rates are also demonstrated. A size effect behavior is seen for depths of cut lower than 30 micrometers where the normal force increase by reducing the chip thickness. The developed FE model is intended to be used to improve the force model for the robotic grinding process and its control strategy. In future work FE results will be combined according to the distribution of grits and their shapes in the grinding wheel surface. Then, a numerical model for the instantaneous cutting force in the process will be developed. The final results will be compared to experimental measured force during the impact-cutting.

A I-10 Acknowledgments

The authors would like to thank the SCOMPI team at Research Institute of Hydro-Quebec (IREQ). The authors would also like to express their gratitude to the Natural Sciences and Engineering Research Council of Canada (NSERC) and to Hydro-Québec for their research grants and support.

A I-11 References

- Anderson, D., A. Warkentin et R. Bauer. 2011. « Experimental and numerical investigations of single abrasive-grain cutting ». *International Journal of Machine Tools and Manufacture*, vol. 51, n° 12, p. 898-910.
- Anderson, D., A. Warkentin et R. Bauer. 2012. « Comparison of spherical and truncated cone geometries for single abrasive-grain cutting ». *Journal of Materials Processing Technology*, vol. 212, n° 9, p. 1946-1953.
- Doman, D. A., R. Bauer et A. Warkentin. 2009a. « Experimentally validated finite element model of the rubbing and ploughing phases in scratch tests ». *Proceedings of the Institution of Mechanical Engineers, Part B (Journal of Engineering Manufacture)*, vol. 223, n° Copyright 2010, The Institution of Engineering and Technology, p. 1519-27.
- Fang, N. 2005a. « A New Quantitative Sensitivity Analysis of the Flow Stress of 18 Engineering Materials in Machining ». *Journal of Engineering Materials and Technology*, vol. 127, n° 2, p. 192-196.
- Grzesik, Wit. 2008. « Modelling and Simulation of Machining Processes and Operations ». In *Advanced Machining Processes of Metallic Materials*. p. 49-67. Amsterdam: Elsevier.
- Guo, Y. B., et David W. Yen. 2004. « A FEM study on mechanisms of discontinuous chip formation in hard machining ». *Journal of Materials Processing Technology*, vol. 155-156, p. 1350-1356.
- Hazel, Bruce, Jean Côté, Yvan Laroche et Patrick Mongenot. 2012b. « A portable, multiprocess, track-based robot for in situ work on hydropower equipment ». *Journal of Field Robotics*, vol. 29, n° 1, p. 69-101.
- Hoffmeister, Hans-Werner, et Arne Gerdes. 2011. « Finite element simulation of quick- Stop experiments for better understanding of chip formation in grinding ». In *17th CIRP*

Conference on Modelling of Machining Operations. (Sintra, Portugal) Vol. 223, p. 764-773. Coll. « Advanced Materials Research »: Trans Tech Publications.

Huang, J. M., et J. T. Black. 1996. « An Evaluation of Chip Separation Criteria for the FEM Simulation of Machining ». *Journal of Manufacturing Science and Engineering*, vol. 118, n° 4, p. 545-554.

Hwang, T. W., C. J. Evans et S. Malkin. 1999. « Size effect for specific energy in grinding of silicon nitride ». *Wear*, vol. 225-229, n° Part 2, p. 862-867.

J. Zouhar, M. Piska. 2008. « MODELLING THE ORTHOGONAL MACHINING PROCESS USING CUTTING TOOLS ». *MM Science Journal*.

Jaspers, S. P. F. C., et J. H. Dautzenberg. 2002. « Material behaviour in conditions similar to metal cutting: flow stress in the primary shear zone ». *Journal of Materials Processing Technology*, vol. 122, n° 2-3, p. 322-330.

Johnson, G. R., et W. H. Cook. 1985a. « Fracture characteristics of three metals subjected to various strains, strain rates, temperatures and pressures ». *Engineering Fracture Mechanics*, vol. 21, n° Copyright 1985, IEE, p. 31-48.

Kita, Yoshihiro, Mamoru Ido et Shigeki Hata. 1978. « The mechanism of metal removal by an abrasive tool ». *Wear*, vol. 47, n° 1, p. 185-193.

Lin, Z. C., et S. Y. Lin. 1992. « A Coupled Finite Element Model of Thermo-Elastic-Plastic Large Deformation for Orthogonal Cutting ». *Journal of Engineering Materials and Technology*, vol. 114, n° 2, p. 218-226.

Livermore (2006). LS-DYNA Theory Manual. L. S. T. Corporation.

Mamalis, A. G., M. Horváth, A. S. Branis et D. E. Manolacos. 2001. « Finite element simulation of chip formation in orthogonal metal cutting ». *Journal of Materials Processing Technology*, vol. 110, n° 1, p. 19-27.

Ng, Eu-Gene, et David K. Aspinwall. 2002. « Modelling of hard part machining ». *Journal of Materials Processing Technology*, vol. 127, n° 2, p. 222-229.

Ohbuchi, Y., et T. Obikawa. 2003. « Finite Element Modeling of Chip Formation in the Domain of Negative Rake Angle Cutting ». *Journal of Engineering Materials and Technology*, vol. 125, n° 3, p. 324-332.

Ozel, Tugrul, et Erol Zeren. 2005. « Finite Element Modeling of Stresses Induced by High

- Speed Machining With Round Edge Cutting Tools ». *ASME Conference Proceedings*, vol. 2005, n° 42231, p. 1279-1287.
- Pantalé, O., J. L. Bacaria, O. Dalverny, R. Rakotomalala et S. Caperaa. 2004. « 2D and 3D numerical models of metal cutting with damage effects ». *Computer Methods in Applied Mechanics and Engineering*, vol. 193, n° 39-41, p. 4383-4399.
- Patnaik Durgumahanti, U. S., Vijayender Singh et P. Venkateswara Rao. 2010. « A New Model for Grinding Force Prediction and Analysis ». *International Journal of Machine Tools and Manufacture*, vol. 50, n° 3, p. 231-240.
- Shaw, Milton C. 1993. « Some Observations Concerning the Mechanics of Cutting and Grinding ». *Applied Mechanics Reviews*, vol. 46, n° 3, p. 74-79.
- Shih, Albert J. 1995. « Finite element analysis of the rake angle effects in orthogonal metal cutting ». *International Journal of Mechanical Sciences*, vol. 38, n° 1, p. 1-17.
- T.T.Opoz, X.Chen. 2010. « FINITE ELEMENT SIMULATION OF CHIP FORMATION ». In *School of Computing and Engineering Researchers' Conference*. (University of Huddersfield, Quensgate, Huddersfield HD1 3DH, UK, Dec 2010).
- Tahvilian, A. M., Champliaud, H., Liu, Z., Hazel, B. . 2012. « Study of workpiece temperature distribution in the contact zone during robotic grinding process using finite element analysis ». In *CIRP ICME '12 - 8th CIRP Conference on INTELLIGENT COMPUTATION IN MANUFACTURING ENGINEERING*. (Gulf of Naples, Italy, 18 - 20 July 2012).
- Vaziri, M. R., M. Salimi et M. Mashayekhi. 2010. « A new calibration method for ductile fracture models as chip separation criteria in machining ». *Simulation Modelling Practice and Theory*, vol. 18, n° 9, p. 1286-1296.
- Xun, Chen, et T. T. Opoz. 2010. « Simulation Of Grinding Surface Creation - A Single Grit Approach ». *Advanced Materials Research*, vol. 126-128, n° Copyright 2010, The Institution of Engineering and Technology, p. 23-8.
- Yen, Yung-Chang, Anurag Jain et Taylan Altan. 2004. « A finite element analysis of orthogonal machining using different tool edge geometries ». *Journal of Materials Processing Technology*, vol. 146, n° 1, p. 72-81.

LIST OF REFERENCES

- Agarwal, Sanjay, et P. Venkateswara Rao. 2013. « Predictive modeling of force and power based on a new analytical undeformed chip thickness model in ceramic grinding ». *International Journal of Machine Tools and Manufacture*, vol. 65, n° 0, p. 68-78.
- Altan, Taylan, et Victor Vazquez. 1997. « Status of process simulation using 2D and 3D finite element method []What is practical today? What can we expect in the future?' ». *Journal of Materials Processing Technology*, vol. 71, n° 1, p. 49-63.
- Altintas, Y., et P. Lee. 1998. « Mechanics and Dynamics of Ball End Milling ». *Journal of Manufacturing Science and Engineering*, vol. 120, n° 4, p. 684-692.
- Anderson, D., A. Warkentin et R. Bauer. 2008a. « Comparison of numerically and analytically predicted contact temperatures in shallow and deep dry grinding with infrared measurements ». *International Journal of Machine Tools and Manufacture*, vol. 48, n° Compendex, p. 320-328.
- Anderson, D., A. Warkentin et R. Bauer. 2008c. « Experimental validation of numerical thermal models for dry grinding ». *Journal of Materials Processing Technology*, vol. 204, p. 269-78.
- Anderson, D., A. Warkentin et R. Bauer. 2011. « Experimental and numerical investigations of single abrasive-grain cutting ». *International Journal of Machine Tools and Manufacture*, vol. 51, n° 12, p. 898-910.
- Anderson, D., A. Warkentin et R. Bauer. 2012. « Comparison of spherical and truncated cone geometries for single abrasive-grain cutting ». *Journal of Materials Processing Technology*, vol. 212, n° 9, p. 1946-1953.
- Arrazola, P. J., D. Ugarte et X. Domínguez. 2008. « A new approach for the friction identification during machining through the use of finite element modeling ». *International Journal of Machine Tools and Manufacture*, vol. 48, n° 2, p. 173-183.
- Arrazola, Pedro J., et Tugrul Özel. 2010. « Investigations on the effects of friction modeling in finite element simulation of machining ». *International Journal of Mechanical Sciences*, vol. 52, n° 1, p. 31-42.
- Aslan, Deniz, et Erhan Budak. 2014. « Semi-analytical Force Model for Grinding Operations ». *Procedia CIRP*, vol. 14, n° 0, p. 7-12.
- Aurich, J. C., O. Braun, G. Warnecke et L. Cronjäger. 2003. « Development of a Superabrasive Grinding Wheel With Defined Grain Structure Using Kinematic Simulation ». *CIRP Annals - Manufacturing Technology*, vol. 52, n° 1, p. 275-280.

- Aurich, J. C., P. Herzenstiel, H. Sudermann et T. Magg. 2008. « High-performance dry grinding using a grinding wheel with a defined grain pattern ». *CIRP Annals - Manufacturing Technology*, vol. 57, n° 1, p. 357-362.
- Aurich, J. C., et B. Kirsch. 2012. « Kinematic simulation of high-performance grinding for analysis of chip parameters of single grains ». *CIRP Journal of Manufacturing Science and Technology*, vol. 5, n° 3, p. 164-174.
- Badger, J. A., et A. A. Torrance. 2000. « A comparison of two models to predict grinding forces from wheel surface topography ». *International Journal of Machine Tools and Manufacture*, vol. 40, n° 8, p. 1099-1120.
- Bansal, Narottam P., et Dongming Zhu. 2005. « Thermal conductivity of zirconia–alumina composites ». *Ceramics International*, vol. 31, n° 7, p. 911-916.
- Blunt, L., et S. Ebdon. 1996. « The application of three-dimensional surface measurement techniques to characterizing grinding wheel topography ». *International Journal of Machine Tools and Manufacture*, vol. 36, n° 11, p. 1207-1226.
- Blunt, L., et X. Jiang. 2003. *Advanced Techniques for Assessment Surface Topography: Development of a Basis for 3D Surface Texture Standards "Surfstand"*. Elsevier Science.
- Bonnet, C., F. Valiorgue, J. Rech et H. Hamdi. 2008. « Improvement of the numerical modeling in orthogonal dry cutting of an AISI 316L stainless steel by the introduction of a new friction model ». *CIRP Journal of Manufacturing Science and Technology*, vol. 1, n° 2, p. 114-118.
- Brinksmeier, E., J. C. Aurich, E. Govekar, C. Heinzl, H. W. Hoffmeister, F. Klocke, J. Peters, R. Rentsch, D. J. Stephenson, E. Uhlmann, K. Weinert et M. Wittmann. 2006. « Advances in modeling and simulation of grinding processes ». *CIRP Annals - Manufacturing Technology*, vol. 55, n° Compendex, p. 667-696.
- Brosse, A., P. Naisson, H. Hamdi et J. M. Bergheau. 2008. « Temperature measurement and heat flux characterization in grinding using thermography ». *Journal of Materials Processing Technology*, vol. 201, n° 1-3, p. 590-595.
- Butler, D. L., L. A. Blunt, B. K. See, J. A. Webster et K. J. Stout. 2002. « The characterisation of grinding wheels using 3D surface measurement techniques ». *Journal of Materials Processing Technology*, vol. 127, n° 2, p. 234-237.
- Carroll, John T., et John S. Strenkowski. 1988. « Finite element models of orthogonal cutting with application to single point diamond turning ». *International Journal of Mechanical Sciences*, vol. 30, n° 12, p. 899-920.

- Chang, Huang-Cheng, et J. J. Junz Wang. 2008. « A stochastic grinding force model considering random grit distribution ». *International Journal of Machine Tools and Manufacture*, vol. 48, n° 12–13, p. 1335-1344.
- Charles Gagnon, ing. 2010. « Inn-EAU-vation technologique à Hydro-Québec ». < <http://www.polymtl.ca/recherche/doc/CharlesGagnon.pdf> >. Consulté le 20-Jul-2010.
- Chen, Jianyi, et Xipeng Xu. 2010. « Temperature and energy partition in high-speed grinding of alumina with a brazed diamond wheel ». *Machining Science and Technology*, vol. 14, n° 4, p. 440-454.
- Comaniciu, D., et P. Meer. 2002. « Mean shift: a robust approach toward feature space analysis ». *Pattern Analysis and Machine Intelligence, IEEE Transactions on*, vol. 24, n° 5, p. 603-619.
- Cui, Changcai, Xipeng Xu, Hui Huang, Jie Hu, Ruifang Ye, Lijun Zhou et Chunqi Huang. 2013. « Extraction of the grains topography from grinding wheels ». *Measurement*, vol. 46, n° 1, p. 484-490.
- Dai, Gil Lee, Jin Kim Po et Kyung Choi Jin. 2000. « Temperature rise and surface roughness of carbon fiber epoxy composites during cut-off grinding ». *Journal of Composite Materials*, vol. 34, n° Compendex, p. 2061-2080.
- Darafon, Abdalslam. 2013. « Measuring and Modeling of Grinding Wheel Topography ». Halifax, Nova Scotia, Dalhousie University.
- Darafon, Abdalslam, Andrew Warkentin et Robert Bauer. 2013. « Characterization of grinding wheel topography using a white chromatic sensor ». *International Journal of Machine Tools and Manufacture*, vol. 70, n° 0, p. 22-31.
- Doman, D. A., R. Bauer et A. Warkentin. 2009a. « Experimentally validated finite element model of the rubbing and ploughing phases in scratch tests ». *Proceedings of the Institution of Mechanical Engineers, Part B (Journal of Engineering Manufacture)*, vol. 223, n° Copyright 2010, The Institution of Engineering and Technology, p. 1519-27.
- Doman, D. A., A. Warkentin et R. Bauer. 2006. « A survey of recent grinding wheel topography models ». *International Journal of Machine Tools and Manufacture*, vol. 46, n° 3–4, p. 343-352.
- Doman, D. A., A. Warkentin et R. Bauer. 2009b. « Finite element modeling approaches in grinding ». *International Journal of Machine Tools and Manufacture*, vol. 49, n° Compendex, p. 109-116.
- Fan, Xiaorui, et Michele H. Miller. 2006. « FORCE ANALYSIS FOR GRINDING WITH

- SEGMENTAL WHEELS ». *Machining Science and Technology*, vol. 10, n° 4, p. 435-455.
- Fang, N. 2005a. « A New Quantitative Sensitivity Analysis of the Flow Stress of 18 Engineering Materials in Machining ». *Journal of Engineering Materials and Technology*, vol. 127, n° 2, p. 192-196.
- Fengfeng, Xi, et D. Zhou. 2005. « Modeling surface roughness in the stone polishing process ». *International Journal of Machine Tools & Manufacture*, vol. 45, n° 4-5, p. 365-72.
- Gonzalez, Rafael, et Richard Woods. 2007. *Digital Image Processing (3rd Edition)*. Prentice Hall.
- Grzesik, Wit. 2008. « Modelling and Simulation of Machining Processes and Operations ». In *Advanced Machining Processes of Metallic Materials*. p. 49-67. Amsterdam: Elsevier.
- Guo, C., Y. Wu, V. Varghese et S. Malkin. 1999. « Temperatures and energy partition for grinding with vitrified CBN wheels ». *CIRP Annals - Manufacturing Technology*, vol. 48, n° Compendex, p. 247-250.
- Guo, Changsheng, et Stephen Malkin. 1999. « Energy partition and cooling during grinding ». *Technical Paper - Society of Manufacturing Engineers. MR*, n° MR99-228, p. 1-10.
- Guo, Y. B., et David W. Yen. 2004. « A FEM study on mechanisms of discontinuous chip formation in hard machining ». *Journal of Materials Processing Technology*, vol. 155-156, p. 1350-1356.
- Hadad, M. J., T. Tawakoli, M. H. Sadeghi et B. Sadeghi. 2012. « Temperature and energy partition in minimum quantity lubrication-MQL grinding process ». *International Journal of Machine Tools and Manufacture*, vol. 54-55, n° 0, p. 10-17.
- Hahn, R. S. 1962. « On the Nature of the Grinding Process ». In *Proceedings of the 3rd Machine Tool Design and Research Conference*. p. pp. 129-154.
- Hazel, Bruce, Jean Côté, Yvan Laroche et Patrick Mongenot. 2012a. « Field repair and construction of large hydropower equipment with a portable robot ». *Journal of Field Robotics*, vol. 29, n° 1, p. 102-122.
- Hazel, Bruce, Jean Côté, Yvan Laroche et Patrick Mongenot. 2012b. « A portable, multiprocess, track-based robot for in situ work on hydropower equipment ». *Journal of Field Robotics*, vol. 29, n° 1, p. 69-101.
- Hecker, RogelioL, StevenY Liang, XiaoJian Wu, Pin Xia et DavidGuoWei Jin. 2007. « Grinding force and power modeling based on chip thickness analysis ». *The*

- International Journal of Advanced Manufacturing Technology*, vol. 33, n° 5-6, p. 449-459.
- Hoffmeister, Hans-Werner, et Arne Gerdes. 2011. « Finite element simulation of quick- Stop experiments for better understanding of chip formation in grinding ». In *17th CIRP Conference on Modelling of Machining Operations*. (Sintra, Portugal) Vol. 223, p. 764-773. Coll. « Advanced Materials Research »: Trans Tech Publications.
- Hoffmeister, Hans-Werner, et Thomas Weber. 1999. « Simulation of grinding by means of the finite element analysis ». *Technical Paper - Society of Manufacturing Engineers. MR*, n° Compendex, p. 1-12.
- Huang, J. M., et J. T. Black. 1996. « An Evaluation of Chip Separation Criteria for the FEM Simulation of Machining ». *Journal of Manufacturing Science and Engineering*, vol. 118, n° 4, p. 545-554.
- Hwang, Jihong, Sridhar Kompella, Srinivasan Chandrasekar et Thomas N. Farris. 2003. « Measurement of Temperature Field in Surface Grinding Using Infra-Red (IR) Imaging System ». *Journal of Tribology*, vol. 125, n° 2, p. 377-383.
- Hwang, T. W., C. J. Evans et S. Malkin. 1999. « Size effect for specific energy in grinding of silicon nitride ». *Wear*, vol. 225-229, n° Part 2, p. 862-867.
- Hydro-Québec. 2004. « Innovation : SCOMPI ». < http://www.hydroquebec.com/technologie/fiches/pdf/prod_scompi_fr.pdf >. Consulté le 20-Jul-2010.
- Hydro-Québec. 2010. « The Advantages of Hydropower ». < <http://www.hydroquebec.com/learning/hydroelectricite/index.html> >. Consulté le 20-Jul-2010.
- Inasaki, I. 1996. « Grinding Process Simulation Based on the Wheel Topography Measurement ». *CIRP Annals - Manufacturing Technology*, vol. 45, n° 1, p. 347-350.
- Iwata, K., K. Osakada et Y. Terasaka. 1984. « Process Modeling of Orthogonal Cutting by the Rigid-Plastic Finite Element Method ». *Journal of Engineering Materials and Technology*, vol. 106, n° 2, p. 132-138.
- J. Zouhar, M. Piska. 2008. « MODELLING THE ORTHOGONAL MACHINING PROCESS USING CUTTING TOOLS ». *MM Science Journal*.
- Jaeger, J. C. 1942. « Moving sources of heat and temperature at sliding contacts ». *Royal Society of New South Wales -- Journal and Proceedings*, vol. 76, n° Part 3, p. 203-224.

- James R. Hendershot, J., et T.J.T.J.E. Miller. 1994. *Design of Brushless Permanent-Magnet Motors*. Magna Physics Pub.
- Jaspers, S. P. F. C., et J. H. Dautzenberg. 2002. « Material behaviour in conditions similar to metal cutting: flow stress in the primary shear zone ». *Journal of Materials Processing Technology*, vol. 122, n° 2-3, p. 322-330.
- Jin, T., et D. J. Stephenson. 2004. « Three dimensional finite element simulation of transient heat transfer in high efficiency deep grinding ». *CIRP Annals - Manufacturing Technology*, vol. 53, n° Compendex, p. 259-262.
- Johnson, E. C., L. Rui, A. J. Shih et H. Hanna. 2008. « Design of experiments based force modeling of the face grinding process ». In *Transactions of the North American Manufacturing Research Institution of SME*. Vol. 36, p. 241-248. In *Scopus*.
- Johnson, Gordon R., et William H. Cook. 1985b. « Fracture characteristics of three metals subjected to various strains, strain rates, temperatures and pressures ». *Engineering Fracture Mechanics*, vol. 21, n° 1, p. 31-48.
- Kapłonek, Wojciech, et Krzysztof Nadolny. 2013. « Assessment of the grinding wheel active surface condition using SEM and image analysis techniques ». *Journal of the Brazilian Society of Mechanical Sciences and Engineering*, vol. 35, n° 3, p. 207-215.
- Kita, Yoshihiro, Mamoru Ido et Shigeki Hata. 1978. « The mechanism of metal removal by an abrasive tool ». *Wear*, vol. 47, n° 1, p. 185-193.
- Kohli, S., C. Guo et S. Malkin. 1995. « Energy Partition to the Workpiece for Grinding with Aluminum Oxide and CBN Abrasive Wheels ». *Journal of Engineering for Industry*, vol. 117, n° 2, p. 160-168.
- Koshy, Philip, V. K. Jain et G. K. Lal. 1993. « A model for the topography of diamond grinding wheels ». *Wear*, vol. 169, n° 2, p. 237-242.
- Koshy, Philip, V. K. Jain et G. K. Lal. 1997. « Stochastic simulation approach to modelling diamond wheel topography ». *International Journal of Machine Tools and Manufacture*, vol. 37, n° 6, p. 751-761.
- Lachance, Stéphane, Andrew Warkentin et Robert Bauer. 2003. « Development of an automated system for measuring grinding wheel wear flats ». *Journal of Manufacturing Systems*, vol. 22, n° 2, p. 130-135.
- Lavine, A. S., S. Malkin et T. C. Jen. 1989. « Thermal Aspects of Grinding with CBN Wheels ». *CIRP Annals - Manufacturing Technology*, vol. 38, n° 1, p. 557-560.
- Lefebvre, A., F. Lanzetta, P. Lipinski et A. A. Torrance. 2012. « Measurement of grinding

temperatures using a foil/workpiece thermocouple ». *International Journal of Machine Tools and Manufacture*, vol. 58, n° 0, p. 1-10.

- Li, Jing, et J. C. M. Li. 2005. « Temperature distribution in workpiece during scratching and grinding ». *Materials Science and Engineering: A*, vol. 409, n° 1-2, p. 108-119.
- Li, Xuekun, Sebastian Wolf, Geng Zhi et Yiming Rong. 2013. « The modelling and experimental verification of the grinding wheel topographical properties based on the 'through-the-process' method ». *The International Journal of Advanced Manufacturing Technology*, p. 1-11.
- Lichun, Li, Fu Jizai et J. Peklenik. 1980. « A Study of Grinding Force Mathematical Model ». *CIRP Annals - Manufacturing Technology*, vol. 29, n° 1, p. 245-249.
- Lin, B., M. N. Morgan, X. W. Chen et Y. K. Wang. 2009. « Study on the convection heat transfer coefficient of coolant and the maximum temperature in the grinding process ». *International Journal of Advanced Manufacturing Technology*, vol. 42, n° Compendex, p. 1175-1186.
- Lin, Z. C., et S. Y. Lin. 1992. « A Coupled Finite Element Model of Thermo-Elastic-Plastic Large Deformation for Orthogonal Cutting ». *Journal of Engineering Materials and Technology*, vol. 114, n° 2, p. 218-226.
- Liu, Qiang, Xun Chen, Yan Wang et Nabil Gindy. 2008. « Empirical modelling of grinding force based on multivariate analysis ». *Journal of Materials Processing Technology*, vol. 203, n° 1-3, p. 420-430.
- Liu, Yueming, Andrew Warkentin, Robert Bauer et Yadong Gong. 2013. « Investigation of different grain shapes and dressing to predict surface roughness in grinding using kinematic simulations ». *Precision Engineering*, vol. 37, n° 3, p. 758-764.
- Veillez sélectionner un type de document autre que « Generic » afin de faire afficher la référence bibliographique.
- Lonardo, P. M., H. Trumpold et L. De Chiffre. 1996. « Progress in 3D Surface Microtopography Characterization ». *CIRP Annals - Manufacturing Technology*, vol. 45, n° 2, p. 589-598.
- Mackerle, J. 2003. « Finite element analysis and simulation of machining: an addendum: A bibliography (1996-2002) ». *International Journal of Machine Tools and Manufacture*, vol. 43, n° 1, p. 103-114.
- Mackerle, Jaroslav. 1998. « Finite-element analysis and simulation of machining: a bibliography (1976-1996) ». *Journal of Materials Processing Technology*, vol. 86, n° 1-3, p. 17-44.

- Mahdi, M., et Zhang Liangchi. 1995. « The finite element thermal analysis of grinding processes by ADINA ». In *Nonlinear Finite Element Analysis and ADINA. 10th ADINA Conference, 21-23 June 1995*. (UK), 2-3 Vol. 56, p. 313-20. Coll. « Comput. Struct. (UK) ».
- Malkin, S., et R. B. Anderson. 1973. « Thermal aspects of grinding - 1. Energy partition ». *American Society of Mechanical Engineers (Paper)*, n° Compendex.
- Malkin, S., et N. H. Cook. 1971. « The Wear of Grinding Wheels: Part 1—Attritious Wear ». *Journal of Manufacturing Science and Engineering*, vol. 93, n° 4, p. 1120-1128.
- Malkin, S., et C. Guo. 2007. « Thermal Analysis of Grinding ». *CIRP Annals - Manufacturing Technology*, vol. 56, n° 2, p. 760-782.
- Malkin S., Guo C. 2008. *Grinding Technology: Theory and Applications of Machining with Abrasives*, 2nd. Industrial Press, New York.
- Mamalis, A. G., M. Horváth, A. S. Branis et D. E. Manolakos. 2001. « Finite element simulation of chip formation in orthogonal metal cutting ». *Journal of Materials Processing Technology*, vol. 110, n° 1, p. 19-27.
- Mamalis, A. G., J. Kundrak, D. E. Manolakos, K. Gyani et A. Markopoulos. 2003a. « Thermal modelling of surface grinding using implicit finite element techniques ». *International Journal of Advanced Manufacturing Technology*, vol. 21, n° Copyright 2004, IEE, p. 929-34.
- Mamalis, A. G., J. Kundrak, D. E. Manolakos, K. Gyani, A. Markopoulos et M. Horvath. 2003b. « Effect of the workpiece material on the heat affected zones during grinding: A numerical simulation ». *International Journal of Advanced Manufacturing Technology*, vol. 22, n° Compendex, p. 761-767.
- Mao, C., Z. X. Zhou, Y. H. Ren et B. Zhang. 2010. « Analysis and FEM simulation of temperature field in wet surface grinding ». *Materials and Manufacturing Processes*, vol. 25, n° 6, p. 399-406.
- Matsuno, Y., H. Yamada, M. Harada et A. Kobayashi. 1975. « The microtopography of the grinding wheel surface with SEM ». *CIRP Annals - Manufacturing Technology*, vol. 43, n° 1, p. 237-242.
- Mishra, Vijay Kumar, et Konstantinos Salonitis. 2013. « Empirical Estimation of Grinding Specific Forces and Energy Based on a Modified Werner Grinding Model ». *Procedia CIRP*, vol. 8, n° 0, p. 287-292.
- Mohamed, A. L. Mokhtar O., Andrew Warkentin et Robert Bauer. 2011. « Use of surface roughness measurements to improve the estimation of the heat partition in grinding ».

Journal of Materials Processing Technology, vol. 211, n° 4, p. 566-572.

- Mohamed, A. L. Mokhtar O., Andrew Warkentin et Robert Bauer. 2012a. « Variable heat flux in numerical simulation of grinding temperatures ». *International Journal of Advanced Manufacturing Technology*, vol. 63, n° 5-8, p. 549-554.
- Mohamed, A. L. MokhtarO, Andrew Warkentin et Robert Bauer. 2012b. « Variable heat flux in numerical simulation of grinding temperatures ». *The International Journal of Advanced Manufacturing Technology*, vol. 63, n° 5-8, p. 549-554.
- Ng, Eu-Gené, et David K. Aspinwall. 2002. « Modelling of hard part machining ». *Journal of Materials Processing Technology*, vol. 127, n° 2, p. 222-229.
- Nguyen, Anh Tuan, et David Lee Butler. 2008. « Correlation of grinding wheel topography and grinding performance: A study from a viewpoint of three-dimensional surface characterisation ». *Journal of Materials Processing Technology*, vol. 208, n° 1-3, p. 14-23.
- Nguyen, T. A., et D. L. Butler. 2005. « Simulation of surface grinding process, part 2: interaction of the abrasive grain with the workpiece ». *International Journal of Machine Tools and Manufacture*, vol. 45, n° 11, p. 1329-1336.
- Ohbuchi, Y., et T. Obikawa. 2003. « Finite Element Modeling of Chip Formation in the Domain of Negative Rake Angle Cutting ». *Journal of Engineering Materials and Technology*, vol. 125, n° 3, p. 324-332.
- Oxley, P. L. 1989. *The mechanics of machining an analytical approach to assessing machinability*. Chichester: Ellis Horwood [u.a.].
- Ozel, T. 2006. « The influence of friction models on finite element simulations of machining ». *International Journal of Machine Tools & Manufacture*, vol. 46, n° Copyright 2006, The Institution of Engineering and Technology, p. 518-30.
- Ozel, Tugrul, et Taylan Altan. 2000. « Determination of workpiece flow stress and friction at the chip-tool contact for high-speed cutting ». *International Journal of Machine Tools and Manufacture*, vol. 40, n° Compendex, p. 133-152.
- Ozel, Tugrul, et Erol Zeren. 2005. « Finite Element Modeling of Stresses Induced by High Speed Machining With Round Edge Cutting Tools ». *ASME Conference Proceedings*, vol. 2005, n° 42231, p. 1279-1287.
- Pantalé, O., J. L. Bacaria, O. Dalverny, R. Rakotomalala et S. Caperaa. 2004. « 2D and 3D numerical models of metal cutting with damage effects ». *Computer Methods in Applied Mechanics and Engineering*, vol. 193, n° 39-41, p. 4383-4399.

- Parente, MarcoPauloLages, RenatoM Natal Jorge, A. Aguiar Vieira et A. Monteiro Baptista. 2012. « Experimental and numerical study of the temperature field during creep feed grinding ». *The International Journal of Advanced Manufacturing Technology*, vol. 61, n° 1-4, p. 127-134.
- Park, Hyung Wook, et Steven Y. Liang. 2008. « Force modeling of micro-grinding incorporating crystallographic effects ». *International Journal of Machine Tools and Manufacture*, vol. 48, n° 15, p. 1658-1667.
- Patnaik Durgumahanti, U. S., Vijayender Singh et P. Venkateswara Rao. 2010. « A New Model for Grinding Force Prediction and Analysis ». *International Journal of Machine Tools and Manufacture*, vol. 50, n° 3, p. 231-240.
- Rafieian, Farzad, François Girardin, Zhaoheng Liu, Marc Thomas et Bruce Hazel. 2013. « Angular analysis of the cyclic impacting oscillations in a robotic grinding process ». *Mechanical Systems and Signal Processing*, vol. (article in press), n° Special issue on Instantaneous Angular Speed (IAS) processing and angular applications
- Rafieian, Farzad, François Girardin, Zhaoheng Liu, Marc Thomas et Bruce Hazel. 2014a. « Angular analysis of the cyclic impacting oscillations in a robotic grinding process ». *Mechanical Systems and Signal Processing*, vol. 44, n° 1-2, p. 160-176.
- Rafieian, Farzad, Bruce Hazel et Zhaoheng Liu. 2014b. « Vibro-impact dynamics of material removal in a robotic grinding process ». *The International Journal of Advanced Manufacturing Technology*, vol. 73, n° 5-8, p. 949-972.
- Robert D. Cook, David S. Malkus, Michael E. Plesha, Robert J. Witt. 2007. *Concepts and Applications of Finite Element Analysis*. John Wiley & Sons
- Roberto Rodríguez, Morales, Domínguez Didier, Torres Esley et H. Sossa Juan. 2012. « Image Segmentation Through an Iterative Algorithm of the Mean Shift ». In.
- Rowe, W. B., J. A. Pettit, A. Boyle et J. L. Moruzzi. 1988. « Avoidance of Thermal Damage in Grinding and Prediction of the Damage Threshold ». *CIRP Annals - Manufacturing Technology*, vol. 37, n° 1, p. 327-330.
- Sevier, M., H. T. Y. Yang, S. Lee et S. Chandrasekar. 2007. « Severe Plastic Deformation by Machining Characterized by Finite Element Simulation ». *Metallurgical and Materials Transactions B*, vol. 38, n° 6, p. 927-938.
- Shaw, Milton C. 1993. « Some Observations Concerning the Mechanics of Cutting and Grinding ». *Applied Mechanics Reviews*, vol. 46, n° 3, p. 74-79.
- Shi, Guoqin, Xiaomin Deng et Chandrakanth Shet. 2002. « A finite element study of the effect of friction in orthogonal metal cutting ». *Finite Elements in Analysis and*

- Design*, vol. 38, n° 9, p. 863-883.
- Shih, Albert J. 1995. « Finite element analysis of the rake angle effects in orthogonal metal cutting ». *International Journal of Mechanical Sciences*, vol. 38, n° 1, p. 1-17.
- Snoeys, R., J. Peters et A. Decneut. 1974. « SIGNIFICANCE OF CHIP THICKNESS IN GRINDING ». *Ann CIRP*, vol. 23, n° 2, p. 227-237.
- Stephen Malkin, Changsheng Guo. 2008. *Grinding Technology, Theory and Applications of Machining with Abrasives*, Second. Industrial Press, New York.
- T.T.Opoz, X.Chen. 2010. « FINITE ELEMENT SIMULATION OF CHIP FORMATION ». In *School of Computing and Engineering Researchers' Conference*. (University of Huddersfield, Quensgate, Huddersfield HD1 3DH, UK, Dec 2010).
- Tahvilian, A. M., Champliaud, H., Liu, Z., Hazel, B. . 2012. « Study of workpiece temperature distribution in the contact zone during robotic grinding process using finite element analysis ». In *CIRP ICME '12 - 8th CIRP Conference on INTELLIGENT COMPUTATION IN MANUFACTURING ENGINEERING*. (Gulf of Naples, Italy, 18 - 20 July 2012).
- Tahvilian, Amir Masoud, Zhaoheng Liu, Henri Champliaud et Bruce Hazel. 2013. « Experimental and finite element analysis of temperature and energy partition to the workpiece while grinding with a flexible robot ». *Journal of Materials Processing Technology*, vol. 213, n° 12, p. 2292-2303.
- Tang, Jinyuan, Jin Du et Yongping Chen. 2009. « Modeling and experimental study of grinding forces in surface grinding ». *Journal of Materials Processing Technology*, vol. 209, n° 6, p. 2847-2854.
- Tönshoff, H. K., J. Peters, I. Inasaki et T. Paul. 1992. « Modelling and Simulation of Grinding Processes ». *CIRP Annals - Manufacturing Technology*, vol. 41, n° 2, p. 677-688.
- Top-alternative-energy-sources. 2010. « Hydro Turbine ». < <http://www.top-alternative-energy-sources.com/water-turbine.html> >. Consulté le 20-Jul-2010.
- Transchel, R., C. Leinenbach et K. Wegener. 2014. « Cutting and ploughing forces for small clearance angles of hexa-octahedron shaped diamond grains ». *CIRP Annals - Manufacturing Technology*, vol. 63, n° 1, p. 325-328.
- Vaziri, M. R., M. Salimi et M. Mashayekhi. 2010. « A new calibration method for ductile fracture models as chip separation criteria in machining ». *Simulation Modelling Practice and Theory*, vol. 18, n° 9, p. 1286-1296.

- Verkerk, J. 1977. *Final Report Concerning CIRP Cooperative Work on the Characterization of Grinding Wheel Topography*. Lab. for Prod. Technol.
- Wang, Dexiang, Peiqi Ge, Wenbo Bi et Jingliang Jiang. 2014. « Grain trajectory and grain workpiece contact analyses for modeling of grinding force and energy partition ». *International Journal of Advanced Manufacturing Technology*, vol. 70, n° 9-12, p. 2111-2123.
- Wang, L., Y. Qin, Z. C. Liu, P. Ge et W. Gao. 2003. « Computer simulation of a workpiece temperature field during the grinding process ». *Proceedings of the Institution of Mechanical Engineers, Part B (Journal of Engineering Manufacture)*, vol. 217, n° Copyright 2004, IEE, p. 953-9.
- Weingaertner, W. L., et A. Boaron. 2012. « A method to determine the grinding wheel's topography based on acoustic emission ». *International Journal of Abrasive Technology*, vol. 5, n° 1, p. 17-32.
- Werner, Günter. 1973. « Konzept und technologische Grundlagen zur adaptiven Prozessoptimierung des Aussenrundscheifens ». In /z-wcorg/. <http://worldcat.org>.
- Winter, Marius, Wen Li, Sami Kara et Christoph Herrmann. 2014. « Determining optimal process parameters to increase the eco-efficiency of grinding processes ». *Journal of Cleaner Production*, vol. 66, n° 0, p. 644-654.
- Xie, J., F. Wei, J. H. Zheng, J. Tamaki et A. Kubo. 2011. « 3D laser investigation on micron-scale grain protrusion topography of truncated diamond grinding wheel for precision grinding performance ». *International Journal of Machine Tools and Manufacture*, vol. 51, n° 5, p. 411-419.
- Xie, J., J. Xu, Y. Tang et J. Tamaki. 2008. « 3D graphical evaluation of micron-scale protrusion topography of diamond grinding wheel ». *International Journal of Machine Tools and Manufacture*, vol. 48, n° 11, p. 1254-1260.
- Xun, Chen, et T. T. Opoz. 2010. « Simulation Of Grinding Surface Creation - A Single Grit Approach ». *Advanced Materials Research*, vol. 126-128, n° Copyright 2010, The Institution of Engineering and Technology, p. 23-8.
- Yan, Lan, Y. M. Rong, Feng Jiang et ZhiXiong Zhou. 2011. « Three-dimension surface characterization of grinding wheel using white light interferometer ». *The International Journal of Advanced Manufacturing Technology*, vol. 55, n° 1-4, p. 133-141.
- Yao, Changfeng, Ting Wang, Wei Xiao, Xinchun Huang et Junxue Ren. 2014. « Experimental study on grinding force and grinding temperature of Aermet 100 steel in surface grinding ». *Journal of Materials Processing Technology*, vol. 214, n° 11, p.

2191-2199.

- Yen, Yung-Chang, Anurag Jain et Taylan Altan. 2004. « A finite element analysis of orthogonal machining using different tool edge geometries ». *Journal of Materials Processing Technology*, vol. 146, n° 1, p. 72-81.
- Zeren, Tuğrul Özel and Erol. 2004. « Finite Element Method Simulation of Machining of AISI 1045 Steel With A Round Edge Cutting Tool ».
- Zerilli, Frank J., et Ronald W. Armstrong. 1987. « Dislocation-mechanics-based constitutive relations for material dynamics calculations ». *Journal of Applied Physics*, vol. 61, n° 5, p. 1816-1825.

